Adsorption on Metal-Supported Silicate Films: Surface and Sub-Surface Chemistry

DISSERTATION

zur Erlangung des akademischen Grades

doctor rerum naturalium
Dr. rer. nat.
im Fach Chemie

eingereicht an der
Mathematisch-Naturwissenschaftlichen Fakultät
Humboldt-Universität zu Berlin

von
Emre Emmez M.S.

Präsident der Humboldt-Universität zu Berlin:
Prof. Dr. Jan-Hendrik Olbertz

Dekan der Mathematisch-Naturwissenschaftlichen Fakultät:
Prof. Dr. Elmar Kulke

Gutachter/in:

1. Prof. Dr. Hans-Joachim Freund
2. Prof. Dr. Klaus Rademann
3. Prof. Dr. Swetlana Schauermann

Datum der Einreichung: 27.08.2015

Datum der Promotion: 01.12.2015

to my family and Didem

Acknowledgements

First and foremost, I would like to express my sincere gratitude to my supervisor Prof. Hans-Joachim Freund for his continuous support during my PhD research, for his patience, motivation, immense knowledge and providing me such an excellent atmosphere for doing research. I am also grateful to Prof. Klaus Rademann for supervising and reviewing my thesis at Humboldt University.

I would like to thank Dr. Shamil Shaikhutdinov, my advisor, who directed this work on a daily basis, for his guidance, understanding, and most importantly his friendship during my PhD study. His mentorship was very valuable for me in terms of growing not only as an experimentalist but also as an independent thinker by being allowed to work with freedom.

Great technical assistance was provided for my UHV system by Uwe Härtel and Matthias Naschitzki, I am very much grateful to them. I would also like to give my special thanks to Klaus-Peter Vogelgesang for his efficient assistance in preparing parts for my equipment and also his very kind personality which created a friendly atmosphere in the lab. I enjoyed so much from our discussions and this will always be remembered.

My sincere thanks also go to Manuela Misch and Gabi Mehnert, our department secretaries, for helping me to set a new life in Berlin and also their continuous support dealing with official works. I must also acknowledge Bettina Menzel, IMPRS program secretary, for her cordial advices in all discussion meetings and block courses that we had in this research school.

I am very grateful for all the friendship of all the members of my department, especially Anibal Boscoboinik, Osman Karslioglu, Xin Yu, Yulia Martynova, Bo Hong Liu, Christin Büchner, Stefanie Stuckenholz, Adrian Lewandowski, Earl Davis, Karl-Heinz Dostert, Yi Cui, Sebastian Beeg and Qiushi Pan. The last two years of my PhD study were particularly unique for me such that I was lucky to be surrounded by many wonderful friends, with whom I always felt relaxed, encouraged and being understood. Therefore, very special thanks go to Leandro Pascua, Christian Stiehler, and Francesca

Mirabella for always being there to listen. I greatly cherish all the wonderful memories that we had during this short but meaningful period of time.

Most importantly, none of this would have been possible without the love and patience of my family. I would like to express my heart-felt gratitude to my mother Temaşa, my father Erdener, my sister Merve and my brother Emirhan. It was under their watchful eyes that I gained so much ability to tackle the challenges and they have always been a constant source of love, support and strength all these years.

Finally, I would like to thank Didem. Her tireless love was undeniably the most important bedrock upon which the past five years of my life have been built. I appreciate her tolerance to my unstable moods and admire her optimism, energy and solid devotion which have always been an endless inspiration to me.

Abstract

The fundamental aspects of the chemical reactions at surfaces can be elucidated by using well-defined model systems under the controlled conditions provided by vacuum-based techniques. Silicon dioxide (SiO_2) as one of the crucial materials in modern technological applications, including microelectronics, photonics, and catalysis, has been subjected to numerous studies in order to rationalize relationships between the atomic structure and functional properties of silica-based materials.

This work marks the attempt to understand interaction of ambient gases with a well-ordered, ultrathin silicate film grown on a Ru(0001) substrate. As the performance of silica in catalysis is primarily determined by surface hydroxo species, we first addressed water adsorption. Using infrared reflection absorption spectroscopy (IRAS) and temperature programmed desorption (TPD), hydroxo species, primarily in the form of isolated silanols (Si-OH), were identified on pristine silicate films. Silanols covered less than a few percent of the surface Si atoms and are thermally stable up to 900 K. Isotopic experiments demonstrated that *surface* hydroxyls form primarily from the water molecules. Silanols do not undergo scrambling with the lattice oxygen atoms upon dehydroxylation. Steps on a silicate sheet and/or "holes" in these ultrathin films are proposed as active sites for hydroxylation. The acidic properties of silanols were studied with adsorption of CO and NH_3 as weak and strong bases, respectively.

Adsorption of gases such as CO, H_2 and O_2 at elevated pressures revealed a more complex behavior. It involves gas transport through the pores, associated with structural defects in the silicate film, subsequent adsorption, and diffusion across the Ru(0001) surface underneath. During this intercalation, the silicate film stays intact even under high pressure (~10 mbar) and high temperature conditions (~900 K). In particular, O_2 molecules readily penetrate the film and dissociate on the underlying Ru surface underneath. The silicate layer does however strongly passivate the Ru surface towards RuO_2(110) formation that readily occurs on bare Ru(0001) under the same conditions. The results indicate considerable spatial effects for oxidation reactions on metal surfaces in the confined space at the interface. Such a hybrid system, which combines a robust silica "membrane" and a chemically active metal underneath, could become an interesting material for technological applications, in particular in catalysis, sensors and anti-corrosion applications.

Zusammenfassung

Die grundlegenden Aspekte chemischer Reaktionen auf Oberflächen können anhand von geeigneten Modelsystemen unter Vakuumbedingungen untersucht werden. Siliciumdioxid(SiO_2) als wichtiges Material für hochmoderne Technologieanwendungen in der Mikroelektronik, Photonik und Katalyse, war Gegenstand zahlreicher Studien, um die Beziehungen zwischen der atomaren Struktur und funktionalen Eigenschaften von Silizium-basierten Materialien zu erklären.

Diese Arbeit untersucht die Wechselwirkung von Gasen mit epitaktisch gewachsenen Silikat-Dünnschichten auf einem Ru(0001) Einkristall. Da die Leistungsfähigkeit von Siliziumdioxid in katalytischen Prozessen hauptsächlich von Hydroxygruppen an der Oberfläche abhängt, haben wir uns zunächst mit der Oberflächenadsorption von Wasser beschäftigt. Unter Verwendung von Infrarot-Reflexions-Absorptions-Spektroskopie (IRAS) und temperaturprogrammierter Desorptionspektroskopie (TPD) konnten die Hydroxy-Spezies auf reinen Silikatfilmen als isolierte Silanole (Si-OH) identifiziert werden. Silanole bedecken lediglich wenige Prozent der Siliziumatome an der Oberfläche und sind thermisch stabil bis zu 900 K. Isotopenexperimente haben gezeigt, dass sich thermisch stabile Oberflächenhydroxylate hauptsächlich aus der Adsorption von Wassermolekülen bilden. Ein Austausch der Silanole mit Sauerstoffatomen im Kristallgitter während des Dehydroxylierungsprozesses wurde nicht beobachtet. Stufenkanten und/ oder Löcher in den ultradünnen Oxidfilmen werden als aktive Zentren für die Hydroxylierung verantwortlich gemacht. Die Säureeigenschaften der Silanole wurden anhand von CO- und NH_3-Adsorption als schwache bzw. starke Basen untersucht.

Durch die Adsorption von Gasen wie CO, H_2 und O_2 bei erhöhtem Druck, lässt sich auf komplexere Prozesse schließen. Dies beinhaltet Gastransport durch Poren im Film, was mit strukturellen Defekten in dem Silikatfilm verbunden ist, sowie nachfolgende Adsorption und Diffusion auf dem unterliegenden Ru(0001)-Substrat. Während der Einlagerung der Moleküle in die Silikatschicht bleibt der Oxidfilm auch unter hohem Druck (~ 10 mbar) sowie hoher Temperatur (~ 900 K) intakt. Insbesondere Sauerstoffmoleküle können den dünnen Film problemlos durchdringen und dissoziieren auf der Ru(0001)-Oberfläche. Die Silikatschicht passiviert jedoch die Ru Oberfläche in Richtung RuO_2(110), welches sich unter den gleichen Bedingungen auf einer Ru(0001)-

Oberfläche leicht bildet. Die Ergebnisse zeigen erhebliche räumliche Effekte für Oxidationsreaktionen auf Metalloberflächen in dem begrenzten Raum an der Grenzfläche. Solch ein Hybridsystem, welches eine robuste Siliciumdioxidmembran mit einem sich darunter befindlichen, chemisch aktiven Metall kombiniert, könnte ein interessantes Materialsystem für technische Anwendungen darstellen, insbesondere zur Herstellung von Katalysatoren und Sensoren sowie für Korrosionsanwendungen.

Contents

1. Introduction

Silica and silicates, which form the largest part of the earth's crust and mantle, share the same importance as raw materials and as mass produced items. Therefore, they have been the subject of scientific research by geoscientists as well as by applied scientists in cement, ceramic, glass, and other industries.

The importance of silicon for life on earth mainly results from the fact that the fertility of soil relies in large part on the ability of clay minerals to absorb and release water and several cations are crucial for plant nutrition [1]. This process is fundamental to the life of superior plants and to the life of those animals which feed upon the plants.

Silica is also commonly used in semiconductor circuits to isolate different conducting regions. Due to its mechanical resistance, high dielectric strength, and selectivity for chemical modification, amorphous silica has also become a key material in microelectronics and chromatography. Due to its unique properties, silica is widely utilized for a broad range of applications: chips, optical fibers, and telescope glasses. Moreover, molecular biologists utilize silica in resins and optical beads to investigate the biomacromolecules[2].

1.1 Diversity of Silicon Compounds

Silicon, after carbon, forms the largest number of compounds which are dominated by Si-O bonds. Since silicon come after carbon in the fourth main group of the periodic table, it could be expected that the factors that produce so large variety of carbon compounds would be the same for the large variety of silicon compounds. However, the result is different.

The substantial number of carbon compounds is due to the fact that the bond energies of the C-C, C-O, and C-H bonds (Table 1.1) are almost equal magnitude and they will be formed with about the same probability.

Bond	C	Si
X-X	346	222
X-O	358	452
X-H	413	318

Table 1.1: Several bonds of carbon and silicon bond energies in kj/ mol [1].

However, the bond energy of the Si-O bond is considerably higher than that of the Si-H bond and much more than that of the Si-Si bond. As a result of this, instead of the common -C-C-C- chains of carbon chemistry, the skeletons of silicon chemistry are formed by –Si-O-Si-O-Si- chains[1]. Furthermore, since only one of the three kinds of bonds, Si-Si, Si-O, and Si-H, is energetically favored in silicon chemistry, while these three bonds are almost equally favorable in carbon chemistry, the number of silicon compounds is smaller than the number of carbon compounds.

SiO_4 tetrahedron is the basic building block of all silicates. It is a structural unit with a silicon atom in the center of four surrounding oxygen atoms. The bond angles between two oxygen atoms are $109^o28$the Si-O bond distance is 1.60 Å, and the edge length of the SiO_4 tetrahedron is 2.62 Å [3].

The electronic structure of silicon is $1s^2 2s^2 2p^6 3s^2 3p^2$. In order to convert the ground state $3s^2 3p^2$ to four unpaired electrons $3s^1 3p^3$, relatively little energy is required. The spherical s orbital and the three extended p orbitals which are hybridized to four equivalent orbitals point towards the corners of a tetrahedron. In the case of oxygen coordination, this results in a stable structural element (SiO_4).

The bond between silicon and oxygen is most likely a mixed bond [4]. Pauling's [5] calculated Si-O value of 1.62 Å under the assumption that all three bond types (polar, isovalent, double bonding) are possible, and this agrees quite well with the experimental value of about 1.60 Å. Analogously, the bond angles agree with those of the model. An angle of 90^o would be expected for purely covalent σ bonding, and 180^o for pure π bonding. Experimental values for Si-O-Si in silicates are between 130^o and 140^o [3].

Another important consideration is the effective charge on each atom in SiO_2. For completely covalent bonding system, the net excess charge on each atom would be zero, resulting into four valence electrons on each silicon atom and six valence electrons on each oxygen atom. For completely ionic SiO_2, the net excess charge on each oxygen atom would be -2, and each silicon atom, +4. The actual situation lies somewhere in between. Many calculations [6-8] have been performed to determine the net charge transfer from Si to O in the various silica structures, and they all agree that the effective excess charge on O is about one electron per oxygen atom. Furthermore, with the light of these calculations, this excess charge (i.e., the ionicity) increases as the Si-O-Si bond angle increases.

Silica has a rich phase diagram as depicted in Figure 1.1. Phase transitions at atmospheric pressures include α quartz to β quartz at 573 ^{o}C, then to tridymite at 870 ^{o}C, and finally to β cristobalite at 1470 ^{o}C. Silica melting occurs at 1705 ^{o}C.

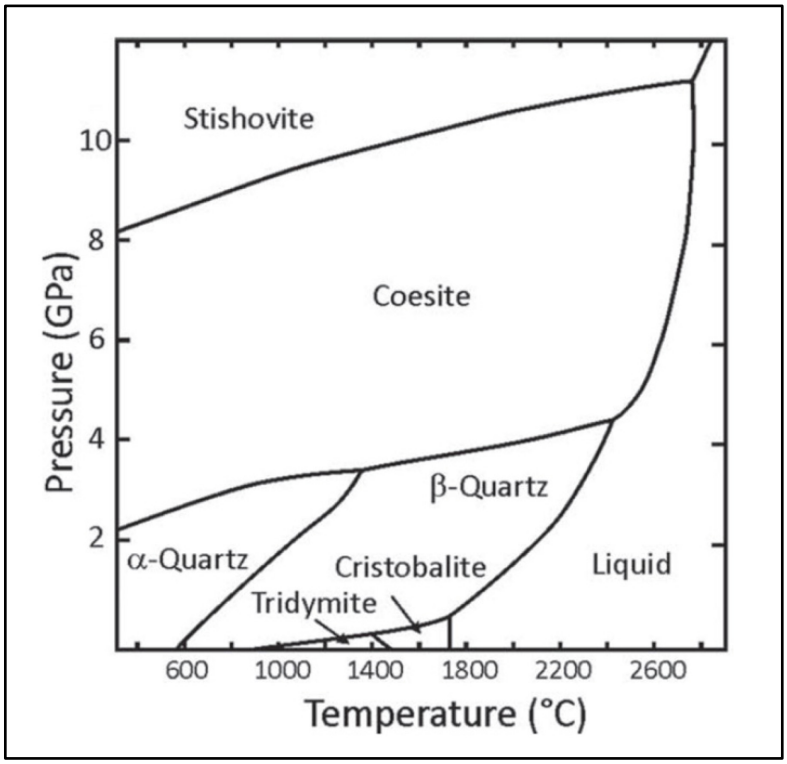

Figure 1.1: Phase diagrams of silica polymorphs [9].

1.2 Crystalline and Vitreous Silica

Glass is an essential component in fields such as optical communications, photovoltaic cells, home electronic equipment, vehicles, building materials and catalysis [10]. Due to the fast growing demand for glasses with novel properties, especially in the fields of photonics and energy science, glasses have developed over the past several decades from primarily silicates to borates, phosphates, germinates, and tellurites, as well as non-oxide glasses such as fluoride glass, halogenide glass, chalcogenide glass, and even metallic glass [10].

The structure of glass is the crucial question in glass science. The vitreous supercooled liquid state between the molten liquid state and the crystalline state represents one clear difference between glass and other condensed matter. This distinctive property of glass is different from the solid, liquid, and gaseous states observed for other elements [11].

Figure 1.2 shows the dependence of the intensity of X-ray diffraction on grazing angle *(sin □/λ).*

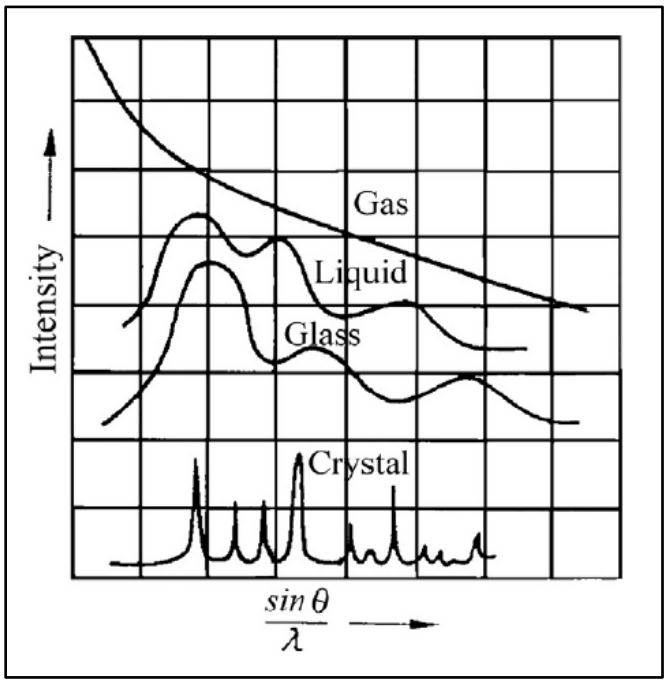

Figure 1.2: Intensity of scattered X-rays distribution in dependence on the grazing angle for substances in various states of aggregation [3].

Structural description of glasses has been a subject for decades. The network hypothesis proposed by Zachariasen [12] and supported by Warren's [13] X-ray diffraction

represented a step forward in the knowledge about the structure of glasses. The observations tell us that the same tetrahedral structures that are uniformly connected in crystalline silicates (Figure 1.3a) are connected irregularly in the case of SiO_2 glass (Figure 1.3b).

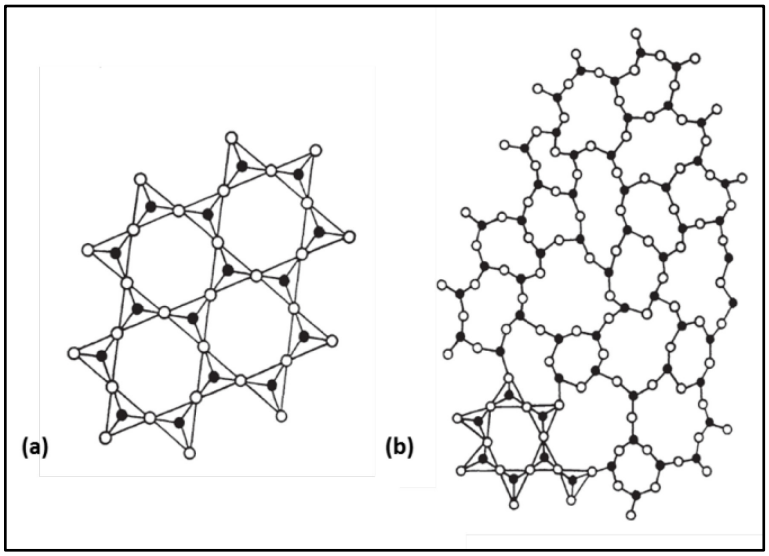

Figure 1.3: SiO_4 linkages in crystallized and amorphous SiO_2. (a) Regularly ordered SiO_4 building blocks in crystalline silica (b) Disordered linkages if SiO_4 building blocks in silica glass [3].

According to the Zachariasen-Waren network theory, the following rules are valid for the formation of low-order 3-dimensional networks[3],

(a) An oxide or compound tends to form glass if it easily forms polyhedral groups as smallest building units.

(b) Polyhedra should not share more than one corner.

(c) Anions (e.g., O^{2-}, S^{2-}, F^{-}) should not bind more than two central atoms of a polyhedron. Therefore, anions form bridges between two polyhedra in simple glasses.

(d) The number of corners of polyhedral must <6.

(e) At least three corners of a polyhedron must connect with neighbor polyhedra.

Zachariasen classified the cations in a glass as follows[3]:

(a) Network-formers, such as Si, B, P, Ge, As, Be (with F), etc., with a coordination number of generally 3 or 4.

(b) Network-modifiers, such as Na, K, Ca, Ba, etc., with coordination numbers generally ≥6.

(f) Intermediates may either reinforce the network (coordination number 4) of further loosen the network (coordination numbers 6-8).

A large number of properties of conventional glasses can be explained or predicted by the Zachariasen-Waren concept; however, the theory does not apply to all glass systems.

1.3 Silica in Catalysis

It is useful noting two factors that have some importance in relation to silica as a catalyst support. On the one hand side, silica with a Tamman temperature of 987 K [14], exhibits no phase transitions on heating to moderate temperatures and thus, the possibility of sintering is limited. For this reason, it is expected to be able to use silica as a support for reactions occurring up to about 973 K. However, on the opposing site, silica is not totally an inert solid and the surface chemistry is dominated by the reactivity of terminal silanol groups, Si-OH [15, 16].

Yet as the support of catalyst, silica has a large industrial application. This is due to its good mechanical and thermal stabilities, and ease of scalability. Among the most well-known application, it is utilized in the catalysts for the oxidation of SO_2 to SO_3, performed at 400-550 ^oC with air as an oxidizing agent. Industrial catalyst for this reaction is V_2O_5/SiO_2 (can also contain an alkali sulfate such as K_2SO_4 or Cs_2SO_4).

The catalyst is essentially composed by a porous silica carrier containing 5-10% V_2O_5 and 10-25% of alkali oxide [17], later on alkali oxide converts into the sulfate in the reaction. It is observed that, the active species are actually in the liquid phase embedded in the silica support.

Although alumina is the most commonly used support of metals for hydrogenation of hydrocarbons, silica is also used in several cases. For example, the hydrogenation of acetylene is normally performed with Pd/Al_2O_3 catalysts, but to perform the same

reaction to convert acetylene in the HCl recycle of the vinyl chloride process, Pd/SiO_2 is preferred. (Noblyst® E 39H from Evonik) [18]. A TEM image of a Pd/SiO_2 catalyst which is used for the direct synthesis of H_2O_2 from H_2 and O_2 in a H_2SO_4/Ethanol system is shown in Figure 1.4[19].

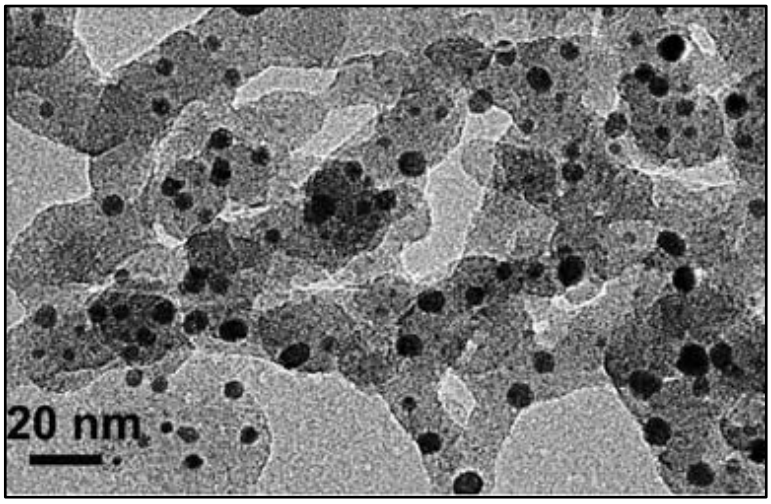

Figure 1.4: TEM image of a Pd/SiO_2 catalyst [19].

Silica also acts as a support for chromium oxides resulting in a catalytic system in which the active sites are formed by anchoring a chromium compound to the hydroxyl groups of the silica surface. Therefore, the description of the silica surface is crucial in order to understand its relevant effect on the catalyst activity. Such a description will be given in detail in the further chapters of this thesis. A suitable spaced OH groups are necessary for the anchoring process of Cr and the surface structure of silica plays an important role on the bonding and location of the anchored species. The Philips catalysts, which is obtained after reduction of Cr(VI) oxide sites on silica support by either carbon monoxide or ethylene, patented in 1958 by Hogan and Banks [20] are responsible for the polymerization of ethylene and the commercial production of more than one-third of all of the polyethylene sold worldwide [21, 22]. The polymerization properties critically depend on choice of silica with specific surface area, concentration of surface hydroxyls, as well as Cr loading.

The TiO_2-SiO_2 catalyst discovered by Shell, is a heterogeneous catalyst for liquid phase epoxidations [23]. The number of silanol groups on the silica surface defines the amount of TiO_2 which can be incorporated. The resulting material is an active and selective catalyst for the epoxidation of a broad range of olefins with alkyl hydroperoxides [24].

The high activity is attributed to the formation of site-isolated Ti^{+4} species on the silica surface.

1.4 Aluminosilicates and Zeolites

Substitution of silicon atoms in the silica framework, typically by aluminum atoms, changes the formal charge on the corresponding tetrahedra from neutral to 1^-. Charge balancing occurs by extra-framework metal cations or hydroxyl protons forming weak Lewis acids site or strong Brønsted acid sites, which are responsible for the catalytic activity of the zeolite materials [25-27].

The silanol groups (Si-OH), also called terminal OH groups, are the second crucial type of hydroxyl groups in zeolites. (Figure 1.5b) These species are located on the external surface of crystal particles or at framework defects [28]. Calcination, hydrothermal treatment, or treatment with strong acids lead to dealumination of the zeolite, and this is the most important reason for the formation of framework defects and silanol groups.

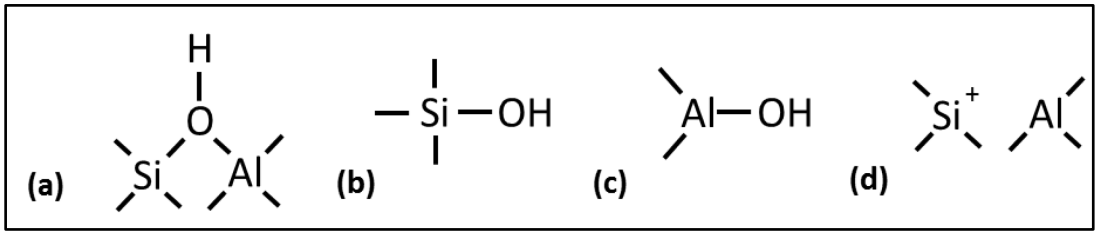

Figure 1.5: Schematic representation of the different types of hydroxyl groups and acid sites in zeolites [28].

Dealumination of the zeolite framework often results in the formation of Lewis acid sites at extra-framework aluminum species and framework defects. (Figure 1.5d) Superacidic Brønsted sites are formed when these Lewis acid sites placed in the vicinity of bridging OH groups [29, 30]. These frameworks Lewis acid sites can act as strong electron withdrawing centers for the neighboring bridging OH groups and generate Brønsted acid sites with a very high strength.

Zeolite materials with different surface acidic sites are being used as important catalysts in chemical technology. The framework of a zeolite contains channels and cages with

different dimensions which gives them unique selectivity towards different type of reactions (Figure 1.6).

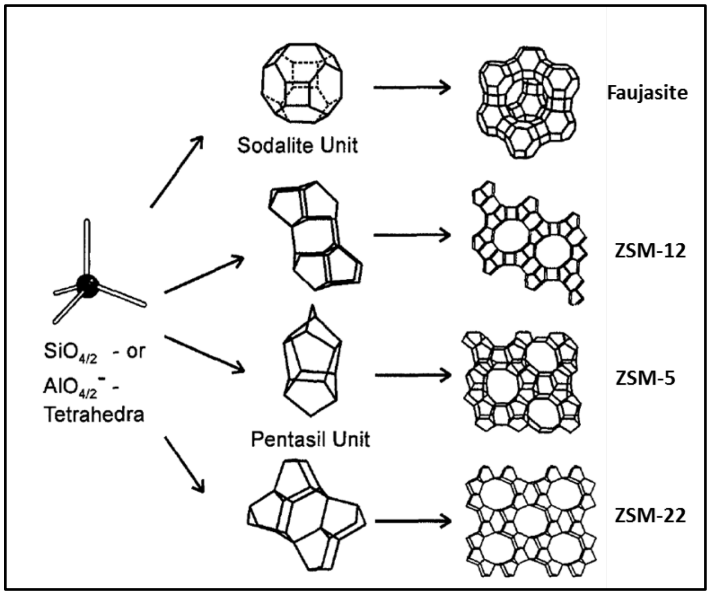

Figure 1.6: Four different type of zeolites and their structural building blocks [31].

In addition to the fluid catalytic cracking (FCC) [32, 33], zeolites are applied in basic petrochemistry, such as isomerization of light gasoline [34], hydrocracking of heavy petroleum distillates [35], catalytic dewaxing [35], alkylation of benzene with ethene or propene [36], disproportionation of toluene [37], isomerization of xylenes [37] and the methanol-to-gasoline process which is considered as a powerful technology to convert coal into high-octane gasoline [38].

In addition to aluminosilicate-type zeolites, the Brønsted acidity based on bridging OH groups can also be obtained by a large variety of crystalline materials that have exchangeable cations, such as silicoaluminophoshates (SAPOs) [39] , ferrosilicates [40, 41] and gallosilicates [42, 43]. Moreover, the Si-O-T bond angle can affect the partial charge and acid strength of the hydroxyl protons [44]. For instance, in zeolite ZSM-5, the Si-O-T bond angles vary from 137^{o} to 177^{o}, for mordenite from 143^{o} to 180^{o}, and for zeolite Y from 138^{o} to 147^{o}[45, 46].

1.5 Model Catalysts: A Surface Science Approach

More than 85% of all chemical products are produced by catalytic processes. Particularly heterogeneous catalysis is very significant in environmental chemistry [47], organic synthesis, depollution, oil refinery, energy storage and conversion [48] and many other fields. Real world catalysts are generally composed of several components in precise proportions which results in catalysts complexity due to their lack of characterization. It is important to be able to have a control over fundamental surface properties of catalytic materials such as particle size, morphology, chemical composition, dispersion in order to promote new catalysts with enhanced performance. A possible strategy has been already suggested by Irving Langmuir [49]. He was proposing the idea of using plane surfaces for catalytic reactions in order to simplify the structure complexity of finely divided catalysts. Langmuir's surface science approach has only become available after almost 30 years (in the late 1960s) with the development of UHV technology in which well-ordered extended surfaces of catalytic materials can be prepared and characterized by the diverse surface science techniques (XPS, AES, UPS, HREELS, LEED, STM etc.). With these systems the structural, electronic, or dynamic properties of many metal surfaces became accessible. However, the well-defined surface science model catalysts are much more simplistic in terms of their structures causing a so called "*materials gap"* between surface science and industrial catalysis [50]. Furthermore, technical catalysts are typically operated at elevated pressures (>760 Torr) which is considerably far from the UHV conditions in surface science studies. This is known as the "*pressure gap"* between applied catalysis and surface science[51]. This pressure difference presents a substantial obstacle for associating UHV characteristics with actual catalyst mechanism. The combination of UHV spectroscopic chamber with an elevated pressure reactor and sample transfer system is a common approach to circumvent the pressure gap [52]. With this procedure, one can treat the material under realistic conditions while collecting valuable information in the UHV chamber, or even in high pressure cell by SFG or PM-IRAS techniques. Several combined UHV compatible high pressure reaction cell system designs have been published in the literature [53].

Great efforts have been made to apply surface science methods to oxide surfaces since most heterogeneous catalysts are based on metal oxides or oxide supported metal

particles [54]. In these systems, the metal/oxide interface plays an essential role in many technologically important applications, including novel structural materials based on metal/ceramic composites, metal/oxide seals in device and medical implant construction, metal/oxide contacts in microelectronic and photovoltaic devices, coatings for corrosion passivation, gas-sensors, and oxide-supported transition metal catalysts [55]. Controlling the defect properties of the oxide surface is very crucial, since they have a major influence on the reactivity and the metal deposits growth. There are three common ways for the preparation of oxide surfaces in UHV conditions. One is to prepare a planar oxide surface with low defect density is by cleaving of oxide single crystals. For instance, MgO(100) is one of the most used cleaved surface which gives very good LEED patterns with sharp spots. However, the low electrical and thermal conductivities of these systems represent a serious restriction for the application of electron spectroscopies, scanning tunneling microscopy (STM), and other experimental methods. Second way of preparation to produce epitaxial thin films is to oxidize a metal (or an alloy) single crystal substrate. This procedure has been successfully applied for Al_2O_3/Al(111), Al_2O_3/ NiAl(111), MgO/Mg(0001), NiO/Ni(111), TiO_2/Ti(0001) and ZnO/Zn(0001) systems [56].

Third way of preparation is typically based on the deposition and oxidation of a metal on an inert substrate single crystal. This method gives the advantage of conducting substrates that are easy to heat (for TPD experiments) or can be utilized by STM, and also good reflectivity permits the usage of infrared reflection absorption spectroscopy (IRAS). The technique has been applied for a large number of oxides like MgO(001), NiO(001), Al_2O_3, SiO_2, Cr_2O_3, FeO, or Fe_3O_4 and others [54].

The preparation of the active particles on a well-characterized model oxide support is the next step for the development of a model catalyst [54]. In many cases, these active particles consist of metal or oxide aggregates. In these systems, the function of the support is not only limited to the dispersion of the catalytically active sites, but also includes a direct modification of the electronic and structural properties of the active sites [56]. Some of the aspects that may be responsible for the specific reactivity of catalyst surfaces are the following:

1- Support Effects: The adsorption strength of adsorbates on the support material and diffusion of these adsorbates through the active particles have a crucial influence on

the catalytic elementary steps. It has been previously shown that, in the case of weak interaction of the reactants with the support, trapping of the reactants by the support occur and this can influence the adsorption kinetics of a Pd/Al_2O_3 model catalyst [57]. It has been observed that most of the reactant molecules adsorbed on Pd particles do not emerge from direct impingement on the particle, but first trapped on the support and then reach the Pd particles through surface diffusion [54]. This is called "capture zone" effect where the flux of adsorbate molecules were enhanced nominally to the active particles [58]. In the case of a strong interaction of the reactants with the support, a part of the reaction can even takes place on the support. The best example is the interaction of NO with an ordered Al_2O_3 surface [59].

"Spillover" (or reverse-spillover process), which involves the transport of active species formed on a first surface onto another surface to form the active species, is also an important mechanistic step in heterogeneous catalysis and the effect of support is strongly included [60]. For instance, spillover of hydrogen is particularly important case since many catalytic reactions involve hydrogen. Chen and White [61] observed four TPD states for the D_2 desorption from Al_2O_3 on a Pt/Al_2O_3; three states of them were attributed to the spillover and only one, the most weakly bond, was observed after D_2 adsorption in the presence of Pt. Spillover can happen from a metal to an oxide, from one metal to another, from one oxide to another, or from a metal oxide onto a metal [60].

Moreover, strong-metal support interactions (SMSI effect) in which metal particles (such as Pd and Pt) strongly interact with a reducible support (such as titania), and covered by the oxide film after heating to elevated temperature, shows how catalyst can be affected from the support material [62]. The SMSI effect was first described in 1978 by Tauster after the observation of the reduction of CO and H_2 uptake on the catalyst upon high temperature calcinations [63]. Therefore, as a consequence of SMSI, the adsorption capacity of the oxide film is strongly attenuated and this leads to a deactivation of the system. In order to explain this phenomenon, a number of models have been proposed, and TiO_2 was a classical support that has exhibited this behavior in many studies [64]. However, the results which include $Pt/TiO_2(110)$ were fairly conclusive. A successful SMSI model system were recently prepared in which the atomic structure of the encapsulating oxide film could be identified [62]. The system includes Pt particles supported on $Fe_3O_4(111)$ film on a Pt(111) single crystal.

Atomically resolved STM images taken after annealing the system to 850 K reveal that Pt nanoparticles were covered by FeO(111) film which leads to the reduction of CO uptake capacity. The film shows no reactivity in UHV conditions, however, the situation dramatically changes when the reaction is tested in ambient conditions (CO: 40 mbar, O_2:20 mbar and helium as buffer gas. In this case, CO oxidation reaction occurs easily at 430 K. Usually, SMSI is recognized as an attenuated activity, however, in this case, it has a positive effect on the CO oxidation reaction.

2- Electronic Effects: The electronic structure of a supported particle can be different from an extended metal surface due to electronic influences of the support [65]. One of the best examples is concerning with the reactivity of supported Au nanoparticles. Although bulk Au is not reactive, Au nanoparticles anchored on a reducible support show high catalytic activity towards CO oxidation [66]. Later, on $Au/TiO_2(110)$ model system, it was reported that two dimensional Au particles are three times more active than three dimensional or spherical counterparts [67]. Metal aggregates usually exhibits three dimensional morphology when grown on an oxide surface due to surface energetics, however, in the case of Au, metal aggregates were able to grow in two-dimensional. Afterwards, it was theoretically calculated that Au_{20} cluster adsorbed on a MgO(100) film, it keeps three dimensional structure, however, when it is adsorbed on a two layer thick MgO(100) film supported on a Mo(100) metal surface, it adopts a two dimensional structure [68]. These theoretical calculations were later supported experimentally, in which it is shown that Au islands on the 3-layer thick MgO(100) film grown on Ag(100) are all in two-dimensional, and the Au islands on the 8-layer thick film are three-dimensional [69]. The answer for this behavior was provided by the assumption of an electron transfer from the oxide support-metal interface, which considers the ionization potential for an electron from this interface, the electron affinity of the adsorbed Au atom, polarization of the substrate and polaronic distortion of the oxide film [62]. Therefore, the wetting phenomenon of the metal aggregates on a supported oxide film depends strongly on electronic behavior of the bulk material.

In order to investigate the source of electrons that control the wetting phenomena, Au nanoparticles have been grown on 60 layers thick CaO(100) substrate and also same substrate doped with very small percentage of Mo ions [70]. It was observed that while the particles on the pristine substrate were three-dimensional, the particles on the doped

substrate exhibited two-dimensional structure. It is, therefore, concluded that dopants in support materials can be candidates for electron sources to induce two-dimensional growths of metal particles on bulk oxide surfaces which is then responsible for the high activity of two-dimensional structures.

All these findings suggest that, the influence of the support material in a heterogeneous catalysis process is inevitable and in order to develop new and better catalysts, we need to fundamentally understand the surface structure of the catalyst support materials and also the interaction between the catalyst particles and support. Since, silica (together with alumina) is widely utilized support in catalysis, the application of surface sensitive techniques to elucidate the atomic structure and the mechanisms of catalytic reactions on silica based materials remain a crucial task. In order to rationalize fundamental issues about silica at low dimensions, the preparation of the system must be well-suited to the experimental and computational methods available in surface science and features of the bulk counterparts [9]. Therefore, the preparation of a silica thin film with a well-defined structure supported by a metal single crystal substrate has a paramount importance for the investigation of the properties of the silicon oxide based materials.

1.5.1 Silica Films on Metal Substrates

The growth of well-defined silica films on single crystals has been extensively studied in the last two decades. A comprehensive review about silica film growth was recently published by Shaikhutdinov and Freund [9]. A brief summary of this review will be presented below.

1.5.1.1 Silica Films on Molybdenum

Xu and Goodman [71] prepared for the first time metal supported thin silica films by using a Mo(110) substrate. The preparation included the evaporation of silicon at low temperatures (<100 ^{o}C) in oxygen background typically $4x10^{-6}$ Torr. They differentiated silicon and silicon dioxide species based on their characteristic Auger transition energies and line shapes. According to AES data the SiO_2 films could be as thin as 2 Å. As deposited films were amorphous, structurally more ordered films could be obtained by post-annealing, based on the narrowing of the respected infrared reflection-absorption spectra. A few months later, the same group reported the preparation of ultrathin silica

films on a Mo(100) surface [72]. The films characterizations were done by using XPS with respect to the chemical states of silicon and the composition of the film. It has been observed that the as deposited silicon oxide contained predominantly SiO_2 with a small fraction of sub-oxides. Annealing to ~1400 K resulted in a stoichiometric film of SiO_2 which exhibited electronic and structural properties similar to those of vitreous silica.

Later on, Schroeder et al.[73] succeeded the preparation of SiO_2 on Mo(112) substrate in which Mo(112) support could accommodate hexagonal surfaces and the lattice parameter can fit those of the low-index silica surfaces, unlike Mo(110) and Mo(100) substrates. The preparation consisted of four cycles of deposition of 0.5 ML Si onto clean Mo(112) at room temperature and oxidation at first 800 K in $5x10^{-5}$ mbar O_2 for 6 min, then $5x10^{-6}$ mbar O_2 at 1150 K for 20 min. The films exhibited a sharp c(2x2)-Mo(112) LEED pattern, thus indicating the high degree of crystallinity. XPS results [74] of the annealed films showed that silicon in the Si^{4+} state, whereas at least two oxygen species are present in the films which were assigned to Si-O and interfacial Si-O-Mo species. UPS data [75] were consistent with silica compounds with corner-sharing [SiO_4] tetrahedral as a building block.

Goodman and co-workers published a paper [76] discussing the atomic structure of the silica film on Mo(112), where the term "a monolayer silica film" was introduced for the first time. The group used another preparation which is different than the original recipe of Schroeder [73]. In this case the clean Mo(112) surface was first exposed to $5x10^{-8}$ Torr O_2 at 850 K to form the well-ordered Mo(112)-p(2x3)O structure. 1 ML Si was deposited stepwise until followed by annealing at 800 K in a 10^{-7} Torr O_2 for 5 min and then increasing the temperature to 1200 K for an additional 5 min. The phonon bands at 496, 800, and 1176 cm^{-1} which were observed for thicker film were essentially the same as those measured for quartz (0001) surface [77]. These features were assigned to bending, symmetric stretching and asymmetric stretching modes of Si-O-Si [78]. At monolayer and submonolayer coverages the phonon peaks at 496 and 1176 cm^{-1} are replaced by features at 320 and 1048 cm^{-1}.

With the help of high-resolution STM and electronic and vibrational spectroscopies applied to the same sample, in combination with the state-of-the art DFT calculations, two groups [79, 80] in 2005 almost independently elucidated the atomic structure of the monolayer silica film on Mo(112). They came to the conclusion that the structure of a

silica film on Mo(112) consisted of a two dimensional network corner-sharing [SiO_4] tetrahedra. The most useful information was obtained by STM studies [81]. It has been revealed that atomically flat films which can be produced only after annealing at temperatures above 1200 K, shows a honeycomb-like structure with a 5.4 Å periodicity, and line defects are decorated along the [-110] direction of Mo(112). The network model contained no oxygen atoms other than those involved in the O-Si-O and Si-O-Mo linkages. The open honeycomb-like structure of the film allows O atoms occupy "inside" the rings in different adsorption sites on the Mo(112) surface [9]. These "O-rich" structures were examined by DFT [82] which revealed that the stability of the "O-rich" phases increases with high pressure of O_2 at low temperatures.

1.5.1.2 Silica Films on Nickel, Palladium and Platinum

The growth of a single-crystal SiO_2 film on Ni(111) was reported by Kundu and Murata [83]. The preparation procedure included, first the deposition of 3 nm Si film at room temperature on clean Ni(111) surface, then the oxidation at $2x10^{-7}$ Torr O_2 in the presence of atomic hydrogen for 1 h at 350 ^oC. Finally, the sample was further annealed at 800^oC in the oxygen ambient. The resulted film showed a sharp LEED pattern assigned to a $(\sqrt{3}x\sqrt{3})R30^o$ structure. Moreover, the preparation of thinner films was not feasible due to the formation of a polycrystalline silicide phase at the SiO_2/Ni(111) interface.

Recently, the preparation of thin silica films on Pd(100) was reported by Zhang et al. [84]. The silica films were prepared by depositing Si onto a Pd(100) substrate kept at 500 K in $1x10^{-3}$ Pa of O_2. The silica films thicknesses were calculated to be 0.4 and 6.5 nm. XPS study revealed that there is no Pd-silicide formation at the SiO_2/Pd(100) interface, in contrast to the SiO_2/Ni(111) system. The UPS results showed that these films present a similar electronic band structure compared to that of crystalline bulk SiO_2. Medlin and co-workers [85] prepared silica on Pd(111) at sub-monolayer surface coverage using coadsorption of SiH_4 and oxygen. According to their TPD, HREELS, and AES results, surface Si and O react <200 K to form a surface SiO_x layer that is stable up to 950 K.

Furthermore, silica films were also prepared on Pt(111) surface [86].Preparation was done by a low temperature (~100 K) Si deposition onto Pt(111) surface in ~10^{-7} mbar

$O_2$and subsequent annealing at ~1200 K in 10^{-6} mbar O_2. At the initial stage of Si deposition, XPS results indicated a Pt-Si surface intermixing which disappeared upon subsequent oxidation at high temperatures. The IRAS results of the 1 and 2 MLE films revealed the bilayer structure of the resulting film with sharp bands at 1294 and 690 cm^{-1}. The expected monolayer film vibrations (1000-1100 cm^{-1}) were not observed for 1 MLE films. It is therefore indicated that silica films grown only in bilayer on Pt(111) substrate. The STM images showed the formation of a two-dimensional vitreous silica film.

1.5.1.3 Silica Films on Ruthenium

The growth of thin silica films on Ru(0001) was studied very recently by our group [87]. The best quality films were obtained by Si deposition at low temperature (~100 K) on to a 3O(2x2)/Ru(0001) surface and annealing at ~1200 K in 10^{-6} mbar O_2. The intermixing of Si and Ru was prevented by the presence of chemisorbed oxygen. The monolayer film consisted of honeycomb shaped network of tetrahedral Si-O linkages with a 5.4 Å lattice constant, in which every Si forms one Si-O-Ru bond and three bridging Si-O-Si bonds. The IRAS spectrum of this film showed four bands at 1134, 1074, 790, and 687 cm^{-1}, which clearly resembles the IRAS spectrum of $SiO_{2.5}$/Mo(112) films.

The surface symmetry was preserved when the coverage was increased up to 2 MLE. However, IRAS spectra exhibited very sharp and intense (good crystallinity) bands at 1300 and 692 cm^{-1}. High-resolution STM images showed again a honeycomb-like network with a 5.5 Å periodicity, similar to monolayer films. DFT calculations [87] suggested that a "bilayer" structure composed of two monolayers linked together through bridging O atoms is formed. This transformation is accompanied by breaking Si-O-Ru bonds and creating the Si-O-Si linkages. XPS/UPS and DFT [88] studies further showed that the system may exhibit "O-poor" and "O-rich" configurations. The presence of this O atom between silica thin film and Ru considerably lowers the adhesion energy, and results in a repulsive interaction between the oxygen atoms of the silica film and the O atoms on Ru. Therefore, the distance between the silica sheet and metal support may increase depending on O coverage on Ru [9]. The electronic states of the SiO_2/Ru can reversibly vary with the amounts of adsorbed oxygen underneath the

silica film. In principle, the electronic properties of oxide/metal systems can be adjusted without altering the thickness and structure of an oxide overlayer itself [9].

Thicker silica films (>2 MLE) exhibit a three-dimensional network of SiO_4 tetrahedra rather than the layered structures which were observed for mono- and bi-layer films. However, atomic resolution couldn't be reached since STM imaging becomes unstable for thick insulating films.

The silica bilayer grown on Ru(0001) can also be employed to directly visualize structural transformation between crystalline and vitreous phases. This is shown by our institute recently [89] in which the polygonal network in the surface plane can easily be recognized. A histogram exhibited that the ring size, measured as a number (N) of members forming the ring, varies between N=4 and 9, with a maximum at N=6 that represents the pure crystalline structure [9]. The glass transition [90] region extends no more than 1.5 nm, in which two adjacent 6-membered rings were transformed into the 5- and 7- membered rings until the distribution of a pure vitreous ring network is reached. These studies demonstrated that bilayer silica films weakly bound to an underlying support, present the unique possibility to study silicate glasses and the glass transition with atomic precision in real space. Furthermore, the glass formation and transition which are highly debated topic in literature was justified for the first time with imaging techniques.

Although surface properties of silica have been intensively studied, many results are still a matter of debate. This significant amount of inconsistencies between various silica surface studies has been attributed to the different preparation methods [91]. As a result, measurements of surface processes on well-defined, planar silica surfaces grown on a metal support can be useful to resolve many contradictory observations. However, only a few researches have utilized ultrahigh vacuum methodologies to address the interaction of adsorbates with well-defined silica surfaces.

It is therefore the motivation of this thesis to elucidate the gas molecules interaction namely D_2O, CO, D_2 and O_2 with silica ultrathin films. Ru(0001) has been chosen as a substrate due to its weak interaction with the film, which makes this model as a good candidate to study only the properties of silica. The organization of the thesis is as follows. After a general introduction about the most important aspects of the silicon

dioxide in Chapter 1, Chapter 2 will include a description of UHV chamber, the procedure for the film preparation, and a brief explanation of the analytical methods applied in this work. The results of this study will be summarized in three chapters and the motivation of the related study will be explained at the beginning of each chapter. Chapter 3 contains the interaction of the water with SiO_2/Ru(0001) model system, mainly the conditions for the formation of silanols and the reactivity of these silanols towards CO and NH_3 gas molecules. The interlayer space between the silica sheet and the metal surface was utilized for the diffusion of adsorbed species mainly CO and D_2, and these results will be discussed in Chapter 4. Chapter 5 will introduce the adsorption of O_2 on silica bilayer and as a result, formation of catalytically active ruthenium oxide underneath silica sheet. A conclusion of this study will be given in Chapter 6.

2. Experimental

2.1 The UHV System

The experiments carried out in this work have been performed in a stainless steel UHV chamber with a base pressure of $2x10^{-10}$ mbar (Figure 2.1). The vacuum in the chamber is maintained by a turbomolecular pump (*Leybold Turbovac 340 M, 400 l/s for N_2*) backed by a small turbomolecular pump (*Pfeiffer D 35614 Asslar, 60 l/s*) and by a rotary pump (*Edwards, 96.7 l/min*) which generate a pressure 10^{-7}-10^{-6} mbar. In order to reach UHV levels, the chamber is baked at 130 ^{o}C for ~48 hours while running titanium sublimation pump (*TSP*) at least 5 times in every 1 hr. The pressure in the chamber is monitored by a Bayard-Alpert type nude ionization gauge (10^{-10} -10^{-4} mbar) and a Pirani gauge (5 x 10^{-4} -1000 mbar). The gas line system is pumped by a small turbomolecular pump (*Pfeiffer D 35614 Asslar, 60 l/s*) and by a rotary pump (*Edwards, 96.7 l/min*). The pressure in the gas line system is monitored by two Baratron gauges (0-10 mbar ; 10-1000 mbar) and a cold cathode gauge (10^{-7}-10^{-3} mbar). Three different types of gasses can be introduced to the chamber by two pinhole dosers. A separate line directly connected to the chamber through a leak-valve allows argon backfilling in order to clean the sample by sputtering.

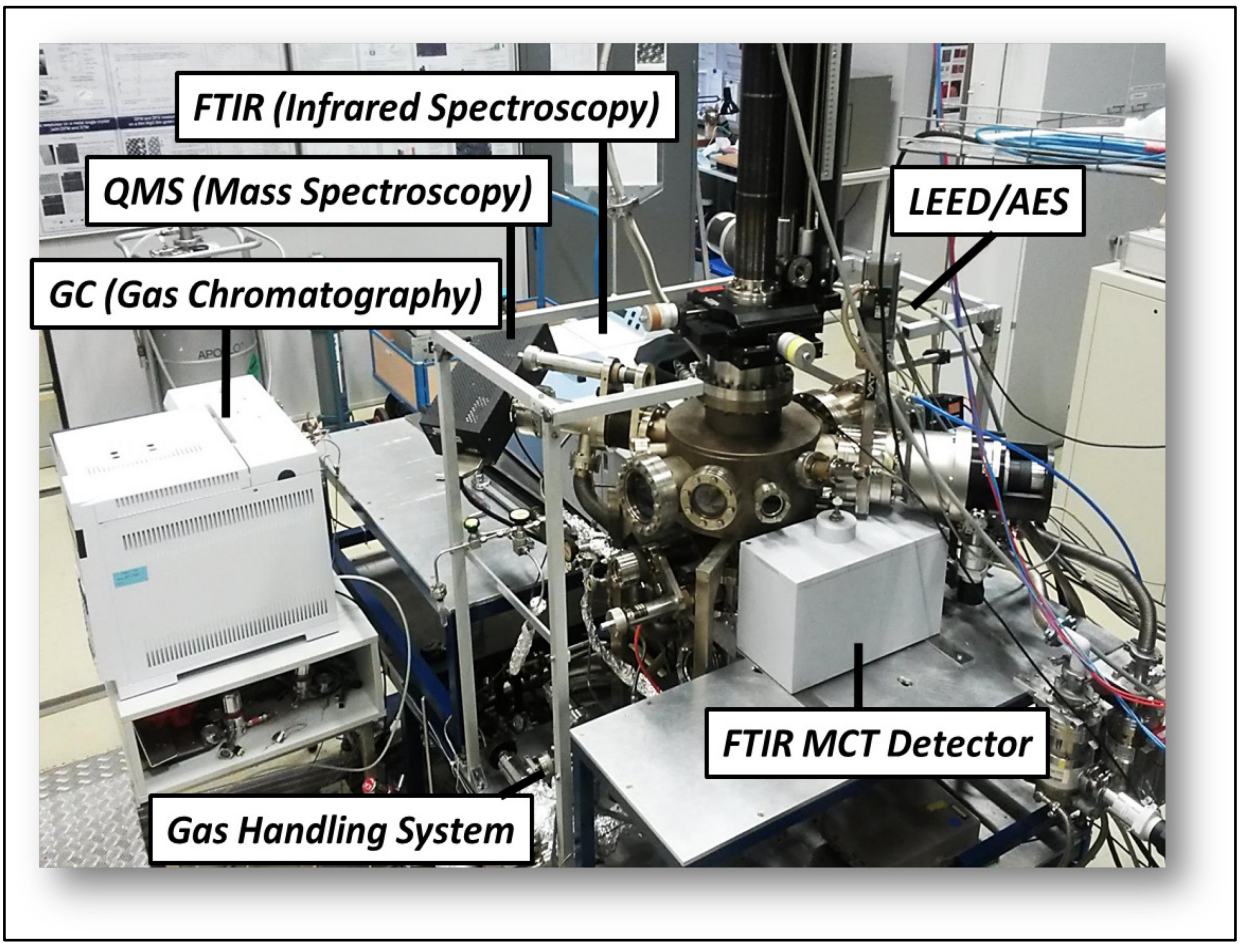

Figure 2.1: The UHV set-up that is used in this study.

The UHV chamber consists of the following instruments and parts:

- Fourier Transform Infrared Spectrometer (Bruker IFS 66v/s) in order to detect the vibrations of molecules adsorbed on planar surface in reflection mode.
- Quadrupole Mass Spectrometer (QMS)(Hiden Analytical) to perform temperature-programmed desorption (TPD) studies
- Gas Chromatography (Agilent 7890 A) (equipped with Ansyco GmbH circulating pump) to separate and analyze the reaction products at atmospheric pressures.
- Low-Energy Electron Diffraction (LEED) optics combined with Auger Electron Spectroscopy (AES) (Omicron) which is used to obtain information about surface structural and chemical analysis.

- An electron-beam assisted evaporator (Focus-EFM 3T) for metal deposition.
- A sputter ion gun for the surface cleaning with a high-energy argon-ion beam.
- Two directional gas dosers

The metal substrate used in this work is a single-side polished Ru(0001) single crystal (10mm diameter, 1.5 mm in thickness) spot-welded to tungsten sticks (ϕ 2.5 mm) through two parallel tantalum wires (ϕ 0.4 mm) which were used for resistive heating. The temperature was measured by type K thermocouple (chromel-alumel) spot-welded to the backside of the crystal. The temperature could be varied between 90 K and 1500 K.

Physical vapor deposition (PVD) method was applied in order to produce thin films with electron beam assisted metal evaporator (*Focus-EFM 3T*). Clean substrate surface was obtained by several cycles of Ar^+ ion bombardment (5-7 μA ion current) with a custom design sputter ion gun and annealing at 1450 K for at least 10 min.

The reactivity studies and high pressure treatments were carried out in a special designed "high-pressure" reactor cell, which is mounted at the bottom part of the UHV chamber (Figure 2.2). The body of the high-pressure reaction cell consists of a 2.75 in. stainless steel conflate cube with a volume of ~30 ml. The reactor cell walls are gold coated in order to avoid side reactions on the walls. It is connected to the main chamber with a straight-through stainless steel membrane seal which is separated from UHV with a Viton O-Ring. The configuration of the manipulator rod is arranged such that the sample vertically moves inside the cell and the end of the manipulator rod fixes on Viton ring to allow pressure seal. A 2.75 in. quartz conflate windows is located on the front of the cube in order to be able to heat the sample from outside with a high power halogen lamp. The reaction cell is evacuated with a high throughput 70 l/s turbo pump and the pressure is measured by a cold cathode gauge. A gas chromatograph (7890 A GC) connected by gas lines to the HP cell allows monitoring gas composition and the reaction kinetics. Facilities allow for introducing gases to high pressure cell and sending gases from this cell into the gas chromatograph for catalytic product analysis.

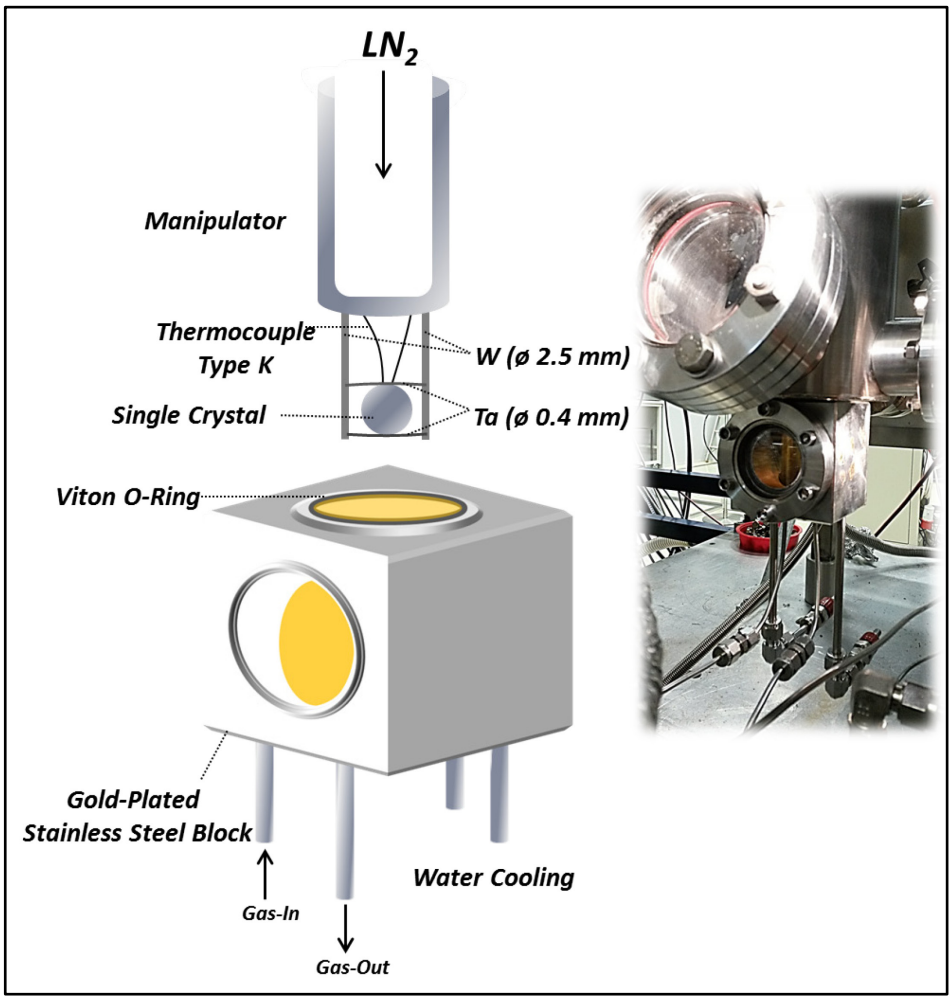

Figure 2.2: High-pressure reaction cell and sample holder design.

2.2 Surface Science Techniques and Principles

2.2.1 Infrared Reflection Absorption Spectroscopy

Vibrational spectroscopy is one of the most powerful techniques to investigate molecular adsorbates that occur on metals during surface chemical reactions. The principle of infrared spectroscopy is based on the interaction of the electric field of the incident infrared light with the dipole moment of the molecule [92]. The vibrational spectra give the information about the chemical nature of the adsorbed molecules to the substrate and adsorbate-adsorbate interactions.

2.2.1.1 Molecular Vibrations

Each atom contains three degrees of freedom. They can move independently along each of the axes of a Cartesian coordinate system. In the case of *N* atoms molecule, there are *3N* degrees of motional freedom. Three of these are the translational ones which involve moving of all atoms simultaneously in the same direction parallel to the axes of a Cartesian coordinate system. Another three degrees of freedom describe rotations in which the distance between the atoms is not changed. The remaining *3N-6* degrees are so called vibrations which change the distance between atoms: the lengths of the chemical bonds and the angles between them.

The simplest model of a vibrating molecule can be approximated by two metal balls connected with spring [93]:

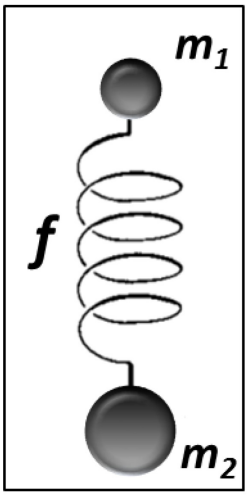

Hooke's law determines the force ***F*** which is necessary to move the atom by a certain distance ***x***from an equilibrium position is proportional to the force constant ***f***:

$$F = -f * \mathrm{x} \tag{2.1}$$

Newton's law states that the force is also proportional to the mass ***m*** and its acceleration, the second derivative of the elongation with respect to the time ***t***:

$$F = m * \frac{d^2x}{dt^2} \tag{2.2}$$

Both equations can be combined:

$$m * \frac{d^2x}{dt^2} = -f * x \tag{2.3}$$

The solution of this second order differential equation results in:

$$x = x_0 * \cos(2\pi\nu t + \varphi) \tag{2.4}$$

which represents the motion of the atom as a harmonic oscillation. In this equation, $\boldsymbol{\nu}$ is the vibrational frequency and $\boldsymbol{\varphi}$the phase angle. The second derivative of $\boldsymbol{x}$ is found to be:

$$\frac{d^2x}{dt^2} = -4\pi^2\nu^2 x_0 \cos(2\pi\nu t + \varphi) = -4\pi^2\nu^2 x \tag{2.5}$$

$$-4\pi^2\nu^2 m = f \text{ or } \nu = \frac{1}{2\pi}\sqrt{\frac{f}{m}} \tag{2.6}$$

This equation gives the frequency of the vibration of a mass connected to a very large mass by an elastic spring. When we consider a diatomic molecule the mass *m* is called a reduced mass of diatomic molecule with the masses $\boldsymbol{m_1}$and$\boldsymbol{m_2}$:

$$\frac{1}{m} = \frac{1}{m_1} + \frac{1}{m_2} \tag{2.7}$$

Then, we obtain an equation describing the frequency of the vibrations of a diatomic molecule:

$$\nu = \frac{1}{2\pi}\sqrt{f\,(\frac{1}{m_1}+\frac{1}{m_2})} \tag{2.8}$$

Equation gives the frequency $\boldsymbol{\nu}$ (in Hz, s^{-1}) of the vibration. In vibrational spectroscopy, it is common to measure "frequencies" in wavenumber units $\tilde{\boldsymbol{\nu}}$ (waves per unit length), which is the reciprocal of the wavelength $\boldsymbol{\lambda}$:

$$\tilde{\nu} = \nu/c = 1/\lambda \tag{2.9}$$

The potential energy of a molecule which obeys Hooke's law is obtained by integrating theeq.2.1:

$$V = \frac{1}{2} f r^2 \tag{2.10}$$

in which $r = x - x_e$, x_e is the Cartesian coordinate of the potential minimum. The graph of this function results in a parabola; which is shown in the Figure 2.3 and it is referred to as a harmonic potential [93].

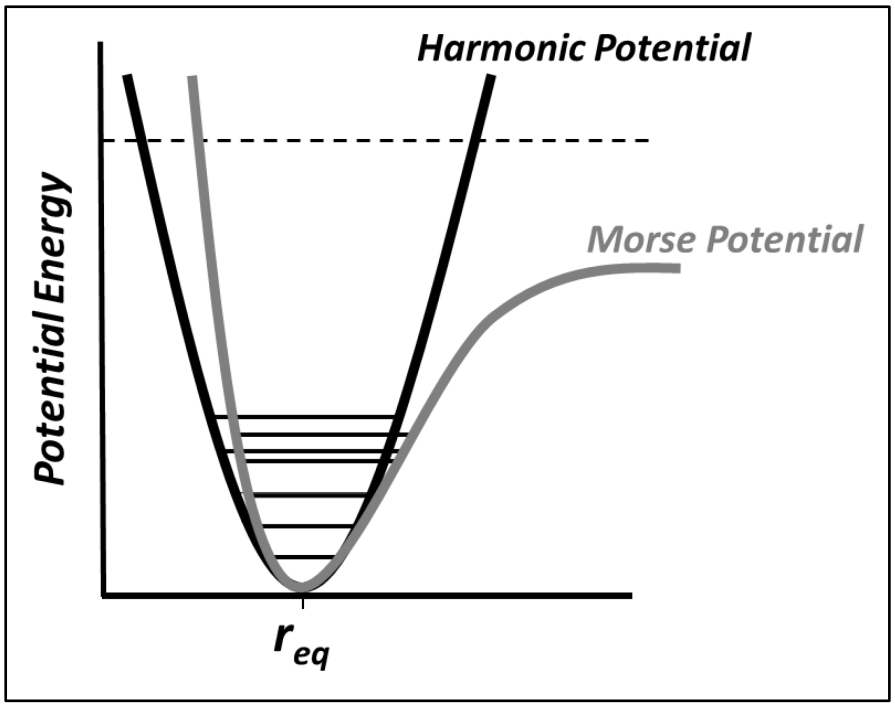

Figure 2.3: Anharmonic (Morse Potential) and harmonic potential with energy states (adapted from [93]).

In the previous discussions, all the assumptions were based on that the vibration of a molecule was purely harmonic and that the dipole moment is a linear function of the displacement from the equilibrium position. If the dipole is not a linear function of the displacement (the vibration is not completely harmonic), the absorption spectra will contain absorption frequencies corresponding to transitions other than the fundamental vibration [94]. Anharmonic potentials may be represented by approximate functions, Morse function (1929):

$$V = D\left[1 - exp\left(\sqrt{-\frac{f_e}{2D}} * r\right)\right]^2 \tag{2.11}$$

$f_e$is the force constant near the potential minimum and D stands for the dissociation energy.

2.2.1.2 The Vibrational Motions of Adsorbates at Surfaces

As we discussed previously, a free molecule has *3N* degrees of freedom which are divided into *3* translational, *3(2)* rotational and *3N-6 (3N-5)* vibrational modes. When an N-atom species is adsorbed on a solid, the translational and rotational modes become vibrational modes [95]. There will be thus *3N* degrees of kinetic freedom on the surface. For example, the vibrations of an OH group bonded to a Si atom bring six additional vibrational degrees of freedom, as indicated in Figure 2.4:

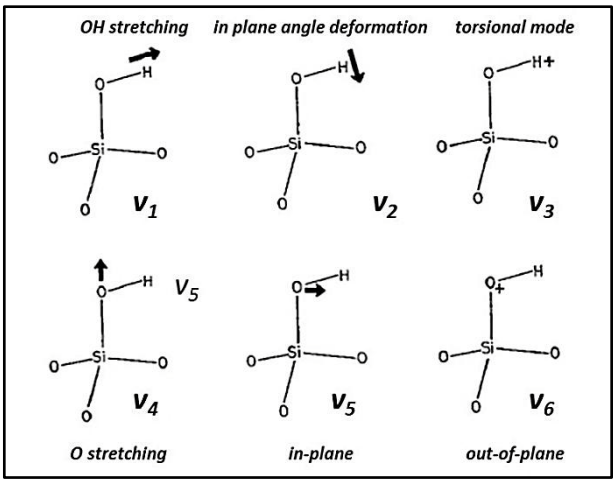

Figure 2.4: The schematic representation of vibration of the surface OH group attached to a silica lattice framework [95].

A necessary condition to probe vibrational modes at the surface is that the component of dynamic dipole moment must be perpendicular to the surface. Quite frequently, totally symmetric representation of the relevant point group corresponds to these modes. This is so called “surface selection rule” and it is directly equivalent to the image dipole theory. The image dipole theory of the surface selection rule is shown in Figure 2.5:

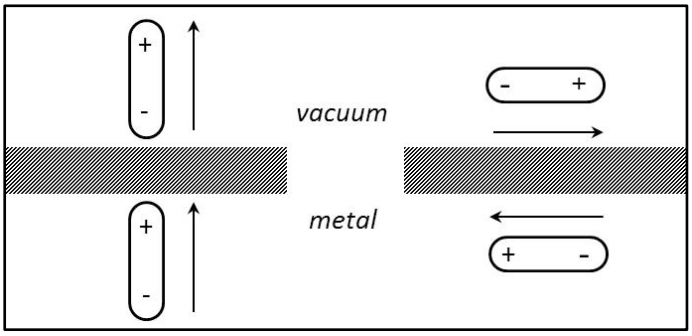

Figure 2.5: The image dipole picture of the molecules resulting an enhancement of a perpendicular dipole, and a dipole orientated parallel to the surface (adapted from [95]).

The electromagnetic field of the infrared radiation cannot distinguish the dipole and its image, and interacts with the sum of their dipoles. In the case of perpendicular dipole, this interaction results in increased response. In the case of a dipole parallel to the surface, two dipoles cancel each other, and no dipole field remains for interaction. Therefore, the dipole moment parallel to the surface plane will not give rise to any spectrum in IR spectrum.

A reflection infrared spectrum of an adsorbed layer can be obtained from the direct measurement of the reflection losses. The absorption of infrared radiation by thin films at a metal surface is enhanced at high angles of incidence and is effectively limited to p-polarized radiation [96].

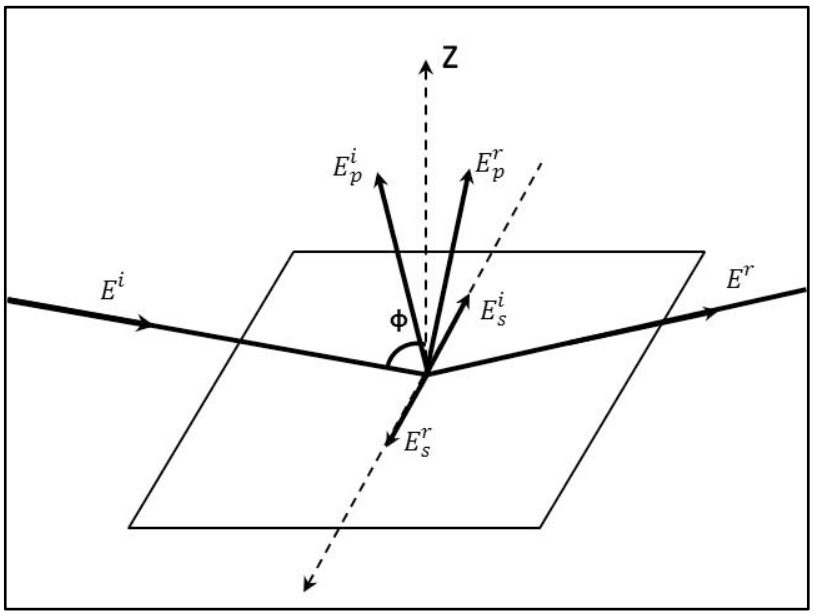

Figure 2.6: The incident (i) and reflected (r) electric vectors of the p- and s- polarized radiation at a metal surface (adapted from [96]).

Figure 2.6illustrates the incident and reflected vectors of s- and p- polarised radiation. Francis and Allison [97] calculated the intensity of reflected IR light by using Fresnel's equation with the index of refraction $\check{\mathbf{n}} = \mathbf{n} + \mathbf{i}\boldsymbol{k}$ by assuming $\mathbf{n}^2 + \mathbf{k}^2 \geq \mathbf{1}$:

$$R_s = \frac{(n - sec)^2 + k^2}{(n + sec)^2 + k^2} \tag{2.12}$$

$$R_p = \frac{(n - cos)^2 + k^2}{(n + cos)^2 + k^2} \tag{2.13}$$

$$\tan\Delta = \tan\left(d_p - d_s\right) = \frac{2\,k\,tan\,sin}{tan^2 - (n^2 + k^2)} \tag{2.14}$$

where$\boldsymbol{R_s}$and $\boldsymbol{R_p}$ are the reflected intensities for s- and p- light, $\boldsymbol{d_s}$ and $\boldsymbol{d_p}$ are the phase shifts upon reflection, $\boldsymbol{\phi}$ is the angle of incidence and $\boldsymbol{E_p}$ and $\boldsymbol{E_s}$ are the electric field components parallel and perpendicular to the plane of incidence. By calculating these equations, results for a typical metal are given in Figure 2.7:

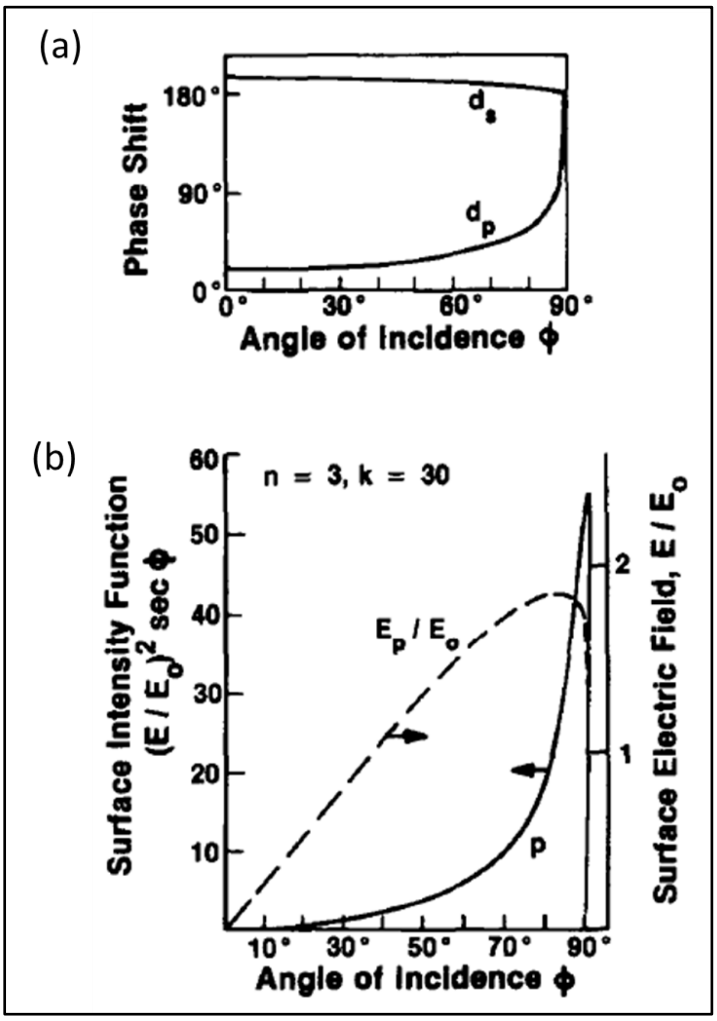

Figure 2.7: Reflection of IR light at a clean metal surface. (a) Phase shifts d_s and $d_p$versus angle of incidence ϕ. (b) Electric field and intensity of p-light versus angle of incidence ϕ [92].

It can be seen from Figure 2.7athat, the s-component of the electric field at the surface has a uniform phase shift of 180^o for all angles of incidence, therefore its electric field disappears at the surface due to destructive interference.However, the phase shift for p-component doesn't suffer a phase shift and large intensity field E_p can be obtained at grazing incidence [92]. This has been shown for copper metal (n=3, k=30) at a frequency of 2000 cm^{-1}(Figure 2.7b)[98] which results in a function for the surface intensity $E_p^2 sec\phi$ that says that the intensity of absorption depends on the square of the surface electric field E_p and on the number of molecules over which the field is exerted. This function has a sharp peak near to high angles of incidence ($85^o \leq \phi \leq 80^o$). Therefore, the interaction of the p-component with vibrational modes of surface species is only limited to the dipoles perpendicular to the surface.

In typical IRAS experiment, infrared radiation is guided from a Globar source through a series of gold coated mirrors towards the metal surface. The incoming photons interact with the surface molecules and reflect from the substrate where they are directed and focused into the detector with another series of gold coated mirrors. The technique is based on the idea of the interference radiation between two beams to yield an *interferogram.* This is a signal produced as a function of the change of pathlength between the two beams [99]. The distance and frequency domains are interconvertible by the mathematical method of *Fourier-transformation*.

The geometry of IRAS system that is being used in this study is shown in Figure 2.8:

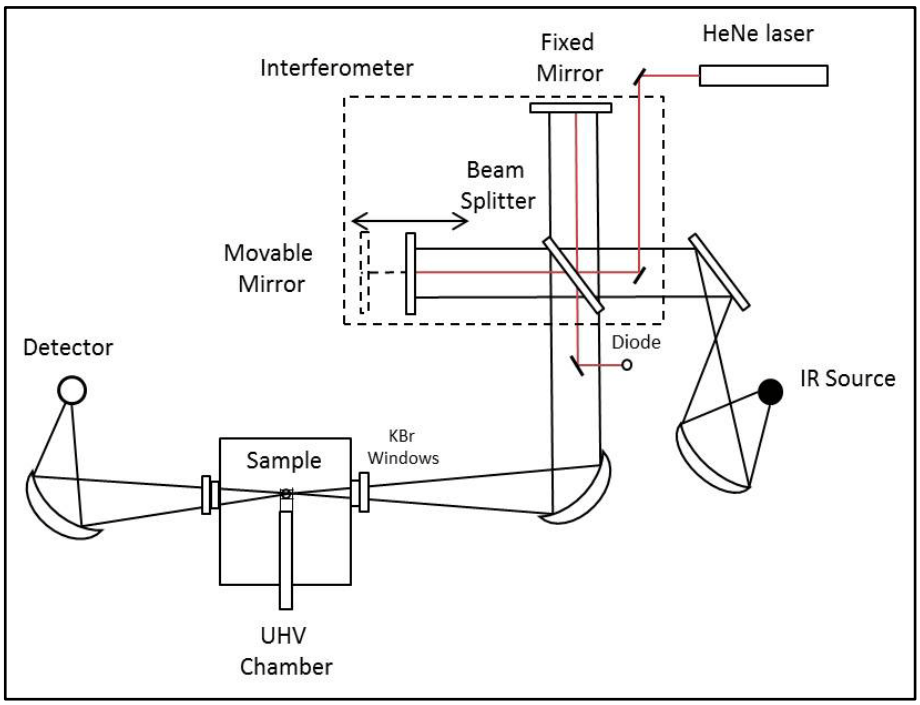

Figure 2.8: Schematic representation of the FTIR set-up that is used in this study.

UHV compatible IR windows, in this case are KBr windows. These windows are completely transparent in the mid-infrared region with low-energy cut-off 400 cm^{-1}[99]. The spectrometer and detector optics are fixed in their aligned position, but both the support table of spectrometer and optics allow final optimization via manual adjustment in z-plane.

The infrared source is a globar, consisting of a silicon carbide rod resistively heated with a direct current. These sources can be utilized in atmosphere at temperatures of up

to ~1500 K, but are mostly run at ~1300 K [99]. In order to sustain the source lifetime and stability, a water-cooling system is operated.

A mercury cadmium telluride (HgCdTe) which is a ternary semiconductor (energy bandgap between 0-1.5 eV at room temperature) is used as a detector. Photons with energy greater than the semiconductor band-gap energy excite electrons into the conduction band, thereby increasing the conductivity of the material. The MCT detector has to be cooled to temperatures as low as 77 K, in order to reduce noise due to thermally excited current carriers.

The most common interferometer used in infrared spectrometry is a *Michelson interferometer*, which consists of two perpendicularly plane mirrors, one of which can travel in a direction perpendicular to the plane. A *beamsplitter* bisects the planes of these two mirrors. When a beam of monochromatic radiation of wavelength λ *(cm)* is passed into a beamsplitter, 50% of the incident radiation will be reflected to one of the mirrors while 50% will be transmitted to movable mirror. These two reflected beams then return to the beamsplitter where they combine and interfere. Transmitted beam is the fifty percent of the beam reflected from the fixed mirror through beamsplitter while 50% is reflected back in the direction of the source. The beam which is detected by the infrared spectrometry is the transmitted beam. The moving mirror produces an optical path difference between the two sides of the interferometer. The intensity as a function of the path length difference in the interferometer p and wavenumber $\tilde{\nu} = 1/\lambda$ is [100]:

$$I(p,) = I()[1 + \cos(2\pi p)] \tag{2.15}$$

where $I(\tilde{\nu})$ is the spectrum to be determined. The total intensity at the detector can be calculated by Fourier cosine function:

$$I(p) = \left(p, \int_0^\infty I(p,)d\right) = \left(p, \int_0^\infty I()[1 + \cos(2\pi p)]d\right) \tag{2.16}$$

Our desired result can be calculated in terms of the measured quantity $I(p)$:

$$I() = 4\int_0^\infty \left[I(p) - \frac{1}{2}I\,(p = 0)\right]\cos(2\pi p)dp \tag{2.17}$$

Throughout this study, IRAS results were plotted as the energy-dependent reflectance relative to that from the same sample prior to gas adsorption. Therefore, the appearance of new species was indicated by negative signals, the disappearance of pre-existing ones resulted in positive signals.

2.2.2 Temperature Programmed Desorption

Temperature-programmed desorption (TPD) technique is used to determine the kinetic and thermodynamic parameters of desorption processes or decomposition reactions on surfaces. The technique involves heating of a sample with a temperature program $\beta(t)=dT/dt$ (Temperature, T is the linear function of time) and measuring the partial pressures of atoms and molecules evolving from the sample by mass spectrometry [101].

Activation of a reactant molecule by adsorption onto catalyst surface is the essential step in a heterogeneous catalytic reaction. The activation step requires that a fairly strong chemical bond is formed with the catalyst surface. This type of adsorption is called chemisorption, and it is characterized by an enthalpy change typically greater than 80 kj mol^{-1}[102]. Due to the chemical bond formation with the catalyst surface, chemisorption is specific meaning that only certain adsorbate-substrate combinations are possible. There is only a single layer, or monolayer, of adsorbed molecules is possible since every adsorbed atom or molecule forms a strong bond with the surface. When the available surface sites for adsorption are occupied, no additional molecules can be chemisorbed.

Every molecule can weakly interact with any solid surface through van der Waals forces. The enthalpy change of this kind of interaction is typically 40 kj mol^{-1} or less [102]. Although physisorbed molecules are not activated for catalysis, they can make a contribution as precursors to chemisorbed molecules. A multilayer formation of molecules is possible in physisorption, since only van der Waals interactions are involved.

As an example, the potential energy diagram for the chemisorption of hydrogen atoms on nickel is schematically shown in Figure 2.9:

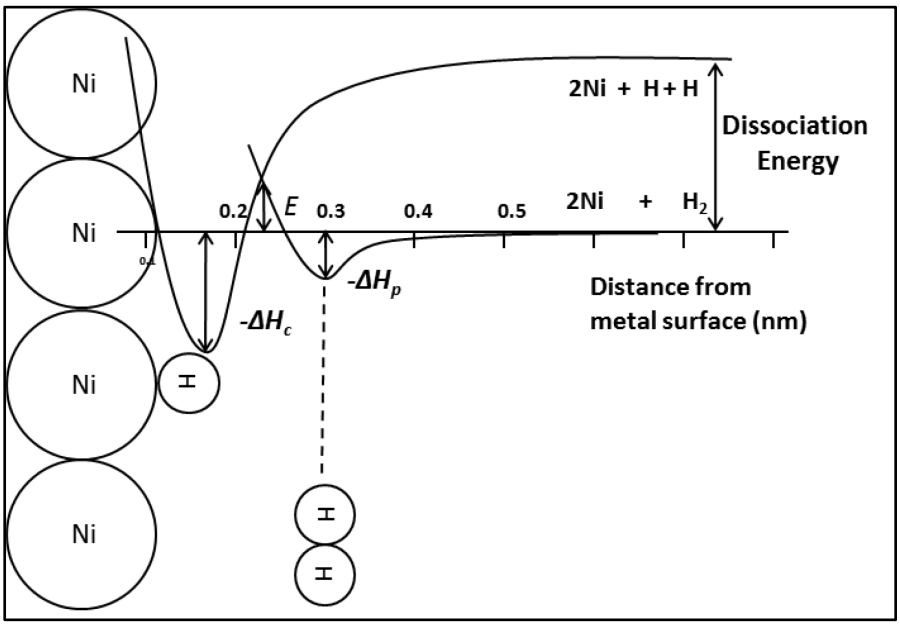

Figure 2.9: Potential energy diagram for the chemisorption of hydrogen on nickel (adapted from [102]).

As molecular hydrogen approaches the surface, it is captured in a potential energy associated with the physisorbed state having an enthalpy of physisorption ΔH_p. The hydrogen atoms chemisorbed on Ni is associated with enthalpy ΔH_c. An activation barrier to chemisorption, E, must be overcome to reach a chemisorbed state from the physisorbed molecule. Since molecular hydrogen dissociates on the surface to form chemisorbed hydrogen atoms, this phenomenon is known as *dissociative chemisorption*.

The sketch of a typical TPD experimental study is shown in Figure 2.10. A cone shaped nozzle has been used in order to reduce the parasitic signals from the heating wires and sample holder. The sample which is <1 mm away from the nozzle of mass spectrometer is heated resistively 1-5 K per second. Furthermore, the instrument consists of a differential pumping system which was designed to facilitate TPD experiments free from the interfering reactions that occur inside the mass spectrometer.

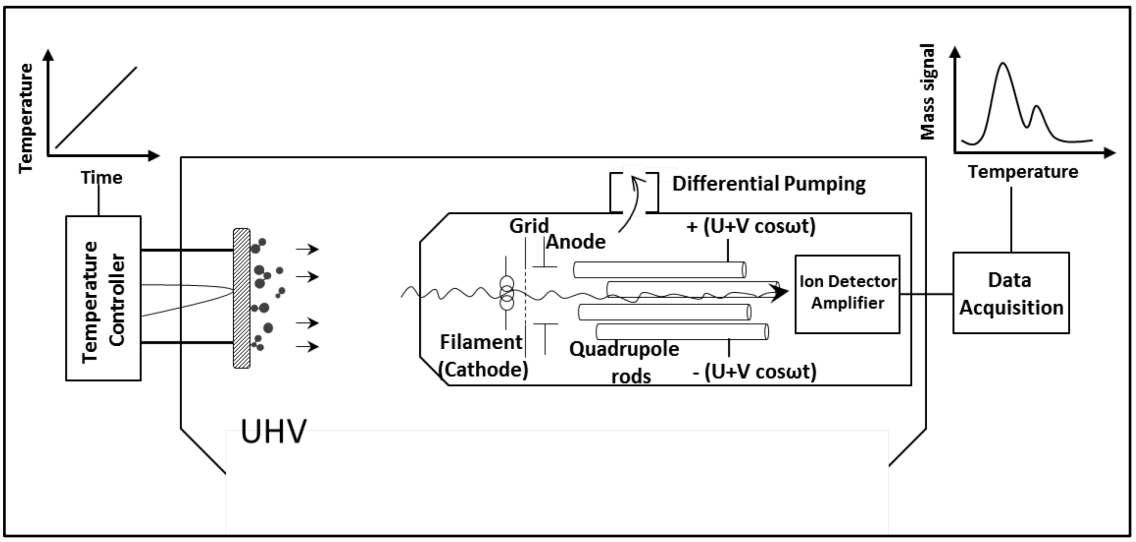

Figure 2.10: Experimental set-up for temperature-programmed desorption studies in ultra-high vacuum (adapted from [101]).

The pumping speed of the main chamber should be high enough to prevent readsorption of the desorbed species back onto the surface. The quadrupole mass spectrometer (QMS) measures the concentration of desorbing species. The QMS consists of three components, (i) the ion source with electron impact ionizer (ii) the quadrupole analyzer consisting of four cylindrically rods (ii) the ion detector (electron multiplier). An electrically heated tungsten filament is the source to produce free electrons that are accelerated by a potential difference (typically 70 V) between the filament and grid. Ionization of the desorbing gas molecules takes place in this region. An electric field then accelerates the positive ions from the front of the QMS into the mass selector region which contains four parallel cylindrical metal rods with the two rods opposite of each other having equal and opposite voltages. The voltages of the electrodes are varied by using an RF oscillation, allowing only ions with a specific mass to charge *(m/z)* ratio to reach the detector.

The interpretation of the spectral data is most commonly performed by the use of the *Polanyi-Wigner* equation [103]. It states that the rate equation for desorption of a gas from a surface in chemical kinetics depends on the concentration of adsorbed molecules per unit surface ***N*** (i.e. coverage) and the temperature ***T***[104]:

$$\frac{dN}{dx} = -k_d N^n \tag{2.18}$$

The rate of desorption is the derivative of ***N*** with respect to time is, ***n*** is the order of desorption, and $\boldsymbol{k_d}$ is the rate constant. *Arrhenius* equation gives the dependence of the rate constant on the temperature and activation energy [105]:

$$k_d = v_n exp(-\frac{E_{des}}{RT}) \tag{2.19}$$

where***T***is the temperature, ***v*** is the pre-exponential factor, ***r***is the ideal gas constant and $\boldsymbol{E_{des}}$ is the activation energy. By substituting *Arrhenius*equation into *Polanyi-Wigner* equation, the rate of desorption from a unit surface area can be written as:

$$\frac{dN}{dx} = -v_n exp(-\frac{E_{des}}{RT})N^n \tag{2.20}$$

When the temperature is linear, $T = T_0 + \beta t$

$$\frac{dT}{dt} = \beta \tag{2.21}$$

Solving for***dt*** and substituting into *Polanyi-Wigner* equation gives the rate of desorption as a function of temperature and heating rate:

$$\frac{dN}{dT} = -\frac{1}{\beta} v_n exp(-\frac{E_{des}}{RT})N^n \tag{2.22}$$

Zero order kinetics *(n=0)* means that the desorption rate does not depend on coverage and also implies that desorption rate increases exponentially with T, which occurs when species desorb from multilayers.

First order reaction means that $\boldsymbol{T_{max}}$keeps constant with increasing coverage and depends on the heating rate of the sample. This occurs when the surface coverage is less than a monolayer. With n=1:

$$N\frac{E_{des}}{RT_m^2} + \frac{dN}{dT} = 0 \tag{2.23}$$

and it can be obtained that

$$ln\left(\frac{R\nu}{E_{des}}\right) + ln\left(\frac{T_m^2}{\beta}\right) = \frac{E_{des}}{RT_m} \tag{2.24}$$

In this equation, note that $\boldsymbol{ln\left(\frac{R\nu}{E_{des}}\right)}$ is a constant, by arranging the eq. 2.18 an equation of a straight line is obtained:

$$ln\left(\frac{T_m^2}{\beta}\right) = \frac{E_{des}}{RT_m} - C \tag{2.25}$$

Activation energies can be calculated by making a $\boldsymbol{ln\left(\frac{T_m^2}{\beta}\right)}$ vs.$\boldsymbol{\frac{1}{T_m}}$ plot and the slope of this graph is ($\boldsymbol{\frac{E_{des}}{R}}$). Moreover, the y-intercept of this plot is equal to $\boldsymbol{ln\left(\frac{R\nu}{E_{des}}\right)}$. Therefore, with the calculation of activation energy; a value for the pre-exponential factor can be obtained [106].

A reaction that is proportional to the concentration of each two molecules is called second order reaction. For a second order kinetic reaction, n=2,

$$ln\left(\frac{T_m^2}{\beta}\right) = \frac{E_{des}}{RT_m} - ln\left(\frac{2\nu RN}{E_{des}}\right) \tag{2.26}$$

In this case, the result is different from the first-order reaction whose $\boldsymbol{T_m}$value does not depend upon the initial coverage, with a second order desorption process, the temperature of the peak $\boldsymbol{T_m}$ will decrease with increasing initial coverage.

Redhead [107] derived an equation to approximate the activation energy of desorption in an accurate way. According to the Redhead`s equation, the rate of desorption (r_d) is proportional to the surface coverage of the adsorbate (θ_A) to the power n (order of the desorption reaction), the number of surface sites (N_s) and the negative of the exponential of the product between the activation energy (E_A), divided by the temperature (T) and Boltzman constant (k). The rate constant's pre-exponential factor is

denoted as (k_0). The activation energy can be calculated from the TPD peak by adding the linear relationship between T and heating time t ($T=T_0+\beta t$):

$$\frac{r_d}{N_s\beta} = -\frac{d\theta_A}{dT} = \frac{k_0}{\beta}\theta_A^n exp\left(-\frac{E_A}{kT}\right) \tag{2.27}$$

2.2.3 Low-Energy Electron Diffraction (LEED)

Diffraction techniques using electrons can be used in order to gain structural information by the analysis of the waves scattered elastically by the crystal. The information on the atomic arrangement within a unit cell can be interpreted by the intensity of the diffracted beams. There are two main reasons for the usage of low-energy electrons for surface analysis systems [108]:

- As the de Broglie wavelength of an electron is given by

$$\lambda = \frac{h}{\sqrt{2mE}}, \qquad \lambda[\text{Å}] = \sqrt{\frac{150}{E(eV)}} \tag{2.28}$$

in the typical range of energies used in LEED (30-200 eV), the electrons have a wavelength (1-2 Å) that fulfills the atomic diffraction condition.

- Since the mean free path of the low-energy electrons is usually short (Figure 2.11), the most elastic collisions occur in the top layers of a sample. Therefore, a 2D atomic structure of the sample surface can be provided by LEED.

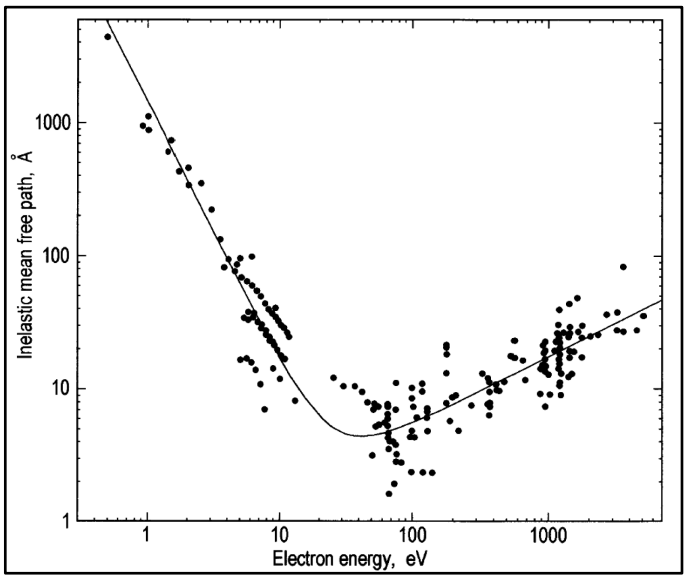

Figure 2.11: Experimental data for the inelastic mean free path of electrons as a function of their energy above the Fermi level [109].

LEED set-up is schematically in Figure 2.12:

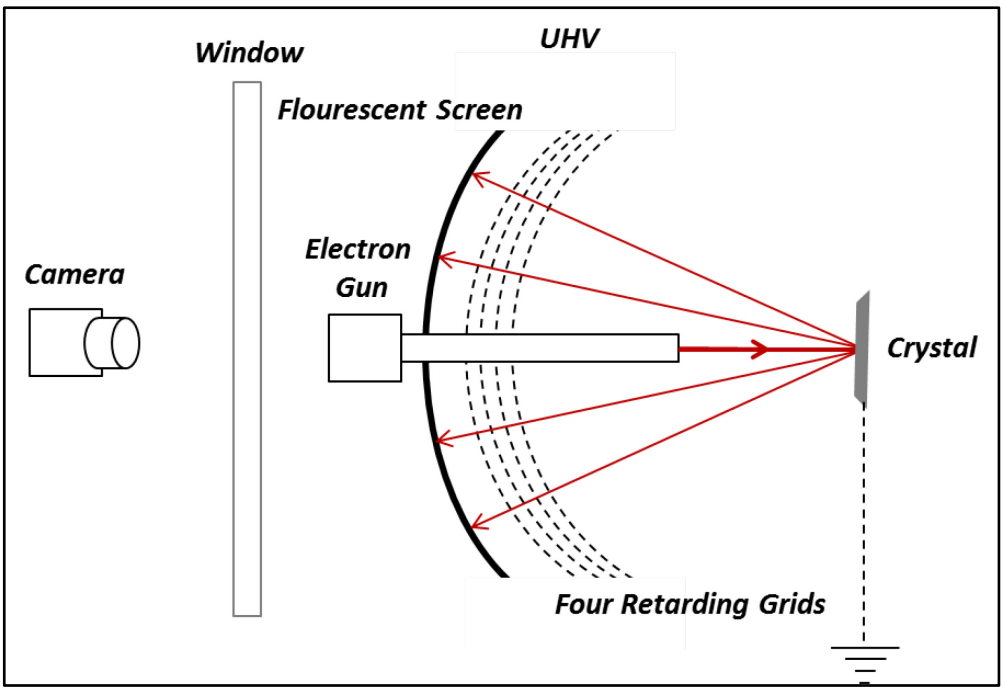

Figure 2.12: Schematic description of LEED set-up (adapted from [110]).

Standard experimental set-up for LEED consists of three main parts: an electron gun to generate a collimated beam of low-energy electrons, a sample holder that allows x, y and z, translations and independent rotations, and a hemispherical fluorescent screen with a set of four grids to investigate the diffraction pattern of the elastically scattered

electrons. The first grid is connected to the earth ground to provide field-free region between the sample and the first grid. This reduces an undesirable electrostatic deflection of diffracted electrons. A negative potential is applied to the second and third grid (suppressor grids) to allow the transmission of the elastically scattered electron to the fluorescent screen in a narrow range. The fourth grid is usually grounded to reduce field penetration of the suppressor grids by the screen voltage when a potential of few kilovolts is applied to the screen in order to make diffraction beams visible. The effective diameter of the electron beam which is produced by a cathode filament with a Wehnelt cylinder is about 1 mm [110].

Since it is the main goal of LEED crystallography to determine surface structures from LEED patterns, it is crucial to study the relation between the symmetry properties of the structure and the observed LEED pattern. The LEED pattern has the same configuration as the so called "reciprocal lattice" [101]. A two-dimensional solid surface contains a primitive unit cell which can be defined by the translational vectors $\overrightarrow{\boldsymbol{a_1}}$ and $\overrightarrow{\boldsymbol{a_2}}$. In this case reciprocal lattice vectors can be written as $\overrightarrow{\boldsymbol{a_1^*}}$ and$\overrightarrow{\boldsymbol{a_2^*}}$**.** The relationships between the primitive translation vectors of the surface,$\overrightarrow{\boldsymbol{a_1}}$ and $\overrightarrow{\boldsymbol{a_2}}$ and the primitive translation vectors of the reciprocal lattice,$\overrightarrow{\boldsymbol{a_1^*}}$ and$\overrightarrow{\boldsymbol{a_2^*}}$ can be written as

$$\overrightarrow{a_1^*} = 2\pi \left[\frac{\overrightarrow{a_2}\, x\, \vec{n}}{\overrightarrow{a_1}\,.\,(\overrightarrow{a_2}\, x\, \overrightarrow{n})}\right] \tag{2.29}$$

$$\overrightarrow{a_2^*} = 2\pi \left[\frac{\overrightarrow{a_1}\, x\, \vec{n}}{\overrightarrow{a_2}\,.\,(\overrightarrow{a_1}\, x\, \overrightarrow{n})}\right] \tag{2.30}$$

when$\overrightarrow{\boldsymbol{n}}$ is taken to be a unit, vector becomes normal to the surface. The most important properties of the reciprocal lattice and the five different surface lattices with corresponding LEED patterns are summarized in Figure 2.13[101]:

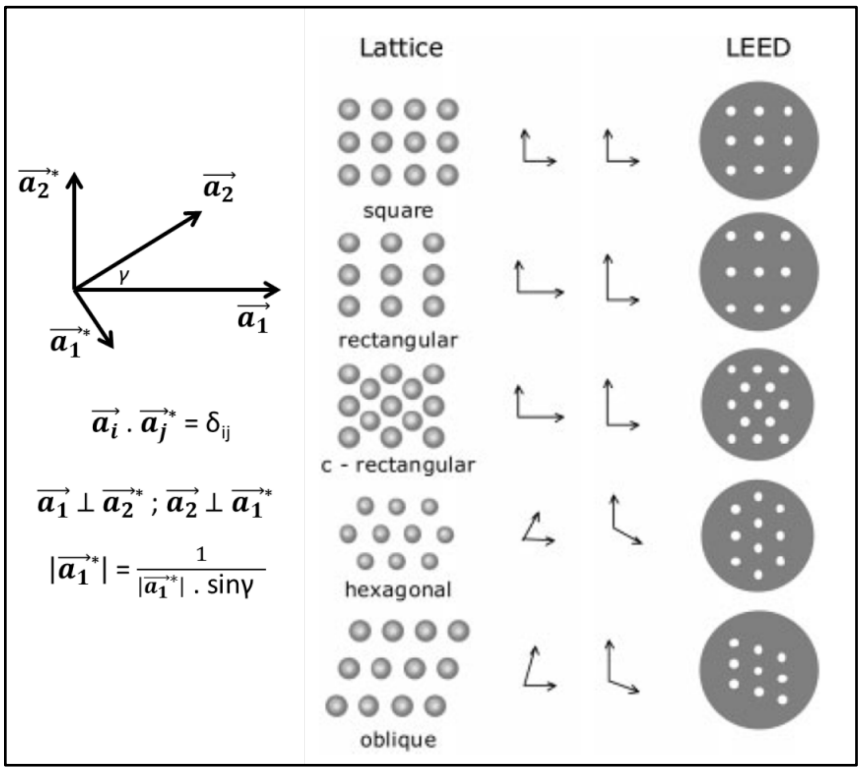

Figure 2.13: Definition and properties of the two-dimensional reciprocal lattice (adapted from [101]).

It is important to note that the base vectors of the surface lattice constitute the smallest parallelogram from which the lattice is constructed through translations. When adsorbed gases form ordered layers with periodical structures, the unit cell of the overlayers can also be determined with LEED. Since the LEED pattern reflects only the periodicity in the layer, the exact position of the adsorbate atoms with respect to the substrate remains unclear [101]. LEED pattern with bright sharp spots and low background intensity comes with the well-ordered surface and the absence of LEED spots indicates a disordered, amorphous, or finely polycrystalline surface [110].

2.2.4 Auger Electron Spectroscopy (AES)

Electron spectroscopy uses the secondary electrons emitted from the sample in order to probe the electronic structure of the surface. The bombardment of the surface with electrons or photons produces these secondary electrons. The typical energy ranges of secondary electrons generally are in between 5-2000 eV [108].

Auger electron spectroscopy which was developed in the late 1960s is one of the most commonly used techniques for the analysis of surface chemical composition by measuring the energies of Auger electrons. The Auger effect was first discovered

independently by both Lisa Meitner and Pierre Victor Auger in 1920s [111, 112]. The technique did not become widely used as a surface tool for more than a decade due to experimental difficulty in retrieving the characteristic Auger features from the large background of inelastically scattered electrons [113]. In 1968, AES was generally accepted after Harris demonstrated that AES analysis could be simply retrieved by differentiating the electron spectrum with respect to energy [114]. The principle of the Auger process is illustrated schematically in Figure 2.14:

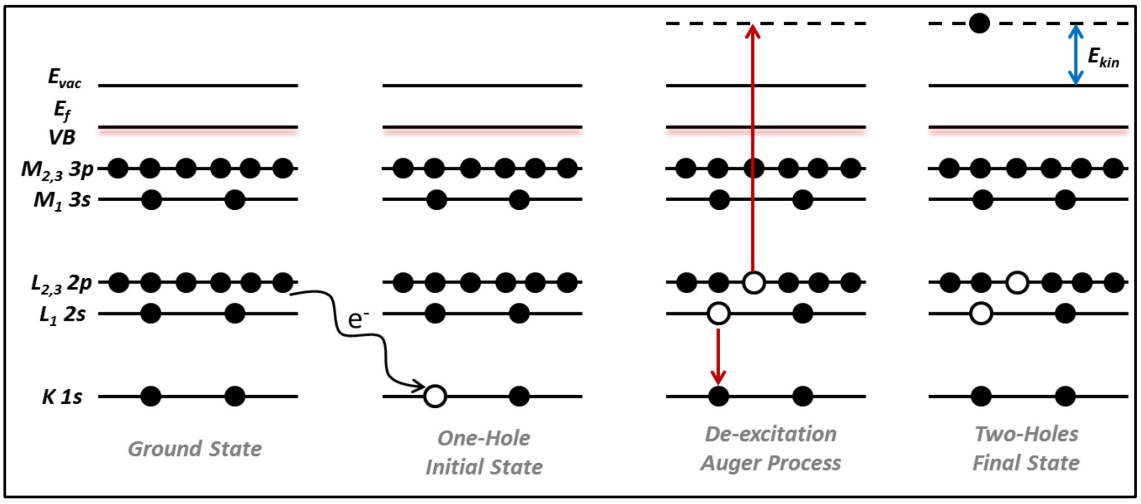

Figure 2.14: Schematic diagram for the illustration of Auger process (adapted from [103]).

The primary electron having energy in the range 2-10 keV creates a core hole by removal of a *K*-shell electron. This hole is filled by an electron from a higher energy level in this case L_1 shell. This ionization creates a highly excited state and will rapidly relax back to a lower energy state by either Auger emission (non-radiative transition) or X-ray fluorescence (radiative transition) [108]. In the case of low-energy transitions (E< 500 eV), principally for lighter elements, x-ray fluorescence becomes negligible and Auger emission is more favored. There are two states in the Auger process, initial (one-hole state) and final (two-hole state) in which three electrons are involved in the transition. Therefore, Auger transitions occur in all elements of the periodic table except for H and He [108].

The location of the initial hole and the location of the final two holes specify the Auger transition, in this example it is a $KL_1L_{2,3}$ transition . The kinetic energy of the ejected

electron for the $KL_1L_{2,3}$ transition can be estimated from the binding energies of the levels [108]:

$$EKL_1L_{2,3} = EK - EL_1 - EL_{2,3} - Ø \quad (2.31)$$

where $Ø = E_{Vacuum} - E_{Fermi}$ is the work function of the material.

The emitted Auger electron is directly related to the nature of the atom that is emitted; therefore elemental identification is possible from the energy positions of the Auger peaks. Moreover, the Auger spectrum contains information on the chemical bonding states of the atoms. When the chemical environment of a certain atom changes, this leads to a redistribution of the electron density of states in the valence band which influences the Auger peak position and/or the peak shape.

The standard equipment for AES consists of an electron gun, energy analyzer and data processing electronics. The primary electron beam that is generated by the electron gun has a typical energy of 1 to 5 keV. The most commonly used energy analyzers are cylindrical mirror, hemispherical, and in our case a four-grid analyzer. The detection of the signal is being recorded with the cylindrical mirror analyzer is in the **dN(E)/ dE** mode at frequency **ω** and **N(E)** mode with the four-grid analyzer. In order to obtain the **dN(E)/ dE** spectra with the latter case, the detection must be done in the frequency **2ω**.

2.2.5 Gas Chromatography (GC)

The pressure gap presents a substantial obstacle for correlating UHV characteristics with actual catalyst mechanisms. A common approach to circumvent the pressure gap is to combine an UHV chamber with an elevated pressure reactor and sample transfer system. The procedure allows being sample treated under realistic conditions by collecting valuable information frequently by gas chromatography method (GC).

Gas chromatography is a technique which uses a gas as the mobile phase, and a solid or a non-volatile liquid as the stationary phase for analyzing and separating compounds. The sample is usually injected as a vapor on to the chromatographic column. Inside the column, the gas phase separation of each component depends on its vapor pressure and the affinity between the compound and the stationary phase. The quality of a separation (resolution) depends on how long the components to be separated stay in the stationary

phase and how often they interact with this phase [115]. Whenever a molecule enters the gas phase, it is directed towards the detector by the carrier gas flow (an inert gas, such as helium). Compounds showing different physical and chemical properties will reach to the detector at different times. Figure 2.15 shows the basic components of the UHV set-up connected to a GC instrument:

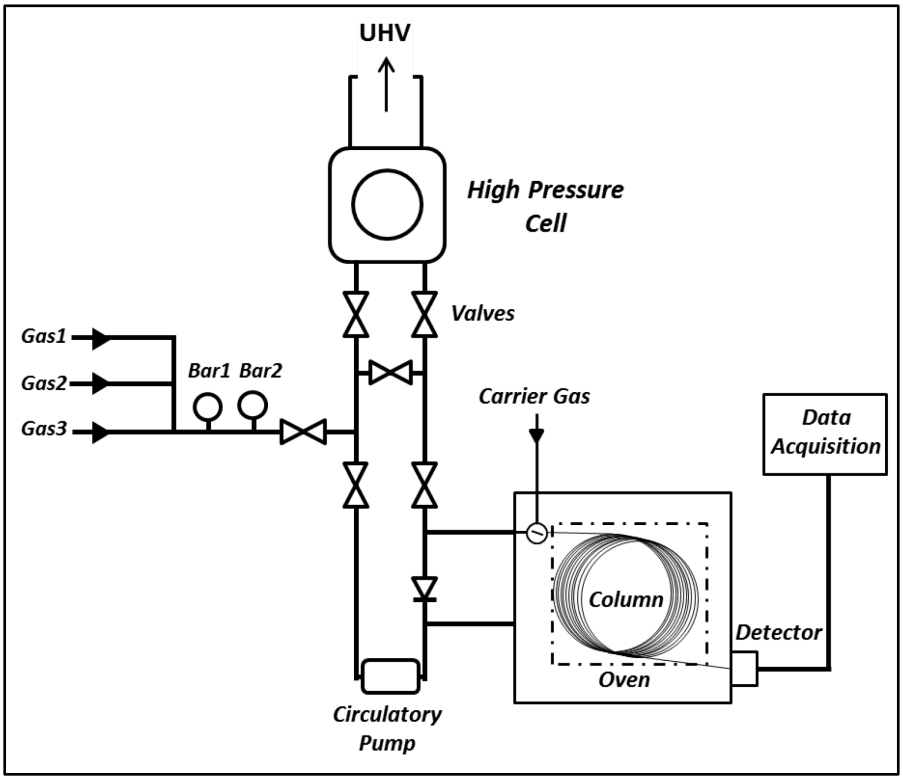

Figure 2.15: The schematic representation of the gas line that is connected to the GC set-up.

Thermal conductivity detectors and flame ionization detectors are commonly used detectors in GC. Thermal conductivity detector senses the changes in the thermal conductivity of the gas leaving the column and compares it with the reference flow of the carrier gas [116]. It consists of four hot tungsten-rhenium filaments that are connected with a Wheatstone bridge arrangement, two filaments place in the exit gas from the column and two in the reference gas stream. When the carrier gas (i.e. helium) which has already same temperature with detector block leaves the column and cools the hot filament. However, a solute mixed with helium emerges; it will cool the filament less. In this case the temperature of the filament will increase and this change in the resistance can be measure. Flame ionization detector (FID) is generally utilized for

detecting organic compounds. The separated gas sample leaving from the column is mixed with hydrogen and air, and is then burned. Hydrocarbon radicals which are formed on combustion are then oxidized and these ions allow a current which are transmitted via a cathode is then converted to a signal [117]. FID is approximately 100 times more sensitive than the thermal conductivity detector for organic materials; however it has no use if the compounds cannot be burned.

Retention time and peak efficiency which describe the ability of the stationary phase to retain a solute are two important parameters in gas chromatography. The time between sample injection and a sample peak reaching a detector at the end of the column is termed the retention time (t_R). It is directly proportional to column length and resolution is proportional to the square root of the column length [118]. The amount of a substance in a sample is proportional to the area under the peak of the substance in analyte. However, each substance and detector has different proportionality constant and therefore, before doing a quantitative analysis, one needs to determine the proportionality constant for each substance in a sample.

In a GC instrument, the performance and response of the chromatograph columns and the detectors are very susceptible to changes in temperature. Therefore, the oven is designed to insulate these components from the effects of ambient temperature changes and maintain a very stable temperature internally. Moreover, the temperature at which the oven is controlled depends on the application: with the heavier hydrocarbon mixture, the oven temperature should be increased.

2.3 Silicate Thin Film Preparation

Figure 2.16 provides an overview of the sample preparation. The film preparation starts with crystal cleaning which is achieved by Ar^+ ion sputtering and annealing at 1400 K for 10 min several cycles. The 3O(2x2)/Ru(0001) surface was prepared by exposing the clean surface to $3x10^{-6}$ mbar O_2 at 1200 K for 10 min and then cooling to 450 K in O_2 ambient. Silicon was deposited onto this O covered surface in $2x10^{-7}$ mbar O_2 using an e-beam assisted evaporator in which 1 mm Si rod of high purity is evaporated. During Si deposition, the crystal temperature is stable at 100 K. The low temperature adsorption can suppress the diffusivity of the atoms on the Ru(0001) surface and therefore can

favor the formation of two-dimensional structures before the final oxidation step. The evaporator is equipped with a flux monitor which allows calibrating the silicon atom flux. In order to achieve stable 10 nA Si flux, 900-950 V on the Si rod and 2.3 A filament current are needed. For the oxidation step, Si deposited Ru(0001) crystal is heated to a temperature of 1200 K for 10 min while the crystal surface is exposed to an oxygen partial pressure of $3x10^{-6}$ mbar. The idea of having chemisorbed oxygen on Ru(0001) surface prior to Si evaporation is to prevent intermixing between Si and Ru. Previous XPS results show that the 3O(2x2) layers are consumed upon silicon deposition. As a consequence, this can further assist to the oxidation of silicon at the initial stages of film preparation [119].

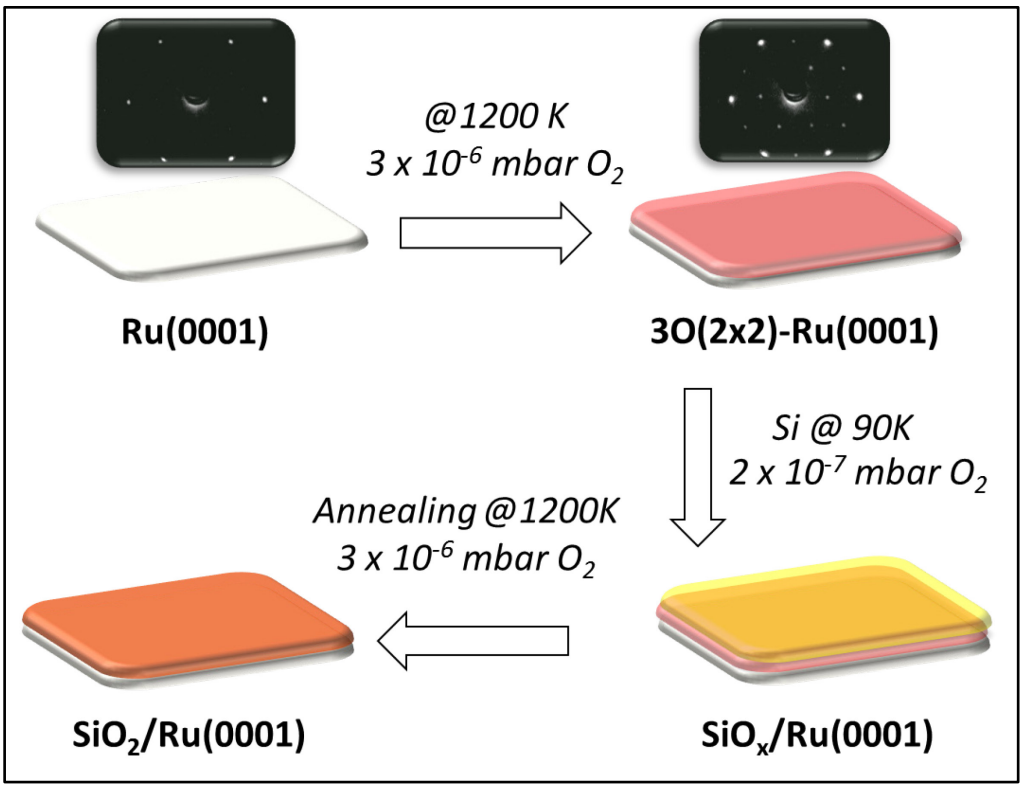

Figure 2.16: Overview of silica film preparation.

The deposition of 3 min Si and oxidation results in 1 MLE film which exhibits (2x2) LEED pattern (Figure 2.17). STM images of the monolayer film show that the surface becomes almost covered by the silica film in which honeycomb-like structure with a 5.4 Å periodicity can be found [119]. IRA-spectrum of the resulted film shows peaks at 1135, 1072, 787 and 685 cm^{-1} in which 1135 cm^{-1} feature dominates the spectrum. This spectrum shows similar features with the one reported for $SiO_{2.5}$/Mo(112) films in which a sharp and intense band at 1060 cm^{-1} assigned to the stretching vibrations of the

Si-O-Mo linkage, weak signals at 770 cm^{-1} assigned to Si-O-Si symmetric stretching mode coupled with Si-O-Si bending mode and 675 cm^{-1} assigned to coupling of Si-O-Si bending modes [79]. Therefore, a similar growth-mode for silica films over Ru(0001) was suggested for monolayer film in which every Si makes one Si-O-Ru bond and three bridging Si-O-Si bonds. In this case, 1135 cm^{-1} is assigned to the in-phase combination of asymmetric stretching vibrations of the Si-O-Ru linkages and 1060 cm^{-1} comes from the combinations of symmetric O-Si-O stretching vibrations. Low frequency vibrations at 787 and 685 cm^{-1} are the combinations of asymmetric stretching of Si-O-Ru linkages and O-Si-O bending modes.

DFT results indicate that; only the film containing two O/Ru atoms per unit cell is found to be stable (Figure 2.17). An auger spectrum of the corresponding film is taken after the final oxidation step. There are three main peaks at 82.6, 280 and 517 eV in the spectrum. The peak at 82.6 eV is expected for the SiO $L_{2,3}VV$ transition [120, 121]. Absence of 92 eV feature which is assigned to $L_{2,3}VV$ transition of elemental Si suggest that the film is completely oxidized. Four peaks located from 150 to 280 eV correspond to Ru MNN transition which is attenuated upon Si deposition. Oxygen peak of the KLL transition is found around 517 eV.

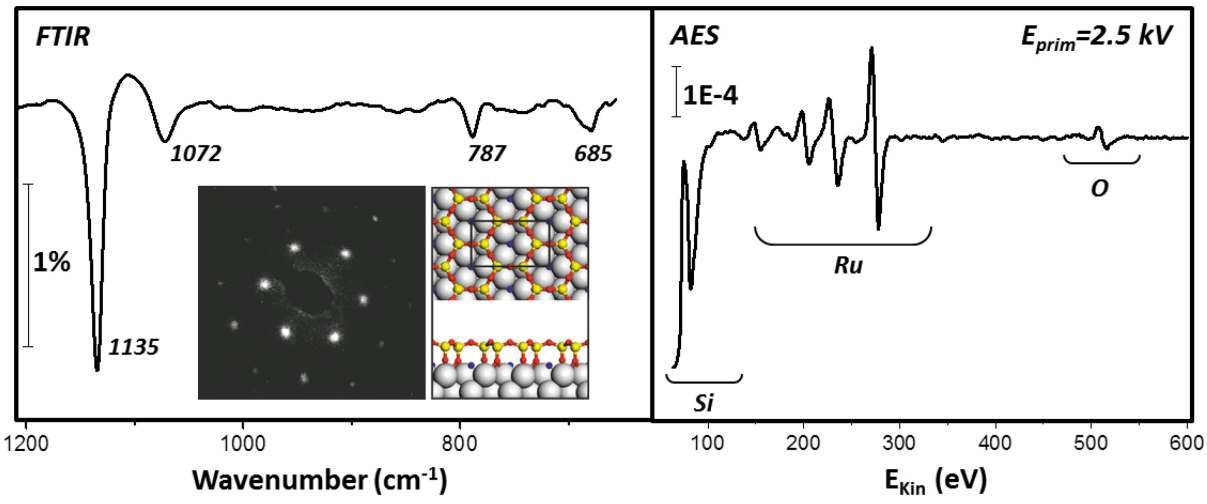

Figure 2.17: IRA spectrum and AES spectrum of the 1 MLE film. LEED pattern of the 1 MLE film and corresponding model is given next to LEED [119].

6 min deposition of silicon and the oxidation at the same conditions results in a bilayer film which shows (2x2) LEED pattern and two rings around them. (2x2) pattern is a result of crystallinity (Figure 2.18). However, ring like structure is caused by amorphous

features in the silica film. Therefore, most of the bilayer films that are prepared in this study is a mixture of both ordered and disordered phases. STM analysis of disordered film exhibits a pore size distribution ranging from 4 to 9 in which [SiO_4] tetrahedral structures are connected to each other by corner sharing [119]. The IRAS measurements showed two intense bands at 1296 and 690 cm^{-1} with the corresponding vibrational modes in model. Blue spectrum corresponds to a silica bilayer film prepared by using $^{18}O_2$. Transformation from monolayer to bilayer occurs by breaking Si-O-Ru bonds while creating Si-O-Si linkages. AES spectra exhibits two peaks in the Si region 81 eV (Si $L_{2,3}V_1V_1$) and a satellite at 65 eV (Si $L_{2,3}$ V_2 V_1) which reflect fully oxidized SiO_2 valence band [74]. Further attenuation of Ru MNN peak is followed by an increase of the oxygen KLL peak at 517 eV by Si deposition and oxidation steps.

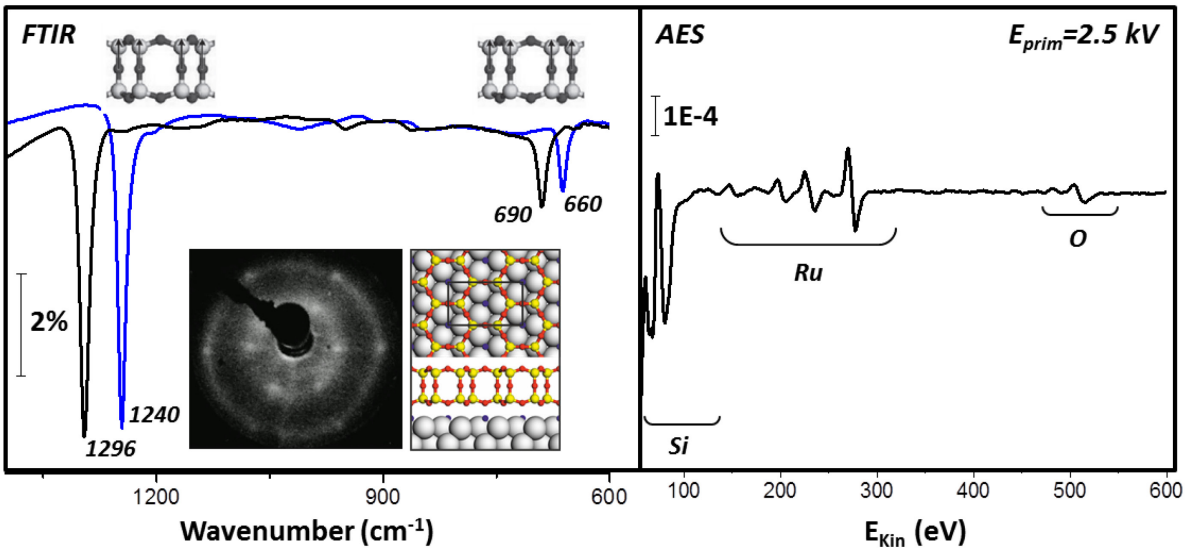

Figure 2.18: IRA spectrum and AES spectrum of the 2 MLE film. LEED pattern of the 2 MLE film and corresponding model is given next to LEED[119].

As shown above, IRAS provides the most straightforward information about determiningthe monolayer vs. bilayer structure of the silicate films.

3. Water Adsorption on Silicate Films

Due to the large abundances on earth, the interaction between water and silica surfaces is of fundamental interest in a vast variety of applications in geology, material science, microelectronics, and catalysis. In silica as a semiconductor, water can move through the gate oxide by leading to drifts in performance of transistors under bias and impairing electron reliability which is called as gate oxide integrity [122, 123]. Moreover, in microelectronics, in order to produce a buried oxide, the wafer-bonding technique is used. The technique includes cohering a hydrophilic Si wafer pair together via hydrogen bonds of the silanol groups (≡Si-OH) on both surfaces. Upon increasing temperature, siloxane bridges (≡Si-O-Si≡) are formed between two surfaces by dehydration of the silanol groups [124]. Therefore, in these applications, it is important to understand the regulations of how water affects the properties of silica surfaces. Water-silica interaction also plays an important role in natural processes such as weathering and dissolution. Additionally, it is generally accepted that the performance of silica in catalysis, where it may be utilized as either the support or the active surface, is primarily determined by surface hydroxyl species.

In the 1930s, studies carried out by Hofmann [125], Rideal [126] and Kiselev [127] indicated for the first time that hydroxyl (silanol) groups (≡Si-OH), should be existed on the surface of silicates and silicas as a result of the condensation processes of silicic acids. Kiselev later suggested that the water evolved during calcination of silica gels is formed from not only physically adsorbed water but also from OH groups that are chemically held on the silica surface [15]. By using an infrared spectroscopy method, Yaroslavsky and Terenin [128], showed for the first time the existence of hydroxyl groups on the silica surface. Since that time, great number of both experimental and theoretical studies has been performed to better understand how water interacts with amorphous silica and quartz. Nuclear magnetic resonance, infrared (IR), and Raman spectroscopies are the analytical tools that have been utilized to investigate hydroxyl species on silica. As a result of these studies, surface OH groups are subdivided into three categories: (i) isolated silanols (single silanols, ≡Si-OH) (ii) germinal free (germinal silanols or silanediols), $=Si(OH)_2$ (iii) vicinal, or bridged, or OH groups bound through the hydrogen bond which may, in principle, be differentiated by IR spectroscopy [129-133].

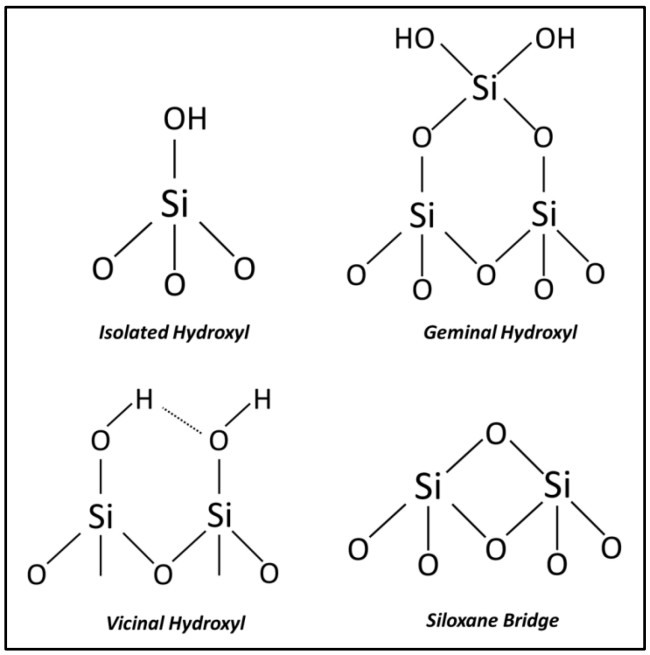

The key reaction which dominates many geochemical processes is the hydrolysis of Si-O-Si siloxane linkage, as such bond often present on the bare SiO_2 surfaces. The hydrolysis reaction of this siloxane bridge in the absence of defects has been investigated extensively [124, 134, 135], and the results reveal that there is a high activation barrier for the hydrolysis, in which water molecules do not seem to adsorb on the regular, essentially hydrophobic siloxane (Si-O-Si) terminated surface. Consequently, theoretical investigation of the hydration mechanism of the (0001) α-quartz surface showed that, the cleaved surface with non-bridging oxygen atoms at the top has been found to be very hydrophilic, however, the hydration of the dense surface shows hydrophobic character of the siloxane bonds [124]. Chemical reactivity is effectively increased by the bond angle deformations where stress-induced compressing of the Si-O-Si bond angle can form chemically active site [122]. Zhu et al. investigated the mechanical stress dependence of water hydrolysis reaction and it is determined that the increased stress could lower the energy barrier and enhance the hydrolysis reaction [136]. This idea is further supported by IR studies, that water chemisorbs on silica by opening strained siloxane (Si-O-Si) bonds and thus forming two silanol groups [130]. Subsequent water molecules then adsorbs on the silanol-covered hydrophilic surface rather than the hydrophobic pristine siloxane surface [124]. In principle, OH sites can also act as the centers of molecular adsorption by forming hydrogen bond with the adsorbate, and most of the case they undergo donor-acceptor interaction [15]. Iler [137] and others [138, 139] have suggested that the rate limiting step in hydroxylation

involves the association of molecular water with neighboring hydroxyl groups where the growth of hydrated surface patches originate. The removal of the hydroxyl groups from the surface leads to a decrease in the adsorption, and the surface becomes more hydrophobic [15]. It is also found that the extra water molecules can act as catalysts which could largely reduce the activation energy of the hydrolysis due to water stabilizing the transition states through hydrogen bonding and participating in hydrogen transfer [140-142]. H-D exchange via reaction with deuterated water is one of the chemical strategies that have been used to characterize silica, for example, to distinguish hydroxyl groups on the surface from those buried in the bulk of silica gel particles [143].

As a consequence of the structural complexity and diversity of silica, chemical properties of hydroxylated silica surfaces remain the subject of many research studies. The large inconsistencies between various silica surface studies has been caused by the different preparation methods [144][145]. Application of surface sensitive experimental techniques to silica-based materials also faces many technical obstacles due to poor electrical and thermal conductivity of these materials. These issues may, in principle, be solved by using thin silica films supported on metal substrates, which do not charge upon electrical impact or emission and efficiently cool down to liquid nitrogen temperatures. Well-defined planar samples have been extensively studied over the past decade as suitable model systems of silica [9]. Through this approach, silica structures have been prepared in the form of a "monolayer" film with $SiO_{2.5}$ compositional stoichiometry [79], or a SiO_2 bilayer [87], with both consisting of a two-dimensional, honeycomb-like network corner-sharing [SiO_4] tetrahedra. Amorphous silica overlayers thermally grown on Si surfaces behave virtually identical to thicker films of the model system.

Previous TPD, IRAS , and PES studies conducted over monolayer $SiO_{2.5}$ films on Mo(112) [146, 147] revealed that the adsorption of water is governed by weak, nondissociative interaction with the surface. Adsorption of water at 100 K resulted in zero-order desorption kinetics, however, adsorption at 140 K, water exhibited pseudo-first order kinetics, which were assigned to the formation of amorphous and crystalline water at these temperatures respectively. Absence of silanols was explained by the stabilization of surface structure due to the strong Si-O-Mo linkages present in that case. On the other hand, the ruthenium supported bilayer film is only weakly bound to the

metal substrate, and, with this respect, resembles sheet-like silicates, albeit only one unit-cell thick versions (see inset Figure 3.1). Furthermore, the bilayer films display more structural flexibility than the monolayer versions, since it may exist in crystalline or vitreous forms, and in many cases both coexisting [119].

In this work, the results of a study aimed at investigating water adsorption on bilayer silica films under vacuum conditions using infrared reflection-absorption spectroscopy (IRAS) and temperature-programmed desorption (TPD) were presented. Specifically, we concentrate on the acidic properties of hydroxyl species via the adsorption of CO and NH_3 probe molecules. The results are compared to those reported in the literature for powdered silica materials.

3.1 Results and Discussion

3.1.1 Hydroxylation of Silicate Film

Before adsorbing water, the characterization of "as-prepared' films were done by IRAS, which revealed only two sharp and intense bands at 1300 and 692 cm^{-1}. These characteristic bands represent well-defined bilayer structure, which has been discussed in detail elsewhere [9]. LEED studies revealed a (2x2)-Ru(0001) pattern conjunction with a (2x2) diffraction ring, indicating that both crystalline and vitreous silicate domains coexist in the films. The presence of "holes" were estimated by CO adsorption studies and previous TPD/STM results, which resulted in <5% of the underlying O-covered Ru(0001) support.

IRAS studies revealed no detectable hydroxo species as a result of the adsorption of water onto the silicate films at 300 K (We especially used deuterated water (D_2O) to discriminate against reactions that can happen with residual water in the vacuum background.). This finding can be readily explained by the atomic structure of the silicate bilayer film, which is terminated by an O-layer from strong siloxane bridges, and is, therefore, hydrophobic. The sticking coefficient was increased, by adsorbing water at low temperatures (~100 K) which resulted in an "amorphous solid water" film (or ice, for simplicity). The sublimation of ice overlayer occurred at ≅ 160 K (Figure 3.1a) following zero-order kinetics (additional spectra are not shown here), subsequently hydroxo species become obviously apparent in IRAS (Figure 3.1b). It

should be noted that no OD species were detected after the same treatment over the 3O (2 x 2)-Ru(0001) surface during control experiments.

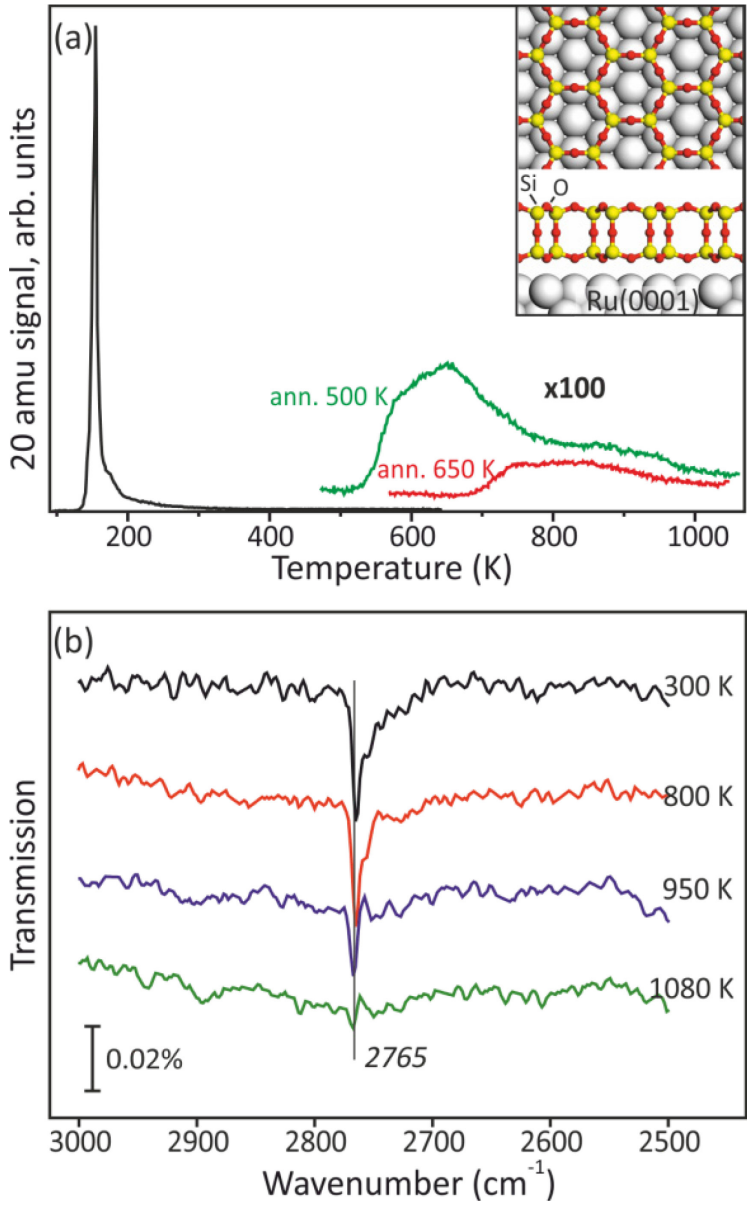

Figure 3.1: (a) TPD spectra (20 amu) of 5 L of D_2O adsorbed onto a bilayer silica film at 100 K and subsequently heated at a rate of 3 K/s. The green curve shows a typical spectrum for a sample preheated to 600 K to diminish the shadowing effect of the tail from multilayer water desorption. The red curve shows the spectrum of a sample preheated to 750 K. Both spectra reveal a desorption feature centered at 900 K. (b) IRA spectra of a film exposed to D_2O at 100 K and heated to the indicated temperature. The spectra were taken at 100 K and are offset for clarity. The inset in (a) depicts the atomic structure of the bilayer film grown on Ru(0001).

The black spectrum in Figure 3.1b, which was obtained after heating to 300 K, displays a sharp signal centered at 2765 cm^{-1}. This feature can be straightforwardly assigned to

ν(O-D) stretching vibrations and readily shifts to 3750 cm^{-1} via D-H exchange upon exposure to H_2O at low temperatures. Moreover, the presence of a prominent shoulder on the low frequency side of the main peak, which extends to 2700 cm^{-1}, was also recorded. Correspondingly, [123] hydrogen-bonded OD species are responsible for this but it should be noted considered an upper limit for the nearest-neighbor hydroxyl concentration due to possible contributions from small amounts of water readsorption prior to performing our measurements at 100 K. The shoulder disappears upon heating to elevated temperatures, and subsequently, the main peak centered at 2765 cm^{-1} gradually attenuates (Figure 3.1b). It appears that, D-bonded species desorb first, presumably due to a higher probability for the recombination of adjacent hydroxyls. The full desorption of the remaining silanols takes place at ~1100 K, which indicates their high thermal stability. However, it should be noted that powdered silica samples typically require temperatures well above 1200 K for full dehydroxylation [148], most likely due to the diffusion limitations in these materials.

Agreeing well with the IRAS data, the recombinative desorption of hydroxyls in the form of water at high temperatures was also detected by TPD. A long desorption tail extending around 200 K is usually observed in TPD spectra of ice films and is commonly attributed to the low pumping rate of water. In order to reduce this effect, the sample was preheated to 600 K in the first TPD run (green curve in Figure 3.1a) and to 750 K in the second adsorption-desorption run (red curve in Figure 3.1a). A feature beginning at ~800 K is visible in both desorption curves, which is roughly consistent with the onset for disappearance of the principal IRA signal at 2765 cm^{-1} (Figure 3.1b). By the observation of the changes in the relative intensity of the lower temperature feature with variation in the duration of ~300 K annealing and the subsequent TPD heating rates, we have concluded that only the higher temperature feature relates to water evolution from the surface (i.e. lower temperature desorption in the range below T ≈ 800 K arises from background sources unrelated to the reactions occurring on the silica.) From the integral intensity of the TPD signal observed for recombinative water from various samples, we calculated an upper limit of ~0.1 nm^{-2} for the surface density of silanols, which is roughly equivalent to one OH per every 40 six-membered rings (under the assumption of a perfectly ordered honeycomb-like structure). Therefore, we conclude that the defect sites are responsible for the hydroxylation rather than regular sites.

In the literature, it is generally accepted that the hydroxylation of silica and silicalites proceeds via "opening" of asymmetrically strained siloxane bridge sites [148] or edge-shared tetrahedral dimers [130], as shown schematically below:

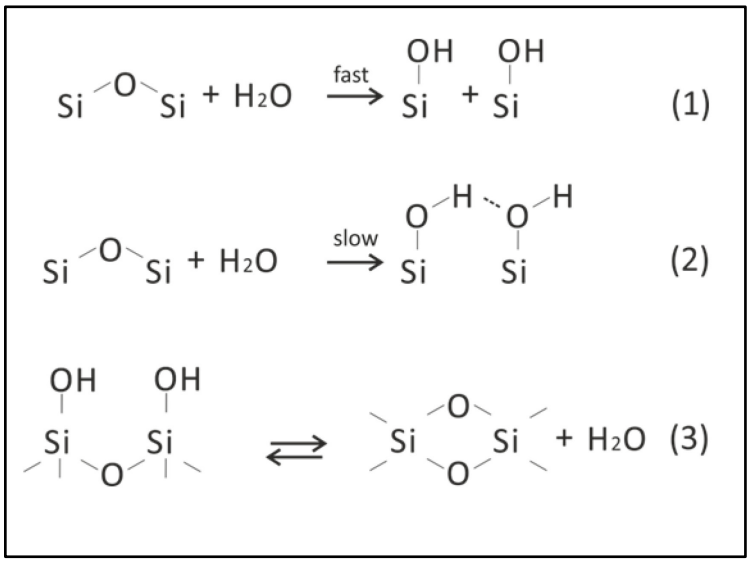

This interpretation comes primarily from the inverse relationship between the intensities of bands in the 890-910 cm^{-1} region (assigned to strained siloxanes) and the ν(OH) band at 3748 cm^{-1}. The large majority of the studies on this field have been performed on high surface are silica samples prepared by "wet chemistry-sol-gel methods", for which it has been generally concluded that strained siloxanes are formed by the recombination of surface silanols at elevated temperatures following route 3. On the other hand, IRAS studies of thin silica films by Chiang et al. [149] revealed that such defects can be formed on dry silica upon annealing to 1400 K. (In this experiment, the film preparation was done by decomposition of a native silica film on a Si wafer, which was positioned in front of a polycrystalline Mo block in vacuo). The results of the latter study also indicated that the local structure determines the chemistry of silica rather than the global surface area.

Our IRAS experiments did not reveal any features around 800-900 cm^{-1} region which can be correlated with the degree of hydroxylation. Definitely, this can be related with the low detection efficiency of these bands, which are not so easy to detect even on the powdered systems [149]. By inspecting mechanism 1 or 2, nevertheless, one of two hydroxyl species should include an oxygen atom from the silica lattice and the other oxygen atom from a dissociated water molecule. Therefore, isotopic labeling of the oxygen in silica and water can help in order to study the reaction mechanism and verify

the proposed scenario. Morrow et al.[123] have previously reported isotopic experiments with $H_2{}^{18}O$, however, considerable amount of residual ^{16}OH species were present in the silica sample prior to the $H_2{}^{18}O$ adsorption. Nonetheless, the secondary reaction 2, which was thought to occur on sites other than those involved in reaction 1, was justified by using these results. Later, Bunker et al. [130] suggested the presence of two types of defects (silanol-free and silanol-containing edge shared defects), with saying that silanol-free defect types are much more reactive. In order to investigate the hydroxylation mechanism in more detail for our films, we have performed isotopic experiments which can be easily carried out on the model system introduced here under well-controlled conditions.

Figure 3.2a displays a typical phonon spectrum from a silica film prepared with ^{18}O, where the main bands are shifted by predictable amounts to lower frequencies (1247 and 644 cm^{-1}, respectively) when compared to $Si^{16}O_2$ phonon.

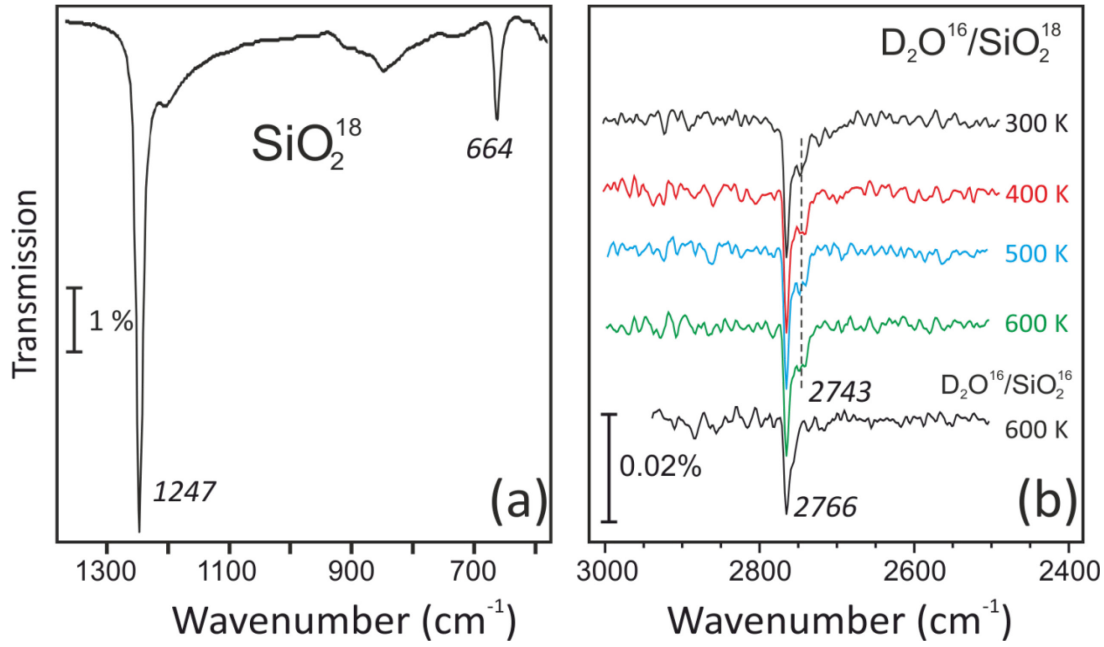

Figure 3.2: (a) IRA spectrum of a silica bilayer film prepared with ^{18}O. (b) IRA spectra of the ν(OD) region following adsorption of D_2O^{16} on this film and heating to the indicated temperature. The spectra are offset for clarity.

After the preparation of this film, the surface was hydroxylated with $D_2{}^{16}O$, and the IRA spectra shown in Figure 3.2b were taken. Surprisingly, the IRA spectrum taken at 300 K of the $Si^{18}O_2$ film, treated with $D_2{}^{16}O$ at 100 K and heated to 300 K, is virtually identical to the hydroxylated film prepared with ^{16}O (compare Figure 3.1b and Figure

3.2b). In the meantime, due to the hydrogen-bonded ^{16}OD shoulder noted for the unlabeled film, the signal from ^{18}OD species, expected at around 2750 cm^{-1} on the basis of reduced mass analysis, is hardly distinguishable. Upon heating the film up to 600 K, we can unambiguously start seeing the presence of some ^{18}OD, albeit with far less signal intensity than that for the ^{16}OD feature.

In principle, these findings can be explained in different ways: (i) the hydroxylation of ultrathin silica films produced in UHV conditions proceeds by way of a mechanism other than that commonly considered for three dimensional amorphous silica and silicalites; (ii) the ^{18}O-D bond is almost parallel to the surface and, as such, becomes nearly invisible in IRAS due to the so-called 'surface selection rule', which implies that only vibrational modes that give rise to an oscillating dipole normal to the metallic surface are active [92], (iii) the geminal silanols were created as a result of hydroxylation i.e. with ^{18}OD and ^{16}OD attached to the same Si atoms, and the low frequency band associated with ^{18}OD is suppressed due to the so-called "intensity borrowing," [92], where a higher frequency signal dominates the spectrum of a system consisting of strongly coupled oscillators; [150] (iv) any combination of (i)-(iii). It should be noted that if the hydroxylation occurs on adventitious silica clusters and particles rather than on the silica film, then one would expect equal intensities of the two OD bands due to the random orientation of surface species on these particles with respect to the film normal.

The results shown in Figure 3.2 were further assisted by isotope-exchange recombinative water TPD studies from Si^{18}O$_2$ samples following low-temperature exposure to D$_2$^{16}O and subsequent annealing above room temperature. The results plotted in Figure 3.3a revealed the detection of mostly m/z$^+$ =18, 19, and 20 upon recombinative desorption of the dissociated water species. This is also displayed in Figure 3.3b, which plots the relative intensity of the time-dependent peak integrals for each of the mass channels collected in Figure 3.3a during both multilayer (T_{desorb} ≈160 K) and recombinative (T_{desorb} ≈940 K) water desorption.

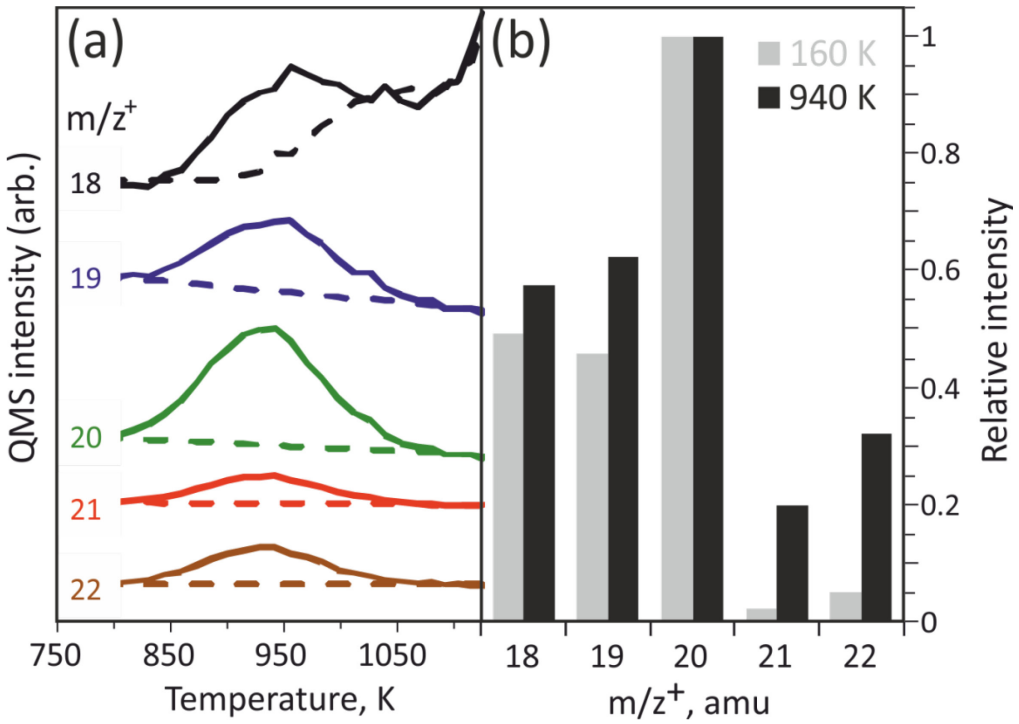

Figure 3.3: (a) TPD spectra (the heating rate 10 K/s) are shown as a function of constituent mass for the recombinative desorption of water from bilayer $Si^{18}O_2$/Ru(0001) following exposure to 5 L of $D_2{}^{16}O$ at ~130 K and subsequent heating to 300 K. The dashed lines indicate the backgrounds used for peak integration and are linear in all cases except $m/z^+ = 18$, where the background has been obtained by appropriately scaling the $m/z^+ = 36$ desorption profile to account for $^{18}O_2$ cracking contributions during the onset of ^{18}O/Ru recombinative desorption. (b) The relative intensity of the time-integrated TPD signals for various mass channels during the desorption of multilayer ($T_{peak} \approx 160$ K) and recombinative ($T_{peak} \approx 940$ K) water are compared using the experimental data from (a). (Provided by Dr. Kaden)

Investigation of this data shows that the lower mass-channel domination of the distributions reflects desorption of predominantly ^{16}O species. A significant concentration of H impurities within the D_2O dose is displayed by the large relative intensities for $m/z^+ = 18$ and 19, but this manifests itself to a similar degree in both desorption features. On the other hand, although the significant abundance of $m/z^+ = 21$ and 22 are detected in the high-temperature feature, these species are mostly absent during multilayer desorption and implies some degree of surface scrambling, such that ~25% of the recombinatively desorbing water incorporates an ^{18}O from the surface prior to departing. The relative abundance of ^{18}OD detected at lower temperatures via IRAS (Figure 3.2b) roughly proves this finding which is far less than would be recombination of freely diffusing D species meeting over randomly positioned O atoms. This result reveals that desorption of water seems to occur nearly exclusively from the defect sites

where the dissociative binding of the hydroxyls occurred, which supplies more evidence that these sites are likely different in nature from those in the majority of the film.

A commonly observed defect type in studies of epitaxially grown, thin film oxides is domain boundaries. In silicate bilayer films, the crystalline phase smoothly transforms into the vitreous phase which were shown by previous high-resolution STM studies, and no other defects, in terms of unsaturated bonds or different bonding arrangements, were found [119, 151]. Despite this, local variations of corrugation amplitude (typically, <0.2 Å) can sometimes be found in both the amorphous and crystalline areas and this can be associated with variations of the local density of states (probed by STM), e.g., by formation of strained Si-O-Si siloxane bridges. However, the very large dominance of only one type of OD species in the isotopic experiments cannot be explained by those structures, which are parallel to the film surface, provided hydroxylation goes through route 1. As another option, the reaction could take place via water-induced breaking of the Si-O-Si linkage between the two layers (see the structure in the inset of Figure 3.1a) due to vertical distortion of the upper Si out of the surface plane upon dissociative binding of ^{16}OD. However, IRAS results [119] indicated that the vertical Si-O-Si linkage is the least suffering from the disordering of the lateral film and, therefore, more stable than the surface Si-O-Si species. Moreover, hydroxylation occurs at temperatures as low as 200 K, thus implying that the reaction has almost no activation barrier, which is hardly feasible on the vertical Si-O-Si linkages, albeit with a high density of water molecules provided by the ice film. Additionally, what happens to the second "invisible" D atom (ion) remains unclear.

Also, we might additionally consider step edges as an alternative type of "defect", which are commonly thought to expose low-coordinated surface atoms and might, thereby, act as active sites for water adsorption. These sites can be formed either on a step between two silica terraces, which basically follow the topography of the underlying metal support, or along the border of "holes", which are also present in the films. In the absence of any reconstruction, very reactive dangling Si-O bonds, which can then be stabilized by hydroxyls in the same manner as cleaved quartz surfaces, must be exposed by such step edges. The high reactivity of such sites could provide an explanation for the frequent observations of small amounts of hydroxyls on the "as-prepared" films, which can seemingly be formed through reaction with residual gases in

the vacuum background. Unfortunately, STM was unsuccessful to visualize hydroxyls for the bilayer film, but it was achievable on monolayer films.

STM image of a monolayer silica film is shown in Figure 3.4b, which was intentionally created with an abundance of Ru-exposing holes and then hydroxylated in the same manner consistent with that already discussed for the bilayer films. The protrusions that are atomically sized bout 1-2 Å in height, decorate the holes, and appear only upon hydroxylation and go along with the appearance of the band at 2760 cm^{-1} in IRAS, as also shown in Figure 3.4a.The protrusions are assigned to surface hydroxyls on the basis of this correlation. The shortest distance between these protrusions is about 5 Å, i.e., the length of the unit cell in the silicate film, implying that these species are isolated in nature, in agreement with the IRAS results. The interpretation of the preferential binding along the perimeter of the hole suggests that step edges likely provide the majority of the active sites for water dissociation and binding, while the TPD results indicate either a limitation to diffusion confined within those regions or, at a minimum, a lower activation barrier for desorption from them. We should also note that the ν(OH) band for monolayer films (2760 cm^{-1}) is slightly (by 5 cm^{-1}) red-shifted with respect to that for bilayer films, demonstrating some effect from the chemical bonds between the silicate and the metal support.

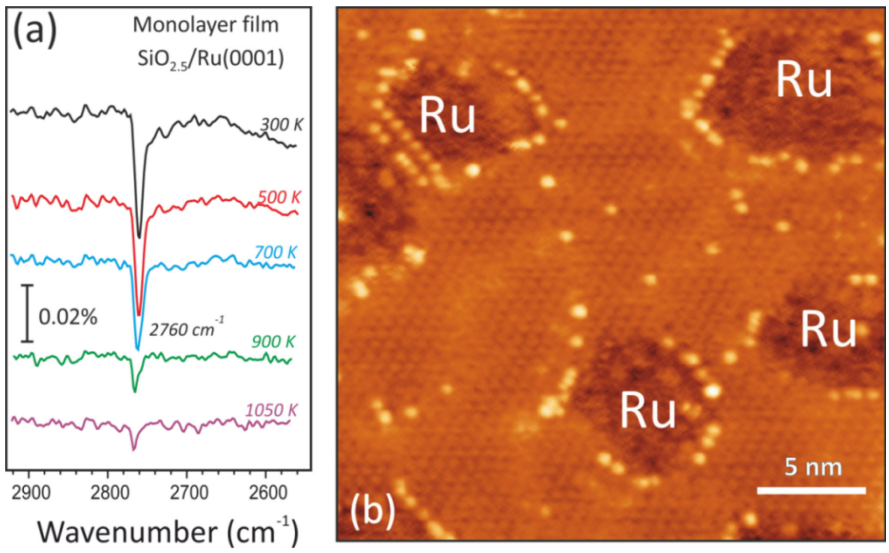

Figure 3.4: The ν(OD) region of IRA-spectra (a) and a room temperature STM image (Provided by Dr. B. Yang) (b) of a hydroxylated monolayer $SiO_{2.5}$ film on Ru(0001). The spectra are measured after D_2O adsorption at 100 K and heating to the indicated temperature. The spectra are offset for clarity. The sample, imaged in (b), intentionally contained many "holes" exposing a metal substrate to demonstrate a decoration of step edges by hydroxo species.

3.1.2 CO and NH_3 Adsorption on Hydroxylated Silicate Film

In order to study the acidic properties of hydroxyl species on oxides, the adsorption of CO and NH_3 is generally used, as weak and strong bases respectively. When OH-CO adduct is formed by CO, spectral shifts can be recorded for both O-H and C=O stretching vibrations, and the magnitude of this shift is an indication of proton acidity [152]. A proton may even be removed in the case of strong bases.

Prior to CO and NH_3 adsorption, the hydroxylated films were prepared by water adsorption at 100 K and heating to 300 K in UHV. No change in the position or integral intensity of the ν(OD) band at 2765 cm^{-1} was observed as a result of continuous exposure of hydroxylated silica films to ~10^{-5} mbar CO at 300 K (Figure 3.5). Additionally, the only change we note is the appearance of a signal at ~2050 cm^{-1} that quickly saturates with increasing CO exposure. This band can be due to atop CO species binding over Ru in areas exposed by "holes" or large pores within amorphous domains of the silica film [119]. Therefore, CO does not interact with silanols, which differs from results obtained over Al-doped silica films, where highly acidic bridging (Si-O-Al) hydroxyls are produced [153]. For comparison, ν(CO) band for the "as prepared" films is at ~2075 cm^{-1},and characteristic for the O-precovered Ru surface in the film. Therefore, red shifted value of 2050 cm^{-1} implies that the combination of water adsorption and subsequent desorption acts to remove O atoms directly adsorbed on Ru within the more porous areas of the film.

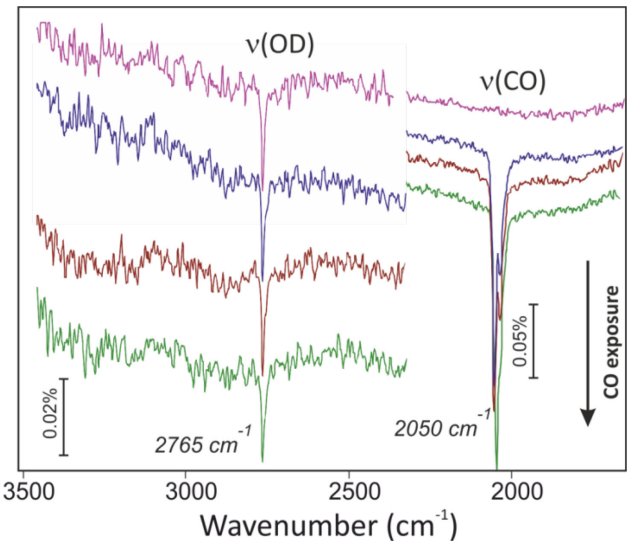

Figure 3.5: The ν(OD) and ν(CO) regions in the IRA spectra of bilayer silicate films before (a top spectrum) and during CO exposure at 300 K. The spectra are offset for clarity.

Since CO adsorption on hydroxyls show no interaction, the surface was also probed with NH_3 to determine if the stronger base might show some reactivity. Dosing at room temperature caused only subtle changes in IRAS. Contrastingly, the TPD spectra shown in Figure 3.6 do contribute some evidence about reactivity following exposure of the prehydroxylated surface to ammonia. At this point, it should be remembered that masses 17 and 16 correspond to NH_3^+ and NH_2^+ ions of NH_3 in the mass spectrometer. D_2O is associated with the 20 amu, and can contribute to the 18 and 16 amu signals as DO^+ and O^+, respectively. Additionally, the 18 amu is also principal signal from H_2O, which in turn contributes to the 17 amu (OH^+) and 16 amu (O^+) signals. Finally, the mass 19 can be assigned to HDO, which also has fragments at 18, 17, and 16 amu's, while D-substituted ammonia $NH_{3-x}D_x$ exhibits different masses depending on x.

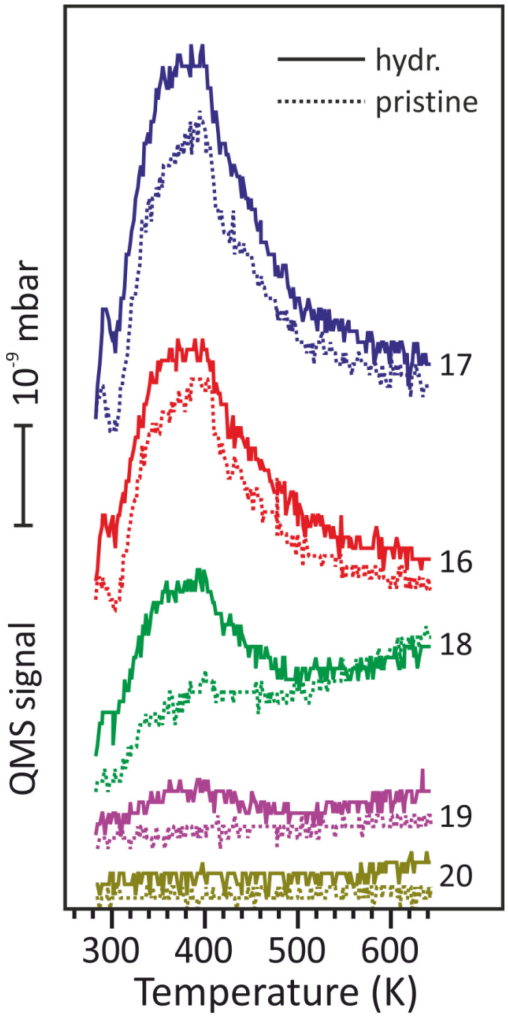

Figure 3.6: TPD signals for indicated masses after adsorption of 10 L NH_3 onto pristine (dashed lines) and OD-containing (solid lines) bilayer silicate films at 300 K. The spectra are offset for clarity.

One can detect the obvious difference between the TPD spectra from the pristine and hydroxylated surfaces (Figure 3.6) for the 18 amu signal. Definitely, the 20 amu signal which is negligible cannot contribute to this feature. In principle, OH recombination following a H-D exchange reaction between OD and NH_3 could form H_2O, however the desorption temperature (~400 K) is clearly too low for this; we, therefore, propose that the creation and desorption of NH_2D provides a more plausible explanation of this signal's origin. In such exchange reactions, the formation of NHD_2 (19 amu) and ND_3 (20 amu), should also be considered, however under our conditions of experiment, they turned out to be almost negligible.

In order to investigate the reactions that occur at low temperatures, NH_3 adsorption was performed at 100 K. Once again, TPD measurements show evidence of reaction between the NH_3 and coadsorbed hydroxyls, which demonstrates itself as a second desorption feature at 150 K (Figure 3.7a) and is not observed for ammonia TPD from pristine samples (Figure 3.7b). The mass dependent fragments of the signal in this feature shows significant intensity for every channel associated with ND_xH_y ion detection, but qualitatively, the whole distribution appears to be shifted by 1 amu to larger values relative to that from the low-temperature feature (Figure 3.7c).

By assuming that the signal at ~115 K results from molecular desorption of contaminant-free NH_3, we can conclude that H-D exchange during wall reactions within the mass spectrometer causes the relative abundance of masses 18, 19, and 20 in this feature. In conjunction with the NH_3 cracking pattern, we can then use the relative abundances of those masses to estimate the likelihood of exchanging 1, 2, or 3 hydrogen(s) for deuterium via wall reaction and, from that, predict the relative abundances of m/z^+= 16-20 that would be expected for the case when 1 H-D exchange takes place to form NDH_2 on the surface prior to desorption into the mass spectrometer. The good agreement of such a distribution with our experimental data suggests that the signal at 150 K results predominantly from desorption of NDH_2 produced in this manner. Additionally, a small desorption feature of 17 amu is also detected at ~400 K (Figure 3.7b), which is almost at the same temperature at which ammonia desorption was noted after adsorption at 300 K (Figure 3.6).

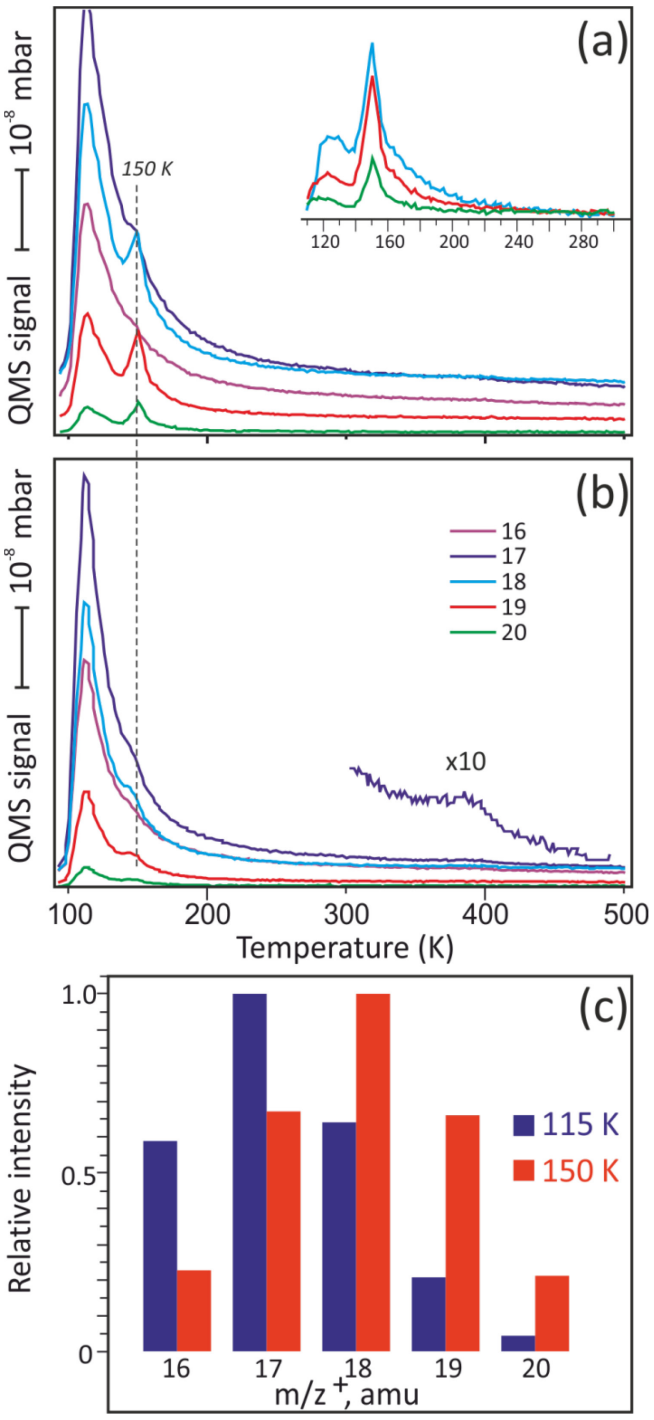

Figure 3.7: TPD signals of 10 L NH_3 adsorbed over hydroxylated (a) and pristine (b) bilayer SiO_2/Ru(0001) samples (T_{ads} = 100 K) are shown for several masses of interest. (c) The relative abundance of the various masses probed in (a) are shown for the two desorption features, i.e. at 115 and 150 K.

In order to have a better understanding of this surface chemistry, we also conducted a complementary low-temperature IRAS study. A series of spectra taken from hydroxylated silica after NH_3 adsorption at ~90 K and subsequent annealing to the indicated temperatures are shown in Figure 3.8.

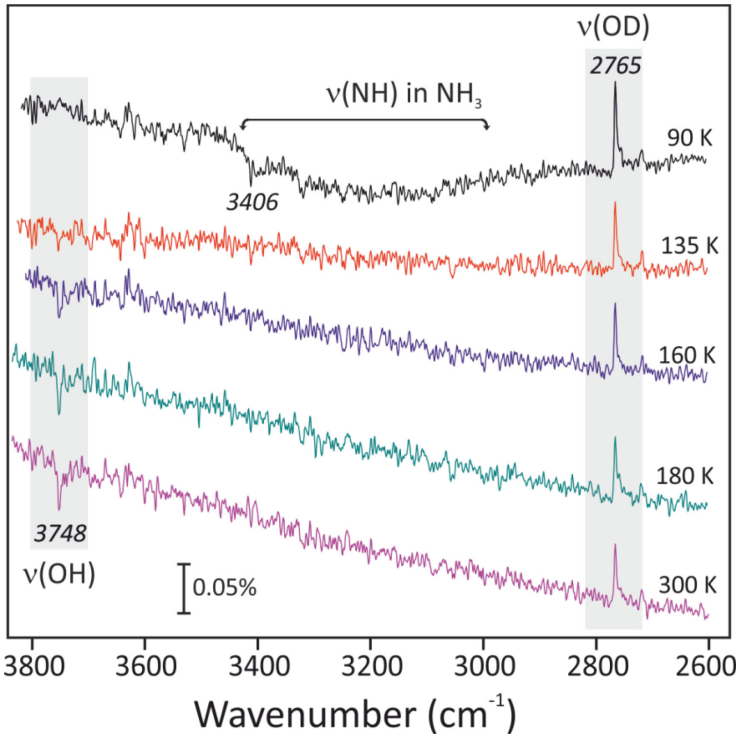

Figure 3.8: IRA spectra of an OD-containing bilayer silicate film after adsorption of NH_3 and heating to the indicated temperature. The spectra are referenced to a spectrum taken before ammonia adsorption and are offset with the ν(OD) and ν(OH) bands highlighted for clarity.

The spectral changes were recorded by dividing a reference spectrum, which was taken prior to ammonia adsorption. Molecularly adsorbed ammonia has given a peak at 3406 cm^{-1} and a broad band at 3000-3500 cm^{-1}, which is assigned to the asymmetric and symmetric N-H stretching vibrations in NH_3 (top spectrum in Figure 3.8) [154]. N-H deformation modes at 1635-1600 cm^{-1} were also observed additionally.

Arrival of the ammonia features at 90 K causes a concomitant loss of the ν(OD) band, which results in a positive signal at 2765 cm^{-1}. The ν(NH) bands vanish since the more weakly bound ammonia desorbs intact after heating to 135 K, which is below the second desorption maximum at 150 K (see Figure 3.7). Upon heating to 160 K, and further to 300 K, the intensity of the positive ν(OD) signal at 2765 cm^{-1} only changes slightly, indicating that the majority of the OD species are consumed by reaction with ammonia. In the meantime, a ν(OH) band at 3748 cm^{-1} starts appearing by 160 K and saturates by 180 K, which seems to support our TPD analysis (i.e., that H-D exchange occurs between OD and NH_3 at low temperatures to form D-substituted ammonia, which then desorbs, leaving behind OH species).

The absence of ammonia in the 150 K desorption feature, and the absence of this feature altogether from pristine films can be due to (i) ammonia is more strongly bound to surface hydroxyls, and (ii) the high conversion of the exchange reaction suggest that no hydroxyl-bound NH_3 survives, and almost all ODs transform into OHs, asFigure 3.8 suggests. So that, the peak desorption temperature (149 K) can be used to estimate an upper limit to the activation barrier for the H-D reaction, which is calculated to be ~37 kj/mol using a Redhead formalism [107] with a prefactor $\nu_0 = 10^{13}$ s^{-1} corresponding to OH (OD) vibrations.

To understand whether the exact nature of the silanol groups (isolated vs H-bonded) is especially important in enabling the H-D reaction with ammonia, the production of NH_2D (at 140-180 K) is measured as a function of the annealing temperature of OD-containing films before NH_3 adsorption (Figure 3.9). In this case, the measurements were performed sequentially over the same film, which was regenerated via high temperature oxidation and subsequent D_2O hydroxylation before each heating step (300, 600, and 900 K). The IRA spectra of the samples are depicted in the inset in Figure 3.9 respectively.

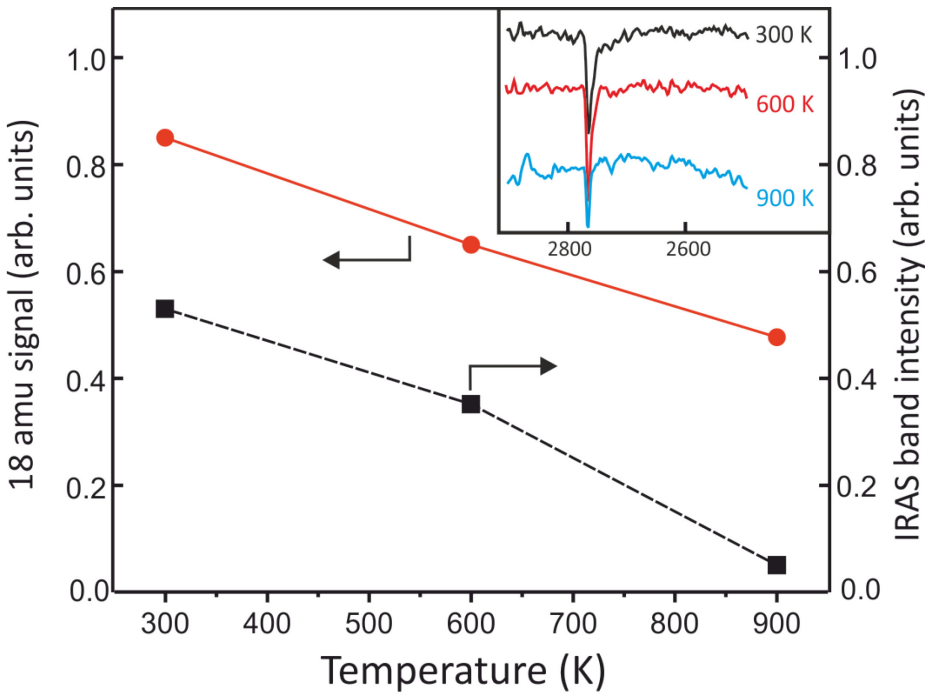

Figure 3.9: Integral intensities of the 18 amu signal at 140 – 180 K (see Figure3.7) and of the IRAS peak at 2765 cm^{-1} (see inset) as a function of the annealing temperature of an OD-containing bilayer silicate film.

As previously mentioned, isolated silanols are formed as a result of high-temperature annealing, whereas annealing to 300 K seems to result in H-bonded species as well. Since, it appears that there is a linear relationship between the H-D exchange reaction and the total number of OD groups, with no significant deviation when H-bonded species are present; we conclude that the coadsorbed ammonia interacts dependently with each hydroxyl during the H-D exchange reaction.

Finally, the adsorption of ammonia over O^{18}-prepared silica, which also revealed some interesting results, was studied. The top spectrum in Figure 3.10 displays a spectrum from a $Si^{18}O_2$ film that was exposed to $D_2{}^{16}O$ at 100 K and then heated to 300 K.

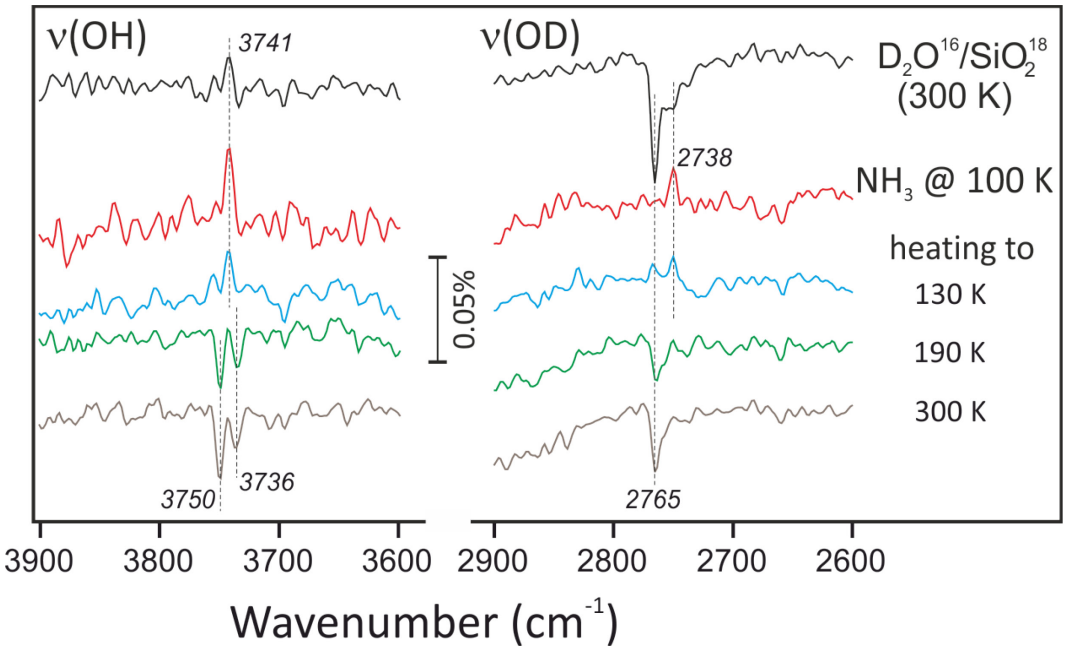

Figure 3.10: (Top) IRA spectrum of a $Si^{18}O_2$ film exposed to $D_2{}^{16}O$ at 100 K and heated to 300 K (top), which was then exposed to NH_3 at 100 K and heated to the indicated temperatures. All spectra are referenced to a spectrum from the "as-prepared" film taken before D_2O^{16} adsorption, and are offset for clarity.

Once again, the data are plotted top reference spectrum, which in this case, was taken from the "as-prepared" film before hydroxylation in this case. As in the case of unlabeled SiO_2 (Figure 3.2), the peak at 2765 cm^{-1} (i.e., ^{16}OD) dominates again the OD region following hydroxylation of the ^{18}O-substituted film. Close inspection of the ν(OH) region, however, reveals a tiny positive signal at 3741 cm^{-1} (black spectrum in

Figure 3.10), which is assigned to traces of ^{18}OH in the reference $Si^{18}O_2$ sample. Even though, there is a possibly that these ^{18}OH species may undergo H-D exchange upon hydroxylation with $D_2{}^{16}O$, the additional contribution to ^{18}OD-related IRA signals is obviously small.

It is apparent that ν(OD) band is suppressed by NH_3 adsorption at 100 K (second spectrum from the top in Figure 3.10). However, simultaneously, a new positive signal is detected at 2738 cm^{-1} for ^{18}OD, and the positive signal at 3741 cm^{-1} (^{18}OH) even becomes more intense. This reveals the presence of adventitious ^{18}OD and ^{18}OH species in the reference sample, which are most likely formed by the reaction of highly hydrophobic Si-O dangling bonds with residual gases in the vacuum background (i.e., After several experiments, H_2O and D_2O level are increased in the background). Furthermore, this result indicates that NH_3 adsorption at low-temperature (100 K) effectively titrates all hydroxyl species in the sample, regardless of their origin.

Upon heating to higher temperatures, the partial recovery of the ν(^{16}OD) band at 2765 cm^{-1} and the appearance of a ν(^{16}OH) band at 3750 cm^{-1}, which comes from H-D exchange reaction, was observed after thermal desorption of ammonia (bottom spectrum in Figure 3.10). Comparing the top (before reaction with NH_3) and the bottom (after reaction with NH_3), it is observed that the intensity of the resultant ν(^{16}OH) feature is nearly equal to the attenuation of the ν(^{16}OD) band. The absence of a well-resolved peak corresponding to ^{18}OD after hydroxylation (top spectrum) makes the interpretation of the ^{18}O-labeled counterpart harder. Despite this, the fact that the ν(^{18}OH) signal at 3736 cm^{-1} in the bottom spectrum approximately equals the positive signal from ν(^{18}OD) at 2738 cm^{-1} in the second spectrum suggests that the most of the new ^{18}OHs originated via H-D exchange of ^{18}ODs that were already present before $D_2{}^{16}O$ adsorption. The data are agreeing well with our earlier analysis, which indicates that the incorporation of lattice oxygen into hydroxyls hardly exists and reveals that the H-D exchange reaction occurs on each OH site, independent of origin. Furthermore, our previous doubt postulated from “energy borrowing” and metal selection rule explanations of the IRAS data in Figure 3.2 is also elucidated by the observation of two well-resolved peaks in the OH region, for both ^{18}O- and ^{16}O-labeled species. Therefore, it seems that exposure to water results in hydroxylation via OH-Si bond formation, additionally, leaves excess H atoms on the surface. These excess hydrogen can be removed by recombinative desorption and/or capture by the metal support. It is noteworthy to mention that the

same behavior with respect to the H-D reaction with ammonia was also observed with monolayer films, in which desorption peak of ammonia was at slightly higher temperature (~160 K) compared to bilayer films (~150 K).

3.2 Conclusions

In this study, we examined the formation and adsorption properties of hydroxyl species on silicate film grown on Ru(0001). It is found that hydroxylation occurs at defects most likely step edges at temperatures as low as ~180 K. Water dissociation seems to be more facile in the presence of several water molecules, since hydroxylation is observed only after water film formation at low temperatures and subsequent heating in order to desorb unreacted water molecules. Water dissociation yields surface Si-OH species and another hydrogen atom that may produce the second OH including oxygen in silicate. This hydrogen may also leave the surface via desorption with water. In addition, it may reach the Ru(0001) surface and recombinatively desorb. Apparently, the precise mechanism depends on the conditions applied. In addition, the IRAS results may be affected by the metal selection rule. Therefore, theoretical calculations are necessary to rationalize the IRAS results observed here. Nonetheless, recombinative desorption of OH through water appears to occur almost exclusively from the sites where dissociation first occurred, such that the desorbing water molecule contains very little lattice oxygen.

The chemical properties of the silanols which were investigated by using CO, water, and NH_3 revealed no evidence for acidity of silanols, however, upon adsorption of NH_3, H-D exchange is observed, where OH species can be replaced by OD and vice versa. This finding strongly suggests that the reaction between hydroxyls and ammonia likely proceeds via the same mechanism as that between OD(OH) and $H_2O(D_2O)$. The adsorption of NH_3 on OD is stronger that with the regular silicate surface. Desorbing ammonia complexes after the interaction with hydroxyls were almost exclusively in the form of NDH_2, in which the ammonia desorption energy of ~37 kj/mol was calculated as an upper limit approximation of the H-D exchange activation barrier.

4. Interaction of "Simple" Molecules with Silicate Films: Adsorption vs. Intercalation

It has been previously observed that the "as prepared" bilayer silicate sheet weakly bound to the Ru (0001) substrate contain oxygen atoms adsorbed directly onto the metal support [87, 88, 155]. Evidenced by XPS studies as a function of annealing temperature, Si2p and O1s(Si) levels shifts equally, and also their intensities remain constant upon annealing to 1150 K. Therefore, it has been concluded that annealing to 1150 K doesn't change the chemical composition and stoichiometry of the silicate film. However, although the O1s(Ru)-related peak doesn't shift, its intensity decreases upon UHV annealing to 1150 K by almost a factor of two, and comes back after sample reoxidation in $2x10^{-6}$ mbar of O_2 at 1140 K [88].It appears that the O coverage can be altered without structural changes of the silicate itself and the molecular oxygen may adsorb/desorb on/from the metal surface underneath the silicate layer. Theoretical calculations demonstrated that the silica/Ru electronic states can also be tuned depending on the O coverage which can open the avenue for tuning the electronic properties of oxide/metal systems without altering the thickness or the structure of an oxide layer. Accordingly, the interlayer space between the silicate sheet and the metal surface (which is computed to be in the range of 2.5 – 3 Å [88]) could be sufficient for surface diffusion of small adsorbed species and subsequent chemical reactions on the metal surface. It is therefore intriguing to utilize the silicate overlayer, which is essentially inert, as a molecular sieve for reactions that may otherwise occur unselectively on the supporting metal surface.

The single-layer silicate, supported on Mo(112), has previously been examined both experimentally and theoretically with respect to the permeation of metal (Au, Pd) atoms only [156, 157]. The adsorption of the same metal atoms on the bilayer silicate was also investigated by the same group as well [158]. The results reveal that Pd atoms penetrate through the silicate and reach the metal support surface essentially without any barrier, while the penetration of Au adatoms depends considerably on the ring size.

In general, diffusion of gases in confined systems remains an interesting issue, in particular about whether a Knudsen description holds true when the pore size approaches the nanometer scale [159-163]. In this context, it is worth mentioning that a

defect-free graphene membrane was found to be impermeable to standard gases, including helium [164]. However, theoretical calculations predicted extremely high selectivity to separate H_2 and CH_4 for graphene possessing defects as pores [165]. Graphene which is prepared on single crystals can also be used in order to study surface chemistry in confined space. As a planar material, it has a distance typically 1 nm between metal substrate, and therefore, adsorbates such as CO, O_2 and H_2O can be readily intercalated under the graphene overlayers [166-170]. The principal structure of single-layer silicate is essentially similar to that of graphene that would allow us to look into the properties of such truly two-dimensional systems solely on topology grounds [171].

Here, the permeation of the silicate with respect to simple gases, such as CO and D_2 is examined. Since it is still not possible to fabricate silicate as a free-standing sheet, the standard methods and techniques for mass transport studies cannot be applied. In attempts to elucidate the permeability of the silicate, we employ here a metal support (in this case Ru(0001)) as a gas detector, bearing in mind that the adsorption and coadsorption of O_2, CO, and H_2 on Ru(0001) is well-documented in the literature [172-184]. The results uncover a complex behavior which involves gas transport through the pores and diffusion across the metal surface underneath the silicate which may aid in our understanding of the reactivity of such hybrid systems combining a molecular-sieve membrane and a chemically active metal underneath.

4.1 Results

First, the integrity of the silicate samples is examined in order to understand whether they possess some macroscopic “holes” which will certainly mislead the results on true gas permeation through the silicate film. For this purpose, CO was used as a probe molecule since its interaction with the Ru surfaces, studied by both IRAS and TPD, is well documented in the literature. For quantitative analysis, we used a “Si-free” sample as a reference which is prepared under the same conditions as the silicate sample, excluding only the Si deposition step. Since CO chemisorbs on the clean and O/Ru surfaces with a high sticking coefficient at low temperatures, the “as prepared” silicate samples were exposed to low CO pressures (ca. 10^{-9} mbar) at 150 K. The simultaneously recorded IRA-spectra revealed only a tiny peak at 2053 cm^{-1} (not shown

here). The TPD spectrum from this sample is presented in Figure 4.1a(red spectra) to compare with the spectra obtained on the clean Ru(0001) and Si-free samples. It is obvious that the CO desorption profile from the silicate sample resembles the one of the Si-free sample which is, in turn, very similar to those observed for CO on O-covered Ru(0001) surfaces [183, 185]. The integral signal ratios demonstrate that the holes, if any, amount to a few percent of the whole sample surface area.

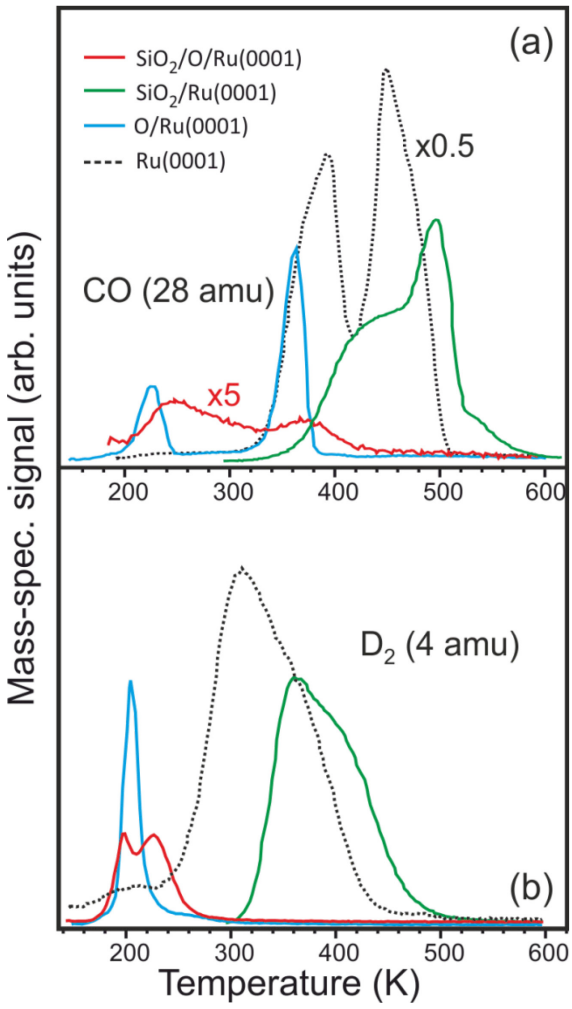

Figure 4.1: Comparison of TPD spectra of CO (a) and D_2 (b) from silicate samples and clean and O-precovered Ru(0001) surfaces.

Adsorption experiments with 10^{-6} mbar D_2 at 150 K on the "as prepared" samples did not show any D_2 desorption signal due to the fact that atomic oxygen on substrate surface blocks the sites for D_2 dissociation [174, 184]. Therefore, in the next step, it is necessary to address the preparation of the clean Ru(0001) surface underneath the silicate; otherwise our "detector" will be silent toward the gases whose chemisorption is blocked by oxygen. In an attempt to desorb the O atoms from the Ru support, the

samples were annealed at 1275 K for 1 min in UHV. This treatment strongly enhanced the D_2 uptake due to the removal of atomic oxygen, while CO adsorption is affected only to a minor extent. The D_2 desorption profile featuring two peaks at 195 and 225 K (red curve in Figure 4.1b) is considerably different from that of the clean Ru(0001) surface (dashed curve in Figure 4.1b) and is similar to the one from the Si-free (O-covered) sample also shown as blue spectrum in Figure 4.1b for comparison. The integral of the TPD area imply that D atoms cover a substantial portion of the support for the annealed silicate samples. It looks like D_2 penetrates the silicate easier than does CO. However, after the annealing procedure, Ru surface underneath the silicate remains to be covered by oxygen, albeit to a lower coverage as compared to the "as prepared" sample. Annealing for a longer time (up to 15 min) resulted in film dewetting, as evidenced by the attenuation of the principal phonon at 1300 cm^{-1} and concomitant growth of the broad band at ~1250 cm^{-1}, which is characteristic of bulk-like silica [9, 119].

In order to remove O species via its interaction with atomic D and subsequent desorption as water, higher pressures of D_2 (1 mbar) at 470 K were introduced to the "as prepared" silicate samples and cooled down to 300 K before D_2 was pumped out (Figure 4.2). After this treatment, the principal 1300 cm^{-1} band IRA spectra is only slightly red-shifted, by a few wavenumbers, thus indicating that the silicate structure is preserved. The TPD spectrum from such a sample (green curve in Figure 4.1b) is very similar to the spectrum of D_2 from the clean Ru(0001) surface, although the profile is shifted by ~40 K to higher temperatures and the intensity is reduced by ~33%.

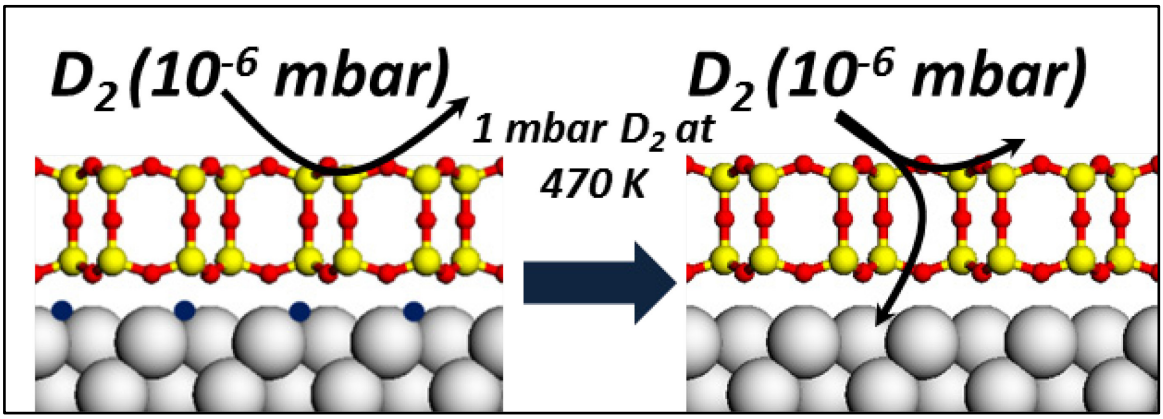

Figure 4.2: The procedure for the removal of interfacial oxygen between silicate and Ru(0001).

In attempt to see whether these effects are solely attributed to the high D_2 pressure used in this experiment, the sample was further exposed to 10^{-6} mbar D_2 at 300 K. Figure 4.3a displays a series of sequential TPD spectra at various exposure times. It can be seen that the D_2 uptake (i.e., integral desorption area at saturation) is almost independent of the pressure used (1 mbar vs 10^{-6} mbar). Moreover, the TPD spectra and the plots of integral desorption area vs. exposure time are very comparable to those observed for the clean Ru(0001) surface [174]. This indicates that D_2 can easily reach the Ru(0001) surface at 10^{-6} mbar pressures even in the presence of the silicate layer. If, however, the silicate covered Ru sample is exposed to D_2 at temperatures below 200 K, the D_2 uptake is considerably reduced (Figure 4.3b), whereas this behavior is almost independent of the adsorption temperature (100-300 K) on the pristine Ru(0001) surface [174, 186]. Owing to the fact that D_2 readily dissociates on Ru(0001) and the resulting D atoms easily diffuse across the surface at these temperatures [178, 181, 187], these findings indicate that the permeation of D_2 through the silicate depends on temperature. However, the silicate layer can also affect the diffusion of D atoms on Ru as well. Therefore, in order to rationalize the TPD and IRAS results obtained upon exposure of metal-supported silicate layers to various gases, it is important that not only gas transport through the silicate, but also adsorption (e.g., dissociation) and diffusion of adsorbed species on the metal surface must be taken into account.

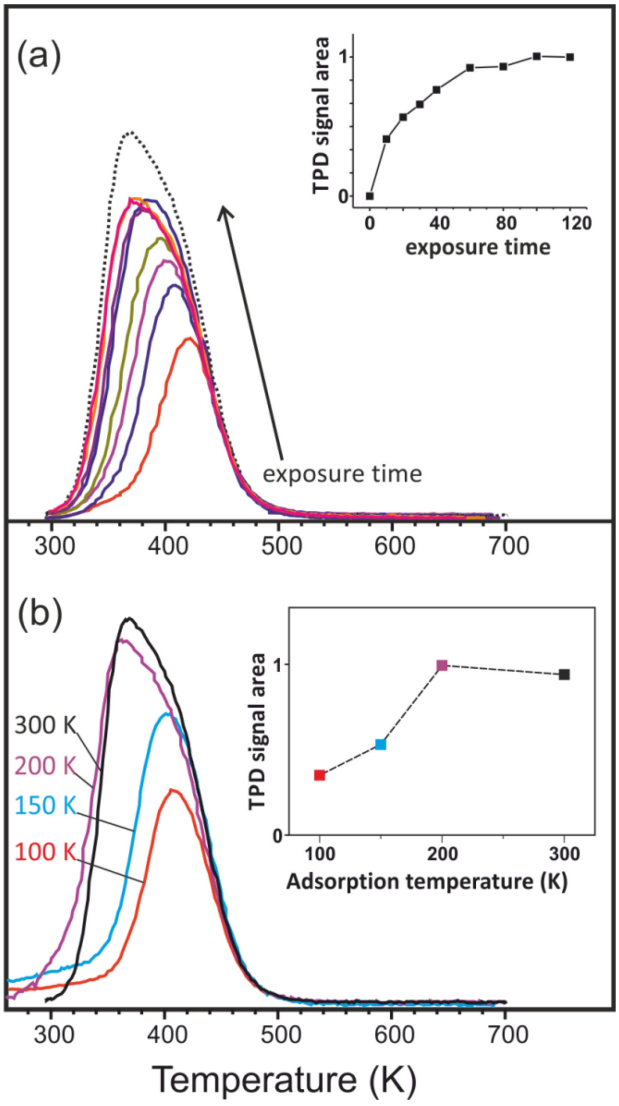

Figure 4.3: TPD spectra and TPD signal areas (in the insets) of $2x10^{-6}$ mbar D_2 adsorbed onto SiO_2/ Ru(0001) as a function of exposure time (all exposures are at 300 K) (a) and temperature (all exposures are 2 min) (b) The dashed line in (a) shows the spectrum after exposure to 1 mbar D_2. TPD signal areas in the insets are normalized to the maximum.

As a following step, CO adsorption on the silicate having a clean Ru support underneath was examined. In the next set of experiments, the sample was exposed to $2x10^{-6}$ mbar CO and IRA spectra were recorded simultaneously. We first performed the measurements at a sample temperature of 100 K. After the IRA spectra of CO adsorption were taken, CO was desorbed in front of a mass spectrometer in the TPD mode by heating to 700 K with a heating rate of 3 K/s. The same experiment was then performed again at stepwise-increased sample temperatures; between 100 and 350 K. Figure 4.4 collects consecutive IRA spectra at indicated temperatures, displaying the CO adsorption kinetics on a metal support underneath the silicate.

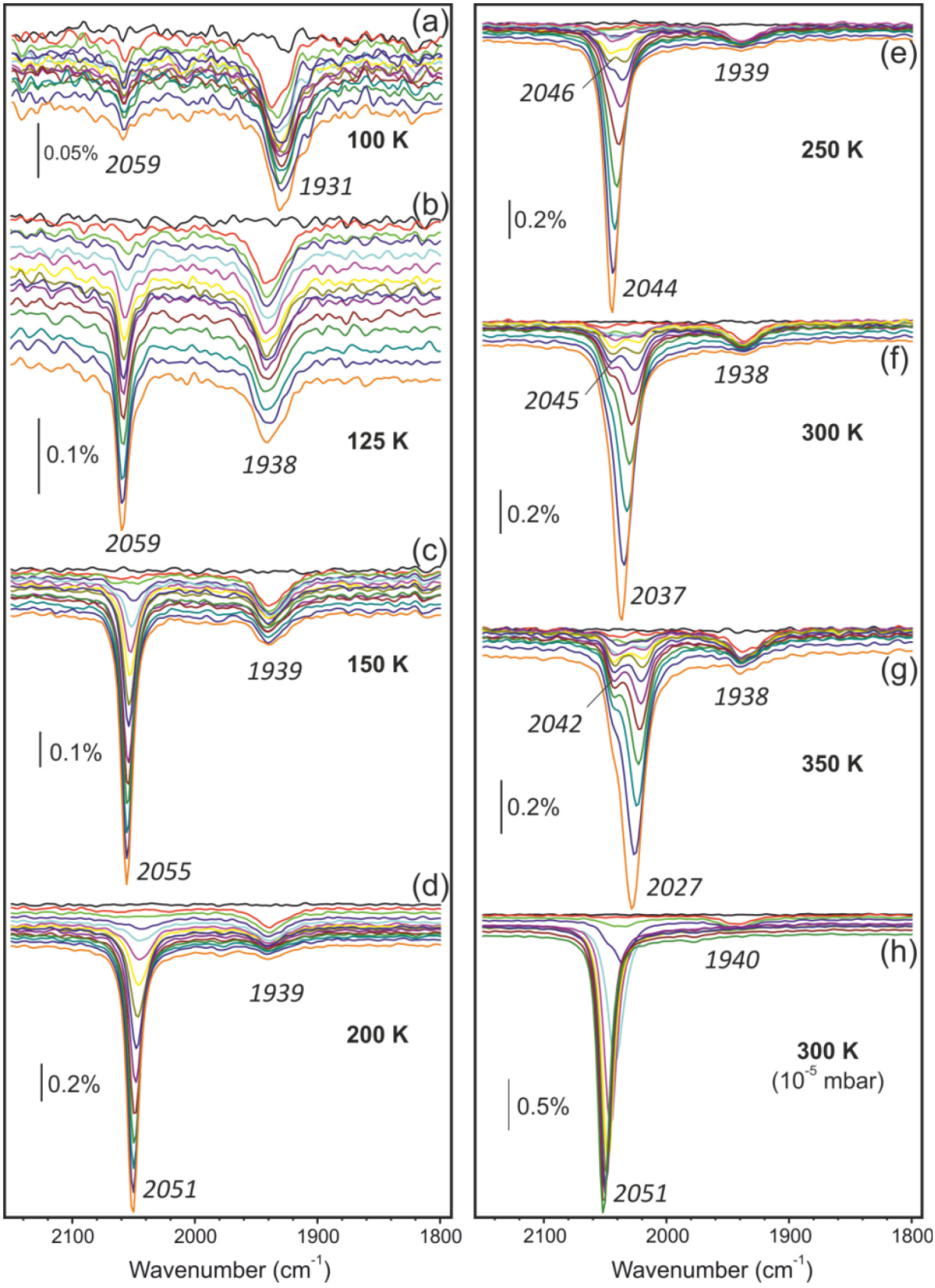

Figure 4.4: Consecutively recorded IRA spectra measured on SiO_2/Ru(0001) in $2x10^{-6}$ mbar CO (a-g) and 10^{-5} mbar CO (h) at the indicated temperatures. Each spectrum takes takes 12 s. The last shown spectrum corresponds to the 6-min exposure. Spectra are offset for clarity.

At low temperatures (100-125 K, Figure 4.4a,b), the IR band peaking at 1931-1938 cm^{-1} (thereafter referred to as band I) saturates immediately, therefore indicating a high sticking coefficient of respective CO species the same as on the clean Ru(0001) surface. Then the band at 2059 cm^{-1} (the band II) appears, that apparently saturates without any shift. For comparison, Figure 4.5 shows the series of IRA spectra recorded in a similar way over the clean Ru(0001) surface at 100 K, although exposed to a much lower pressure (10^{-8} mbar) in order to monitor spectral changes at increasing CO exposures. The signal appears first at~1995 cm^{-1} and then continuously shifts to 2060 cm^{-1} upon increasing CO coverage until saturation, in good agreement with previous results [173].

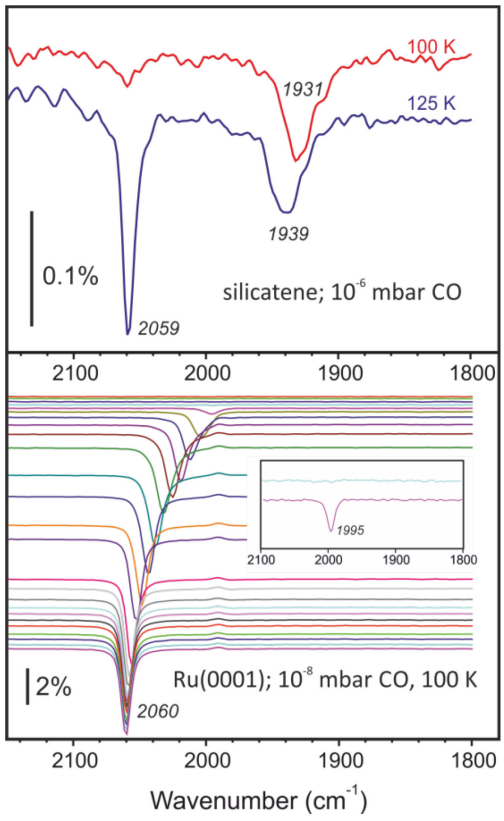

Figure 4.5: (Top) IRA spectra of CO on SiO_2/Ru(0001) measured in 2×10^{-6} mbar CO at 100 and 125 K. (Bottom) Consecutive IRA spectra for clean Ru(0001) upon exposure to 10^{-8} mbar CO at 100 K. The inset zooms in the first spectra. All spectra are offset for clarity.

Band II dominates the spectra at higher temperatures, as can be seen in Figure 4.4a-g. The signal gains intensity and gradually shifts to 2055 cm^{-1} at 150 K, and further to 2051 cm^{-1} (200 K), 2044 cm^{-1} (250 K), 2037 cm^{-1} (300 K), and 2027 cm^{-1} (350 K), all measured after the same CO exposure (2 x 10^{-6} mbar, 2 min). Concomitantly, the low-frequency band I at 1939 cm^{-1}, which always becomes visible first, strongly attenuates and disappears at high exposures. The spectra at 250, 300, and 350 K revealed an

additional band (band III) centered at ~2045 cm^{-1}, which might overlap with band II at low temperatures. The frequency of band III almost doesn`t change with adsorption temperature and exposure of CO, however band II clearly shows the blue shift by about 5-10 cm^{-1} upon increasing CO coverage. It has turned out that at temperatures above 125 K saturation can hardly be achieved in $2x10^{-6}$ mbar of CO within reasonable time. To reach saturation, the experiments had to be performed at higher CO pressures, at least 10^{-5} mbar as shown in Figure 4.4h. The spectrum at saturation shows only a very strong band II at 2051 cm^{-1}, i.e. at considerably higher frequency than 2037 cm^{-1}, observed in $2x10^{-6}$ mbar CO (both at 300 K; compare f and h of Figure 4.4). This blue-shift agrees well with the coverage-dependent behavior observed on a clean Ru(0001) surface.

The final spectra from the plots presented in Figure 4.4a-h are compared in Figure 4.6a. The corresponding TPD spectra recorded after each IRAS measurements are displayed in Figure 4.6b. First we note that the integral IRAS signal is proportional to the CO desorption signal (Figure 4.6c), both increase with adsorption temperature (inset in Figure 4.6b). Therefore, we conclude that the CO adsorption geometry doesn`t influence IRA signal intensity (CO axis is vertical or tilted with respect to the surface) due to the metal selection rules, but IRA signals exclusively reflect CO surface population. In addition, this linear relationship (see Figure 4.6c) allows us to interpret the total CO coverage by IRAS.

As in the case of D_2 (see Figure 4.3b), the CO uptake increases in the temperature range from 100 to 200 K and then almost doesn`t change between 200 and 300 K. The desorption profile falls into the range of temperatures characteristic for CO desorption from a metallic Ru surface, but it is shifted by ~25 K (measured at the descending edge) toward higher temperatures, i.e. in the same way as D_2 (~40 K, Figure 4.1b). In addition, a notable shoulder at the high-temperature side is seen, which is absent for the pristine Ru(0001) surface. Compared with pristine Ru(0001), the CO uptake over the silicate-covered sample is reduced by ~38% (compare to ~33% observed for the D_2 uptake (Figure 4.1b)). Since the CO saturation coverage on Ru(0001) is about 0.66 of monolayer (ML) (with respect to the number of the Ru surface atoms) [173, 176], reduction by ~38% yields approximately 0.5 ML for the saturated CO coverage on Ru(0001) underneath the silicate. Correspondingly, we estimate 0.66 ML for the

saturation D coverage underneath the silicate using the saturation coverage of 1.0 ML for clean Ru(0001) as the reference [174, 178].

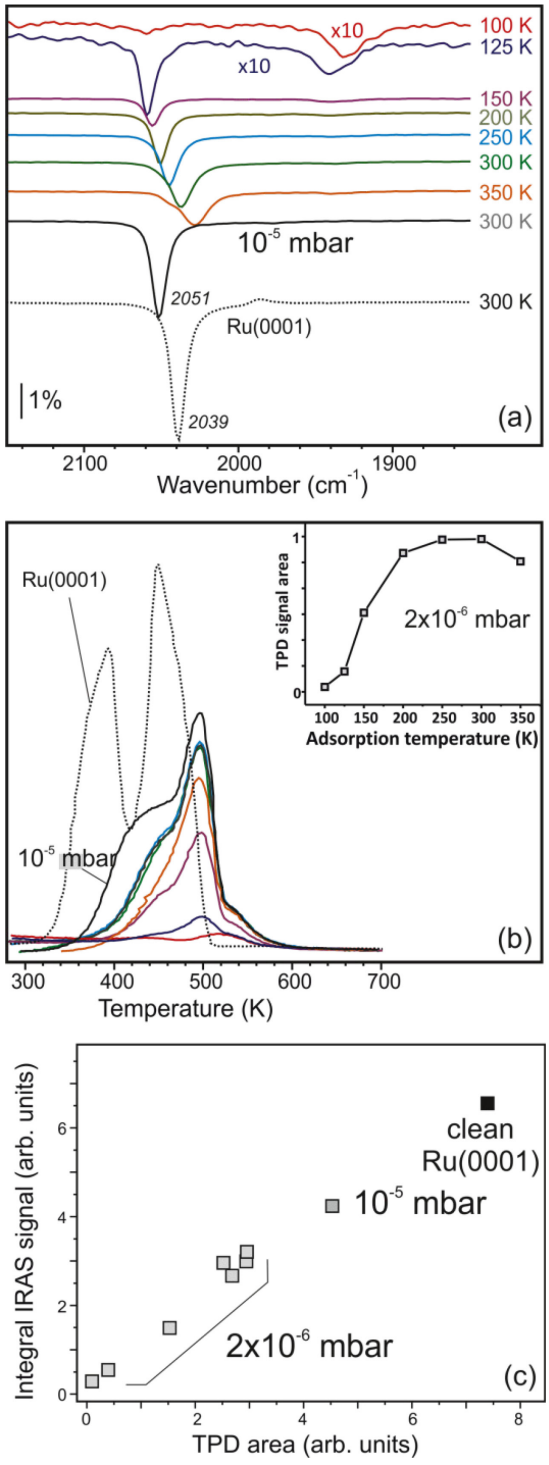

Figure 4.6: (a) The final IRA-spectra taken from each plot (a-h) presented in Figure 4.4. (b) The corresponding TPD spectra of CO taken after the IRAS measurements. The inset shows integral signal, normalized to the maximum, as a function of adsorption temperature at 2×10^{-6} mbar CO. The results for the clean Ru(0001) surface are shown by the dashed lines. The results for 10^{-5} mbar CO pressure are marked, for clarity. Plot (c) demonstrates the linear relation between all presented IRAS and TPD signals.

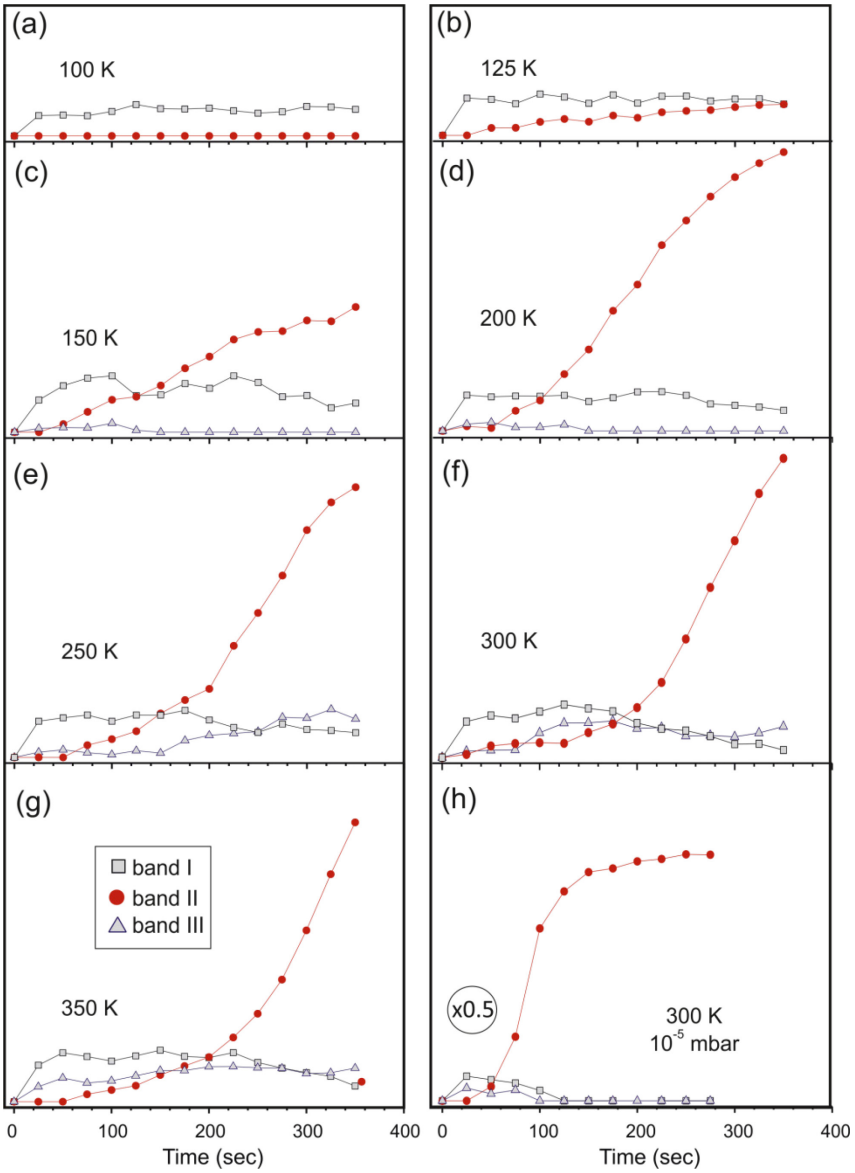

Figure 4.7: Kinetics of the IRA signal intensities of the each band (I,II, and III) obtained from the spectra presented in Figure 4.4.

As the vibrational IRA bands related to the D atoms on Ru(0001) (relatively strong at 602 and weak at 833 cm^{-1}) [177] could not be measured with our spectrometer, the adsorption kinetics were analyzed by IRAS for CO adsorption only. Figure 4.7 displays the integral intensity of the each band (I, II, and III) as a function of exposure time at a specified temperature measured for the spectra depicted in Figure 4.4. Band I appears immediately with introducing CO, thus indicates that the respective CO species has the sticking coefficient as high as on the bare Ru(0001) surface. Moreover, its coverage is independent of adsorption temperature. Therefore, we have tentatively assigned those species to the "macroscopic holes" exposing clean Ru. However, the measured frequency (~1935 cm^{-1}) is much lower than ever detected on Ru(0001) [173]. This

implies that the vibrational properties of CO in such holes are strongly affected by the presence of the silica layer. CO adsorbing in two-fold (bridged) coordination has same frequencies in this spectral region for many metals, however this is unusual for the Ru(0001) surface. Nevertheless, the intensity of band I represents a minority species and disappears at high CO coverage.

Apparently, the site corresponding to band III at ~2045 cm^{-1}, which became apparent at T > 200K, populates the second, as better seen in e-g of Figure 4.4. The frequency corresponds to the region typical for linear CO species on metallic Ru. Once again, the total CO uptake is not affected by these species.

It is obvious that band II dominates the spectra at high CO exposures and elevated temperatures. However, it is apparent in Figure 4.7 that above 200 K, the intensity of this band present an induction period after which it steeply increases, ultimately approaching saturation (Figure 4.7h). CO pressure strongly governs this induction period meaning the higher the pressure, the smaller the induction period as shown in Figure 4.8:

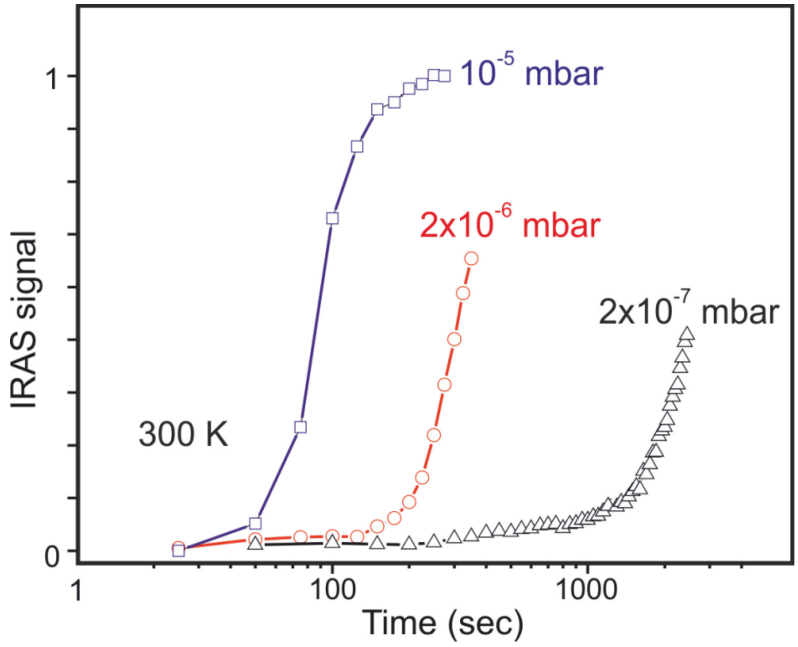

Figure 4.8: Kinetics of the CO uptake measured by IRAS at 300 K at three different CO pressures as indicated. Note the logarithmic scale for the exposure time.

Finally, it should be noted that after the adsorption of CO, the silica phonon band at 1300 cm^{-1} is shifted toward higher frequencies by ~5 cm^{-1}. The similar behavior was

also observed for the "O-rich" silicate films having O directly adsorbed on the Ru support [88]. Correspondingly, this shift indicates a further decoupling of the silicate with the metal support due to the repulsive interaction between oxygen in the bottom layer of silicate and CO.

4.2 Discussion

The results that are presented indicate that the silicate layer on a ~1 cm scale (diameter of the Ru single crystal) has a good integrity which allows us to neglect permeation of gases through macroscopic holes (on average) in order to rationalize the TPD and IRAS results. The main observations for CO and D_2 adsorption on the silicate-covered Ru(0001) surface can be elaborated as follows:

i. Chemisorption of D_2 and CO readily takes place on the Ru(0001) support underneath the silicate layer, when exposed to 10^{-5}-10^{-6} mbar at temperatures above 200 K. The highest surface coverages were ~0.5 ML for CO, and ~0.65 ML for D which are about 35% lower than on the pristine Ru(0001) surface (Figure 4.1).

ii. The CO and D_2 uptakes are strongly depend on temperature; both are considerably reduced at temperatures below 200 K, more remarkably for CO (Figure 4.3b and Figure 4.6b).

iii. When compared to the bare Ru(0001) surface, D_2 desorbs ~40 K and CO desorbs ~25 K higher temperatures (Figure 4.1).

iv. In contrast to D_2, which exhibits a Langmuir-type adsorption kinetics (Figure 4.3a), CO adsorption at T>200 K presents an induction period followed by self-acceleration (Figure 4.7). The induction time decreases with increasing CO ambient pressure (Figure 4.8).

v. At least three CO surface species having different sticking coefficients and fractional coverages are detected from CO adsorption experiments.

It is apparent that, a general scenario upon exposure of the silicate covered Ru(0001) to the standard gases must involve the following steps: (1) penetration of a molecule

through a pore in the silicate; (2) adsorption on the metal surface right behind the pore; (3) diffusion of adsorbed species across the metal surface underneath the silicate layer (Figure 4.9). Step (1) which may include ballistic and nonballistic components can occur either through specific pores, associated with large N-membered rings, or uniformly. Step (2) may additionally include dissociation, as in the case of D_2. Moreover, the adsorption site on the metal surface may be occupied by a previously adsorbed molecule (atoms) at low surface diffusion. Additionally, all steps may be temperature dependent and have different rate constants.

Here at the studied temperatures (100-300 K), the dissociation of hydrogen takes place readily on the Ru surface [174, 177]. Surface diffusion of hydrogen and deuterium on Ru(0001) at low coverage was studied earlier using laser-induced thermal desorption techniques [179, 180].

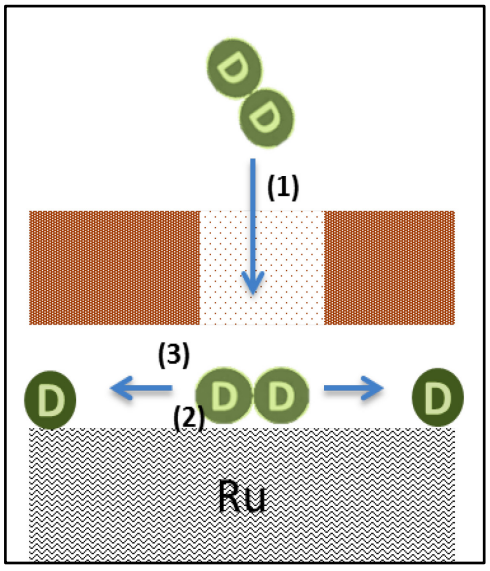

Figure 4.9: Schematic representation of the adsorption scenario on the silicate films (1) permeation (2) adsorption and (3) diffusion steps.

In the temperature range between 260 and 330 K, the surface diffusion coefficient of deuterium was expressed in Arrhenius form as $D = 4.6 \times 10^{-4}$ cm^2/s $exp(-4.1 (\pm 0.5)$ kcal $mol^{-1}/ RT)$. Recently, helium spin-echo techniques and density functional theory (DFT) calculations exhibited a tunneling-dominating fast diffusion at low temperatures (below 120 K) with the hoping rate of about 2×10^9 s^{-1}. By using the well-known formula for the diffusion length ($L = 2\sqrt{Dt}$), one can convince oneself that, at the time-scale of our experiments (typically, > 10 s), the diffusion of the adsorbed D takes place very fast on

Ru(0001), consequently leading to a uniform D population across the surface, even at 100 K. Therefore, the permeation step (1) must be responsible for the temperature dependence observed for D_2 uptake, assuming that D diffusion is not strongly affected by the silicate layer.

CO diffusion on Ru(0001) is more complex to elaborate. There is a strong dependence of the diffusion coefficient on CO coverage which is proved by laser-induced thermal desorption measurements [188]. For CO coverages below 0.3 ML, the coefficient measured at 290 K was approximately constant at ~10^{-8} cm^2/s. As the CO coverage increased to 0.6 ML, the surface diffusion coefficient also increased dramatically up to 10^{-6} cm^2/s. At some temperatures (210-370 K) and CO coverages, Arrhenius behaviour is observed for the diffusivity. At 0.3 ML coverage, the diffusion coefficient is fitted by $D = 0.38\ cm^2/s\ \exp(-11\ kcal\ mol^{-1}/RT)$. At increasing CO coverage from 0.3 to 0.6 ML, both the activation energy and pre-exponential factor decrease, i.e. from 11 to 6 kcal/mol, and from 0.38 to 0.06 cm^2/s, respectively. This behaviour was explained by the strong repulsive CO-CO interaction. Such complexity manifests an assessment for the CO diffusion kinetics under our conditions rather difficult. By using the above values, the diffusion length was estimated to be 10^3-10^4 nm at 300 K, but it becomes close or even smaller than the Ru(0001) lattice constant at 100 K. Therefore, at low temperatures, one should take into account at least diffusion step (3) in CO adsorption experiments.

It is a well-known fact that the CO stretching frequency depends almost linearly on CO coverage (see ref [173] and Figure 4.10). With this respect, such a relationship could be used for determining the CO coverage underneath the silicate. However, comparing the IRA spectra, shown in Figure 4.6a, it can be seen that the band measured for the silicate covered surface at 300 K, peaks at 2051 cm^{-1} at saturation, i.e. at a frequency much higher than 2039 cm^{-1} observed on pristine Ru(0001), although for a higher coverage in the latter case. Even larger difference (~17 cm^{-1}) was observed if one compares spectra at equal, i.e. 0.5 ML coverage (Figure 4.10).

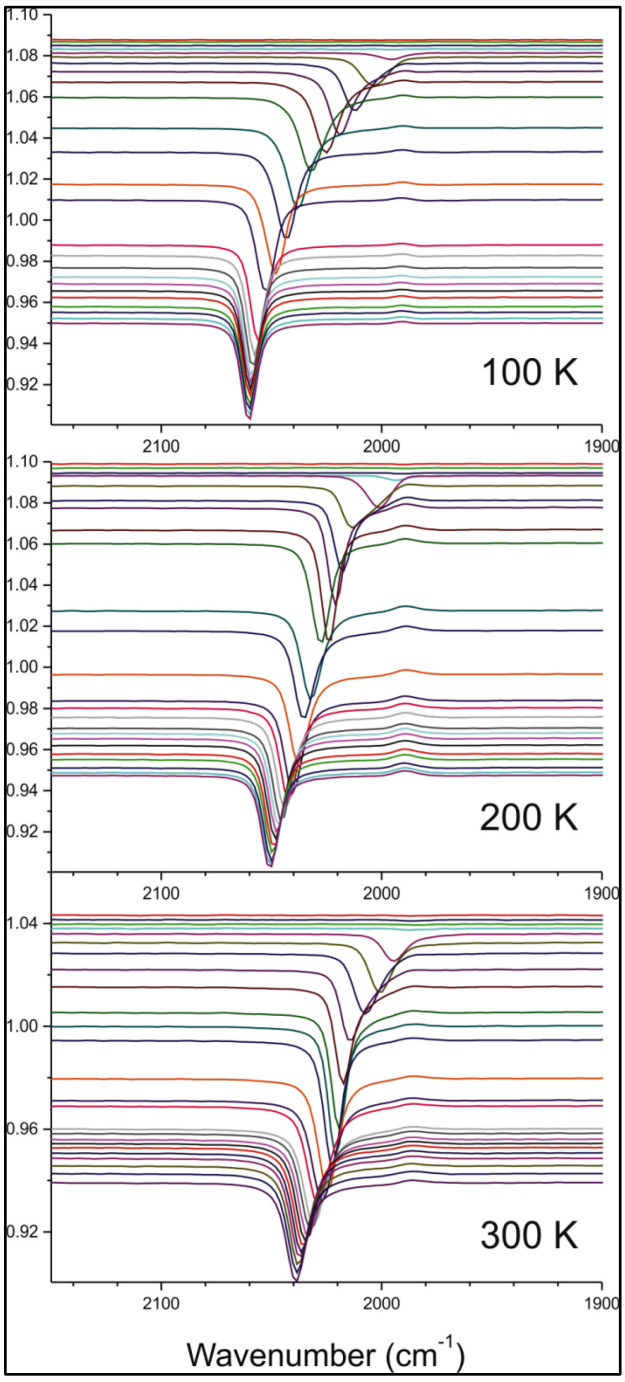

Figure 4.10: Consecutive IRA spectra of CO adsorption on the clean Ru(0001) surface in 10^{-8} mbar CO at indicated temperatures. The spectra are offset for clarity.

Therefore, the stretching frequency of CO adsorbed on the Ru support is considerably higher in the presence of silicate layer above, although the frequency is blue-shifted at increasing CO exposure in the same way as on the pristine Ru (compare g and h of Figure 4.4 and Figure 4.10). If one assumes that the same difference holds true for adsorption at low temperatures, the band at 2059 cm^{-1} observed at 125 K for the silicate sample would correspond to the coverage of about 0.4-0.5 ML, which would be almost

an order of magnitude higher than the total CO coverage (0.05 ML) measured on this sample (Figure 4.6b,c). Uniform penetration of CO doesn't explain this finding. Indeed, if CO could penetrate through all-cells in the honeycomb-like structure, eventually resulting in one CO molecule per polygonal cell, one would expect to observe one IR band growing in intensity and blue-shifting with increasing CO exposure. This shift must resemble to that observed for pristine Ru(0001), i.e.~20-30 cm^{-1} (see Figure 4.10). In fact, a-d of Figure 4.4 shows that band III grows almost without any shift. This indicates that CO molecules penetrate through specific pores and accumulate on the metal surface behind the pore to relatively high local concentration because of low surface diffusivity at low temperatures. Once the temperature is increased, the surface diffusion sets in, which reduces the local CO concentration and thus causes the red-shift of the IRAS band, despite the total CO coverage increase, as shown in Figure 4.6a. Apparently, the local concentration depends on the flux of penetrating molecules and surface diffusivity. Within such a description, band III at ~2045 cm^{-1}could tentatively be associated with CO species the behind pores at a quasi-steady state. Upon reaching the saturation coverages, CO molecules become uniformly covering the whole Ru surface. As a result of this, bands I and III totally disappear.

It seems that the CO desorption upon heating occurs through the same pores as the adsorption. Since the molecule requires some time to reach these pores to escape, the desorption is delayed as compared with the pristine Ru(0001), thus resulting in the temperature shift in the TPD spectra (Figure 4.1). In the case of D_2, the desorption may be delayed even more, since it additionally involves D recombination to form D_2 which desorbs. Indeed, the observed shift for D_2 (~40 K) is higher than for CO (~25 K).

In order to support the conclusion about CO and D_2 penetration through specific pores, site blocking experiments were done. For this, the silicate was first exposed to 10^{-6} mbar CO at 300 K for 1 min, which results in CO coverage of about 0.05 ML. Subsequently, 10^{-6} mbar D_2 was dosed to this surface at 300 K for 2 min. The TPD spectra with and without CO preadsorption are compared in Figure 4.11.

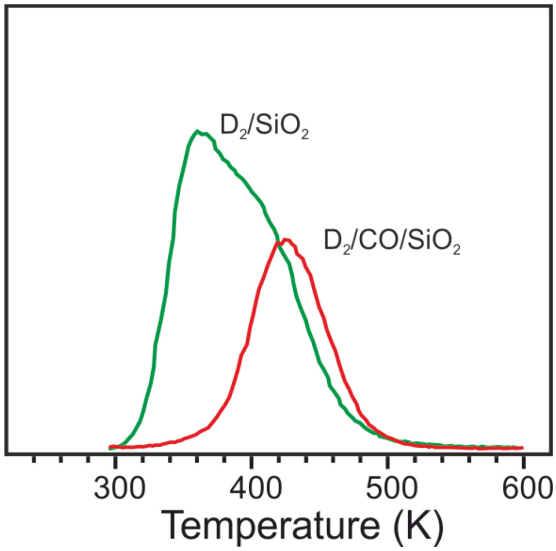

Figure 4.11: D_2 signals in TPD spectra of the silicate after exposure to 2×10^{-6} mbar D_2 at 300 K for 2 min on the clean sample (green line) and the sample first exposed to 2×10^{-6} mbar CO at 300 K for 1 min (red line).

It is clear that preadsorbed CO suppresses the D_2 uptake by a factor of ~2. Although CO blocking of D_2 adsorption (dissociation) is well-documented in the literature for the Ru(0001) surface [182, 184], the D_2 adsorption cannot be changed so drastically since the total amounts of preadsorbed CO is too small. Furthermore, previous CO and D_2 coadsorption studies by TPD revealed that D_2 desorption temperature shift toward low temperatures, however in our experiments it shifts to higher temperatures. Therefore, these findings can hardly be explained by uniform flux of D_2 molecules penetrating the silicate and approaching the CO-precovered Ru surface. It seems more plausible that the D atoms, which reach the metal surface through those pores, exhibit limited surface diffusivity within the precovered CO ad-layer. For the same reason, D_2 desorption is delayed in time during TPD run, thus causing a further shift to higher temperatures in the TPD spectra (Figure 4.11).

With the light of the combined results, it is apparent that a perfect crystalline silicate is, in essence, impermeable for CO and D_2. The penetration of gas molecules occurs through the defects (pores) associated with larger than 6-membered rings which are commonly present in the amorphous silicate. Since in all these experiments CO and D_2 ambient was kept at room temperature, ballistic flow through the pores cannot explain the observed temperature dependence for CO and D_2 uptake (Figure 4.3b and Figure 4.6b). In fact, Figure 4.6 shows that, at temperatures below 200 K, the CO uptake

linearly grows in time, with the rate presenting Arrhenius behaviour (Figure 4.12) yielding an apparent activation energy of 2.3 kcal/mol.

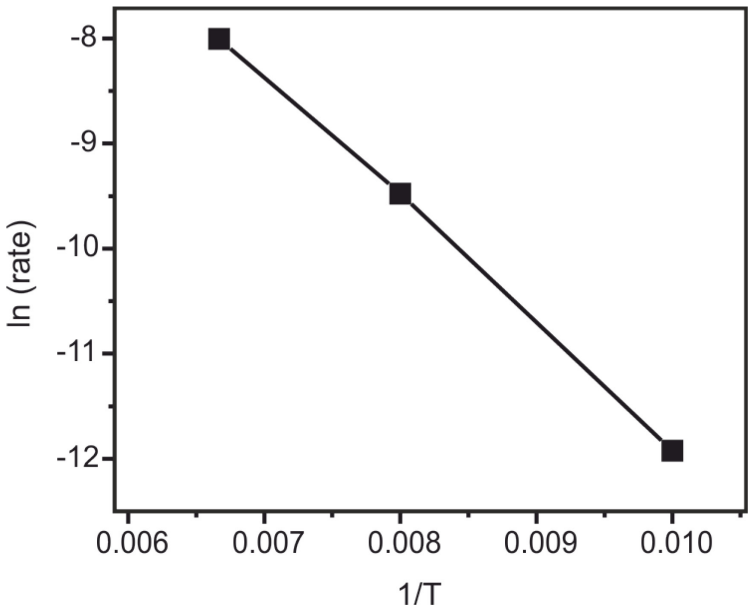

Figure 4.12: Arrhenius plot for CO adsorption rate measured from the IRAS results, shown in Figure 4.4, at temperatures 100 – 150 K. The slope corresponds to the apparent activation energy 2.3 kcal/mol.

CO diffusion on pristine Ru(0001) has remarkably higher activation energy (between 6 and 11 kcal/mol) [188] than this energy. As a consequence, the temperature dependence must be assigned to the activated penetration of CO through the silicate pores rather than to the surface diffusion. In accordance with the kinetic diameters of D_2 and CO, which are about 2.9 and 3.8 Å, the effective pore size allowing penetration would correspond to 8-membered rings as possible candidate.

The observation of an induction period (Figure 4.7 and Figure 4.8) for CO adsorption remains obscure. As mentioned previously, CO surface diffusivity on clean Ru(0001) exhibits nonlinear enhancement at increasing local CO coverage [188]. Therefore, it is highly possible that the increased local CO coverage right behind the pore, which is determined, basically, by the fluxes penetrating molecules and those migrating away from the pore, both increasing with temperature, reached the situation when CO diffusivity strongly enhances due to the CO-CO repulsive interaction [188]. Additionally, CO diffusion underneath the silicate layer can be further favoured by an increase of the distance between the silicate and the metal surface. In this respect, it can be instructive here to address recent studies on intercalation of metal-supported graphene [166-168, 189].

Particularly, it was found that the fully graphene covered Ru(0001) surface became passivated to O_2 adsorption at room temperature and only activated at elevated temperatures (>500 K). The adsorbed oxygen which is intercalated between the graphene overlayer and the Ru(0001) surface decouples the graphene layer from the substrate, forming a quasi-freestanding graphene layer floating on O/Ru(0001) [189].The intercalation of oxygen competes with the etching of graphene that occurs at domain edges and becomes significantly dominant at T > 400 ^{o}C [167]. It was further claimed that not only atomic O, formed by dissociation on the Ru surface surrounding the graphene domain, but even molecular O_2 diffuses between the graphene and the metal. Recently, it was also shown that CO also permeates through the graphene/ Pt(111) interface, but only through open channels at island edges at pressures >10^{-6} mbar [166]. (For a fully covered graphene layer exposed to 10^{-6} mbar at 300 K for ca. 30 min., no adsorption took place.) When the kinetic diameter of CO (3.76 Å) and the distance between graphene and the Pt(111) substrate (3.30 Å) are considered, it was claimed that CO intercalation enlarges the distance between the graphene sheet and the Pt surface as assisted by DFT calculations, yielding the distance of about 5.9 Å [166]. The calculations also revealed that CO adsorption on Pt(111) is weakened by the presence of the graphene above, in agreement with experimental results indicating that CO desorbs in UHV conditions even around room temperature. It was also previously reported that O atoms desorb from graphene/ Ru(0001) interface earlier temperatures than the bare Ru(0001) [189].

4.3 Conclusions

Exposure of CO and $D_2$to a double-layer silicate film grown on Ru(0001) results in intercalation of the silicate/Ru interface.The CO and D_2 uptakes exhibit strong temperature dependence: Both are considerably reduced at temperatures below 200 K. At T>200 K,CO adsorption exhibits an induction period followed by self-acceleration. The induction time decreases with increasing CO ambient pressure. The results reveal a complex response of such systems upon gas exposures which involves gas transport through the pores (associated with larger membered rings, i.e. >6) in the silicate, subsequent chemisorption, and diffusion across the metal surface underneath the silicate.

5. Oxidation of the Ru(0001) Surface Underneath a Silicate Film: Towards Chemistry in Confined Space

As shown in the previous chapter, due to the presence of a relatively large space between the silicate sheet and the metal support, small molecules may intercalate the interface, diffuse and ultimately react on the metal surface. Although it is potentially interesting, the studies on chemical reactions in such confined space remain in its premature state. To date, only a few studies have been reported for metal-supported graphene system in which CO, H_2O and O_2 can diffuse into the space between graphene and substrate, and even chemical reactions may happen in the two-dimensional space under graphene sheet [166-168]. In this respect, metal-supported bilayer silicate films, which combine an ultrathin "membrane" and a chemically active metal surface underneath, may become interesting hybrid materials, in particular catalysis as the silica is a robust material in catalytically relevant atmosphere as shown in the previous section.

Three types of scenario are expected for chemical reactions over silicate/metal system exposed to ambient gases: (i) penetration of molecules through "pores" in the film; (ii) chemisorption on the metal surface right behind the pore and subsequent diffusion across the metal surface; (iii) surface reactions, and finally (iv) desorption of products (if any) back through the pores in the film. The first two steps were addressed in the previous chapter with respect to CO and D_2. The results revealed that a perfect crystalline silicate which is composed of a honeycomb-like structure of 6-membered rings) is, in essence, impermeable even for these small molecules. Their penetration seems to occur through the pores associated with the large N-membered rings present in the amorphous portion of the films.

In this chapter, we address intercalation and subsequent reaction of oxygen. It has been previously observed that the "as prepared" silicates grown on Ru(0001) commonly contains oxygen atoms adsorbed directly on the metal surface [88, 119]. The amount of oxygen may be reduced by annealing in ultra-high vacuum (UHV) and recovered by re-oxidation, without any structural changes in the silicate films. Owing to the fact that Ru(0001) surface is susceptible to form oxidic phases, such as a well-ordered RuO_2(110) films, which is considered as the active phase in the catalytic reactions

(chlorine evolution (electrochemistry) or Deacon process) [190], we focused here on oxidation of the Ru(0001) surface underneath the film in more detail, in particular at high O_2 pressures and elevated temperatures.

It is well established that under UHV conditions oxygen exposure, (2x2)-O, (2x1)-O and (2x2)-3O overlayers on Ru(0001) can be formed. Additionally, oxygen exposures of several millions Langmuirs can produce (1x1)-O overlayer and also varying concentration of subsurface oxygen [191]. This excessive oxidation of the Ru(0001) surface which result in the O uptake more than a monolayer, has been intensively studied since this so-called "oxygen-rich" Ru(0001) surface was found to be very active in the CO oxidation reaction. Böttcher and co-workers discussed the presence of sub-surface oxygen species which can be formed without any formation of Ru oxides depending on the exposure temperature [192, 193]. Furthermore, Over and co-workers clearly demonstrated that the oxygen-rich Ru(0001) surface, which is known to be extraordinarily active in the oxidation of CO molecules consists of RuO_2(110) and (1x1)-O patches [194-196]. Further studies showed that it is adsorbed oxygen atom located in terminal position above the coordinatively unsaturated Ru sites on RuO_2(110) that is involved in CO oxidation [197-200]. Nonetheless, it is fair to say that chemisorbed oxygen, surface oxide, buried oxides, and subsurface oxygen may, in principle, all coexist in the near surface region of Ru(0001), thus leading to a rich oxygen-ruthenium surface chemistry [190, 201]. Indeed, a low energy electron microscopy study on the oxidation of Ru(0001) revealed that oxidation beyond an initial (1x1)-O adlayer phase produces a substantial spatial inhomogeneity in the oxide formation across the surface [202].

5.1 Case 1: Pure Silicate Films

In order to grow oxide layer more than a monolayer on Ru(0001), we need elevated temperatures and pressures. Commonly, thin RuO_2(110) films are prepared by exposing Ru(0001) to high doses of molecular oxygen at 10^{-6}-10^{-4} mbar and at high temperatures [197, 198, 203, 204]. In this study Ru(0001) was oxidized in 10^{-5} mbar of O_2 at 700 K for 45 min, and cooled to room temperature in the same oxygen ambient. The characteristic LEED pattern of RuO_2(110)/Ru(0001), which is well-documented in the literature [195], was observed after this procedure. By using Auger O (at 510 eV) and

Ru (at 280 eV) signals ratio (~0.7, see a top spectrum in Figure 5.1b) , the nominal film thickness was estimated to be 6 ML, based on our calibration using 3O(2x2)-Ru(0001) surface as a benchmark [203]. Additionally, thermal desorption of O_2 from the resulted surface, shown in Figure 5.1a, nicely reproduces previously reported TPD spectra of RuO_2(110)[197], showing two peaks at ~400 K and ~1005 K. The high temperature peak corresponds to Ru-oxide film decomposition, whereas the weakly bonded oxygen species (at ~400 K) are assigned to adsorbed oxygen atoms located in terminal position above the coordinatively unsaturated Ru sites on RuO_2(110) [197].

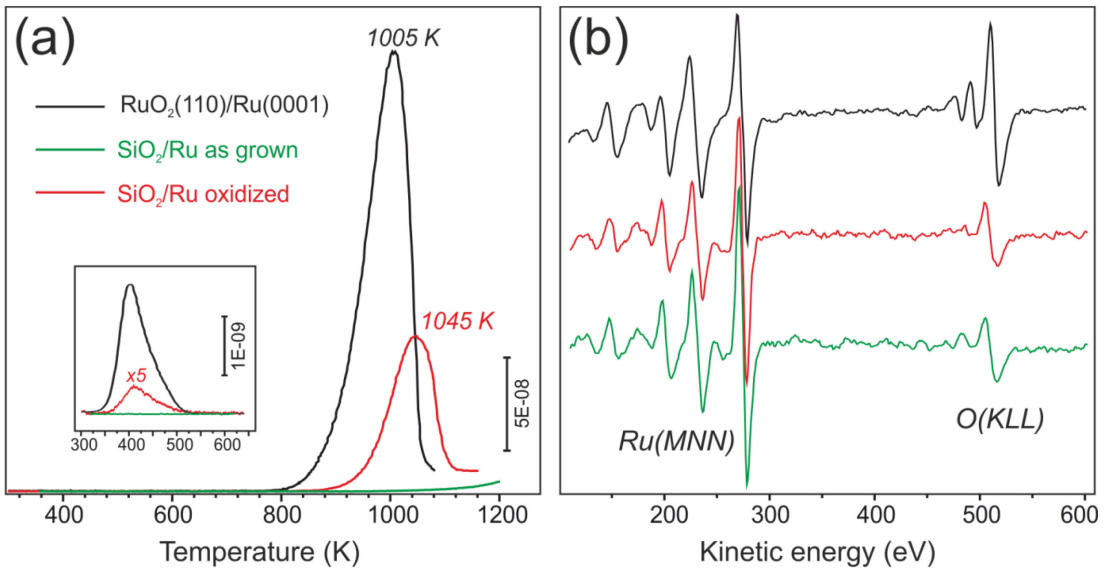

Figure 5.1: O_2-TPD spectra (a) and AES spectra (b) of Ru(0001) (in black) and SiO_2/Ru(0001) (in red) surfaces after exposure to 10^{-5} mbar O_2 at 700 K for 45 min. The results for "as grown" SiO_2/Ru(0001) in green are shown for comparison.

Now we address the results of oxidation of silicate-covered Ru(0001). Note that below 1200 K, there wasn't any oxygen desorption for the "as grown" silicate film (Figure 5.1a, green curve). As silicate itself does not decompose or dewet at these temperatures as judged by IRAS [205], small desorption signal above ~1100 K could be assigned to the onset of oxygen desorption from the Ru(0001) surface underneath, which fully occurs only at temperatures as high as 1400 K [192].

Next, the same conditions as used above for the preparation of RuO_2(110) films (i.e. 10^{-5} mbar O_2 at 700 K for 45 min) were used for the silicate-covered Ru(0001). The corresponding TPD spectrum (Figure 5.1a, red curve) resulted in two desorption signals which resemble those observed upon oxidation of pure Ru(0001). In principle, this

finding suggests that the formation of a Ru-oxide film underneath the silicate is possible, although it is strongly suppressed, as the integral intensity of the high temperature peak associated with the decomposition of Ru-oxide is by factor of ~3 lower than that of observed on the Ru(0001) sample. In accordance with AES investigation (Figure 5.1b), only slight increase in the O(510 eV)/Ru(280 eV) signal ratio (0.25 vs 0.21 for the oxidized and the "as grown" silicate samples, respectively) has been observed, and this is much lower than 0.7 observed for pristine Ru(0001) under these conditions.

Considerable qualitative differences were also observed by further comparison of TPD spectra obtained for these two surfaces. Particularly, the high-temperature desorption peak on oxidized silicate/Ru is by about 40 K shifted towards higher temperatures. Based on our previous studies of CO and D_2 adsorption showing shifts [205], it seems like that oxygen molecules, produced upon decomposition of Ru-oxide, need some time to find the pores in silicate to escape. Therefore, the desorption is delayed as compared to uncovered Ru(0001), and as such appeared at higher temperatures in TPD spectra. Interestingly, such a delay observed here for O_2 (~40 K) is almost the same as previously observed for D_2, and both are considerably larger than obtained for CO (~25 K), most likely because of $O_2(D_2)$ desorption additionally includes O(D) recombination and hence time.

On the contrary, such a shift wasn't observed for the low-temperature desorption peak at ~400 K. Moreover, its intensity is by factor of ~25 lower, whereas a factor ~3 is obtained for the high temperature peak. Since the weakly bonded state is associated with the $RuO_2(110)$ surface, it is possible that other surface terminations were expected for the Ru-oxide formed underneath silicate. As no ordered structure was observed by LEED inspection, the resulted Ru-oxide film is amorphous in nature.

On the basis of these results, the following scenario can be speculated. Apparently, the "as grown" silicate films possess some amounts of "holes" or large pores (e.g. 10-membered rings). The Ru surface behind these pores behaves, in essence, like uncovered Ru(0001). Subsequent oxidation results in the transformation of these small areas into $RuO_2(110)$ which gives rise to the low temperature desorption peak almost at the same temperature as observed for extended $RuO_2(110)$/Ru(0001). Based on the signal intensity ratio in pure and silicate covered Ru samples, one can estimate such

domains to cover about 4% of the entire surface, whereas the majority of Ru-oxide, which is of about 2 ML in nominal thickness as estimated from the high signals ratio, is present in the amorphous state. However, it is still unclear that whether this oxide film uniformly covers the Ru support or is preferentially formed in the proximity to the silicate pores responsible for the oxygen permeation.

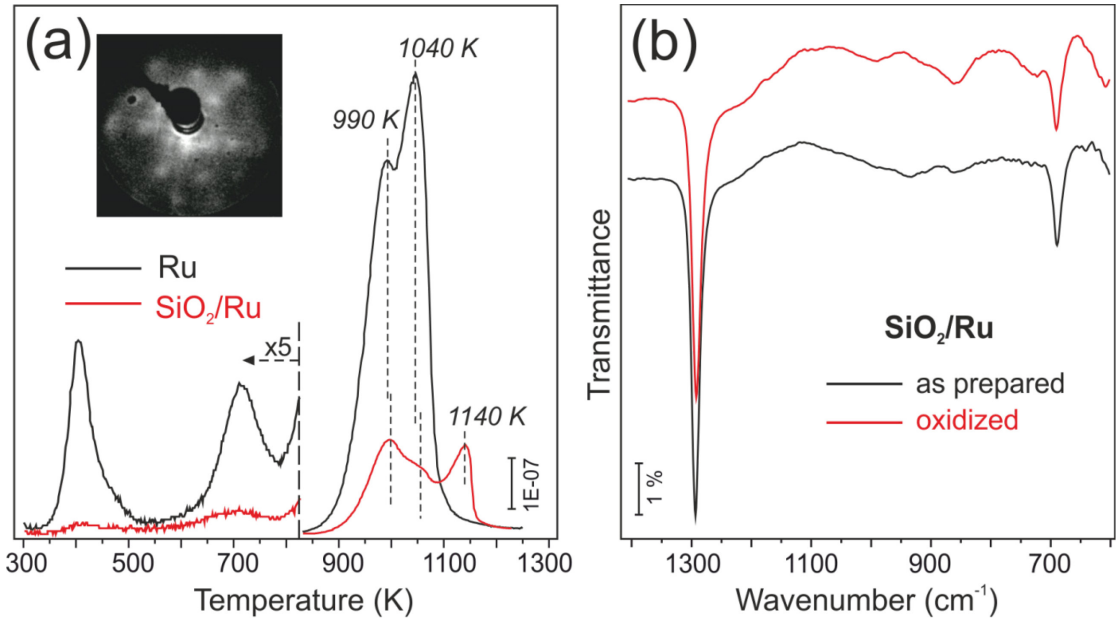

Figure 5.2: (a) O_2 (32 amu) signals in TPD spectra of Ru(0001) (in black) and SiO_2/Ru(0001) (in red) surfaces after exposure to 15 mbar O_2 at 700 K for 45 min. (b) IRA-spectra of the SiO_2/Ru(0001) film before (in black) and after (in red) oxygen exposure show that the structure of the silicate film is maintained.

In the next set of experiments, we studied oxidation at high oxygen pressures. Again, we first address the results for the clean Ru(0001) surface, which was exposed to 15 mbar O_2 at 700 K for 45 min and cooled down in oxygen to 300 K before oxygen was pumped out. Figure 5.2a shows O_2 desorption spectrum (in black) from the resulted surface. It can be seen that the total amount of O_2 molecules desorbing at high temperatures increased substantially (by factor of 4.5) as compared to that observed after oxidation in 10^{-5} mbar of O_2, therefore indicating continuous oxidation of deeper layers of Ru(0001) at elevated pressures. On the other hand, there is a decrement by factor of ~3.5 for the intensity of a weakly bonded state at ~400 K, which is characteristic for the RuO_2(110) terminated surface. Additionally, new desorption feature is seen at 710 K, and the most intense high temperature signal clearly shows two peaks at 990 and 1040 K, respectively.

To the best our knowledge, TPD spectra of Ru(0001) oxidation by near-atmospheric oxygen pressures have only been reported by Böttcher and co-workers [193]. As in our case, they observed two well-separated TPD features at about 1000 and 1050 K (O_β and O_α in their notation) upon exposure of Ru(0001) to 1 bar O_2 at 350-450 K, although the precise peaks position deviates depending on the O_2 dosage (in the range of 10^{11}-10^{14} L) and adsorption temperature. These features were assigned to deposition of substantial amount of oxygen (~3.5 ML) in the subsurface region, without creating the RuO_2 phase. Basically, this conclusion has been drawn on the basis of LEED patterns showing only Ru(0001)-(1x1) diffraction spots, and lack of desorption state at 400 K which they considered as a fingerprint for RuO_2. Upon exposure to 1 bar O_2 at higher temperatures 500 K, a new state (O_γ, in their notation) at 1120 K developed and it is shifted 30 K higher temperatures when the exposure is done at 525 K. This peak was assigned to initial formation of RuO_2 nuclei that progressively grew in size, and the eventually dominates the TPD spectra by covering the peaks α and β. Concomitantly, characteristic RuO_2(110) spots appeared in LEED patterns.

Unfortunately, they didn't provide O_2-TPD spectra below 800 K in order to compare with the signal that is observed at 710 K here (Figure 5.2a). Even so, on the basis of its low intensity, this feature seems to be associated with surface rather than bulk O species. To some extent, similar desorption feature has recently been reported by Over and co-workers [206] in the course of the initial oxidation of Ru(0001) at room temperature using atomic oxygen as oxidizing agent and assigned to Ru oxide clusters formed preferentially at step edges (Note that the sample temperature could not be accurately measured in this study, see ref.[207]). Certainly, such assignment can hardly be applied here for heavily oxidized Ru surface.

The origin of the oxygen desorption at ~400 K, which is a fingerprint exclusively for the RuO_2(110) surface, is important to mention here. Indeed, for the disordered RuO_2 films, grown on Pt(111) to the same film thickness (~6 ML) film thickness as on Ru(0001), such a signal was not observed (Figure 5.3).

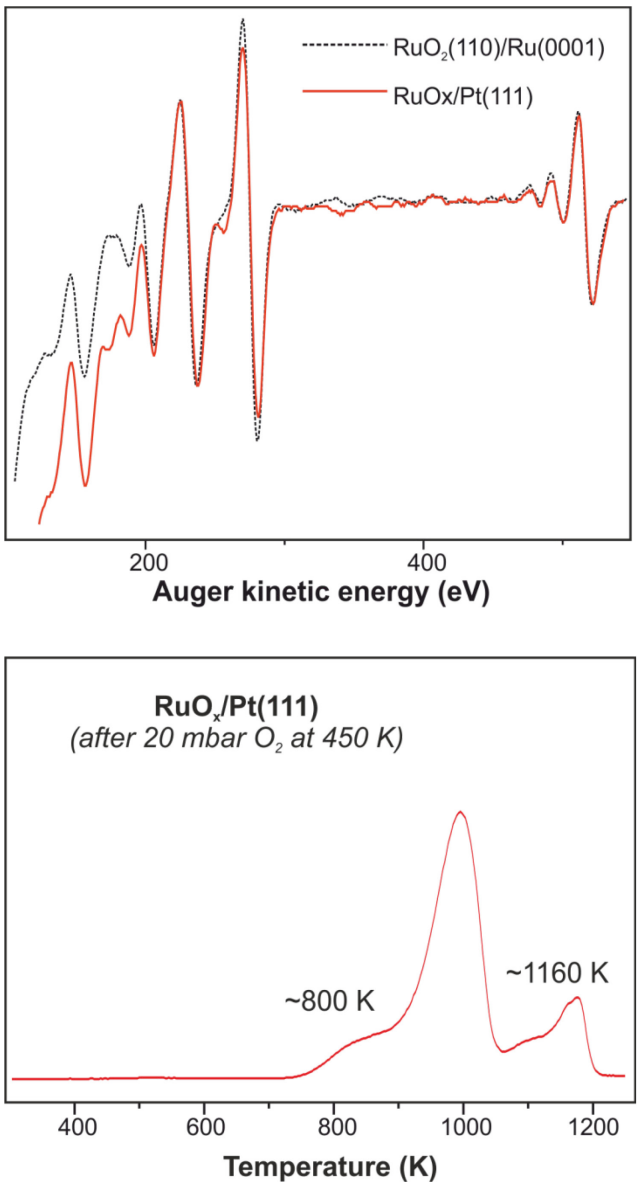

Figure 5.3: (top) Auger spectra of a crystalline $RuO_2(110)$ film formed on Ru(0001) (dashed line) and disordered RuO_x films grown on Pt(111) (red solid line), both prepared under the same conditions ($2x10^{-4}$ mbar; 700 K; 40 min). (Bottom) O_2 (32 amu) signal in TPD spectrum of the "as grown" RuO_x/Pt(111) film after exposure to 20 mbar of O_2 at 450 K for 10 min (Provided by Dr. Y. Martynova).

The films were prepared by Ru deposition in $5x10^{-7}$ mbar O_2 at 300 K and subsequent oxidation in $2x10^{-4}$ mbar at 700 K for 40 min, i.e. under conditions which normally resulted in $RuO_2(110)$ films on Ru(0001). However, weakly bonded O species at 400 K were not observed with these films prepared on Pt(111), even after exposure to 20 mbar O_2. Instead, additional TPD signals were observed at ~800 K and ~1160 K, which were missing on $RuO_2(110)$/Ru(0001) after the same treatment (Figure 5.3). Therefore, the lack of oxygen desorption at ~400 K does not mean the absence of Ru-oxide phase, but solely the absence of the $RuO_2(110)$ surface. Accordingly, a mixture of several Ru-oxide

phases can be formed, in which RuO_2(110) surface as well as other yet undefined surface possessing oxygen atoms which desorb at 710 K and 1140 K (Figure 5.2a) can be formed. Interestingly, for the RuO_2(110) films on Ru(0001) [203] and the RuO_x films on Pt(111) (Figure 5.3), all treated with 20 mbar O_2 at 450 K, the O_2 desorption at ~1000 K showed a single peak, whereas a double peak is observed here (Figure 5.2a) for oxidation at a higher temperature (700 K vs 450 K). It seems plausible, that all oxygen desorption features at T> 900 K are associated with decomposition of different Ru-oxide phases, which formation and/or phase separation depends on oxygen pressure and temperature.

Now we address the results of the high-pressure oxidation of silicate-covered Ru(0001). The same features in TPD were observed as in the case of pristine Ru(0001), although of much lower intensity (Figure 5.2a). Therefore, it can be suggested that silicate strongly passivates the Ru(0001) surface even at high oxygen pressures. Note, however, there is an additional feature that appears at 1140 K, which is missing on pure as well as silica-covered Ru(0001) at low pressures (Figure 5.1).

As it can be seen from the comparison of the IRA-spectra before and after oxidation, high-pressure treatment does not affect the bilayer structure of the silicate film. Apparently, the silicate film remains decoupled from the support which is oxidized, although to a much lower extent than bare Ru(0001). TPD features between 900 and 1100 K revealed again a small shift to higher temperatures for the oxidized sample as previously observed for oxidation at low pressure (Figure 5.1a). (This shift would, in fact, be larger if both spectra were measured at the same O content, as oxide sublimation commonly follows zero-order desorption kinetics, and hence the desorption maximum may shift to higher temperatures at increasing oxygen coverage.) Such a shift again can be explained by delaying of O_2 desorption by the time to find pores in the silicate.

It is significant to note that only upon oxidation at high pressures, and only on silicate-covered Ru(0001) is able to produce the desorption feature at 1140 K. To elaborate more on its origin, particularly to see whether this signal could be assigned to decomposition of adventitious silica nanoparticles and clusters, we prepared a sample possessing about 20% more Si than in the “perfect” silicate films. In addition, this film

was prepared using $^{18}O_2$ in order to differentiate O_2 related desorption features between silicate and Ru(0001) (Figure 5.4).

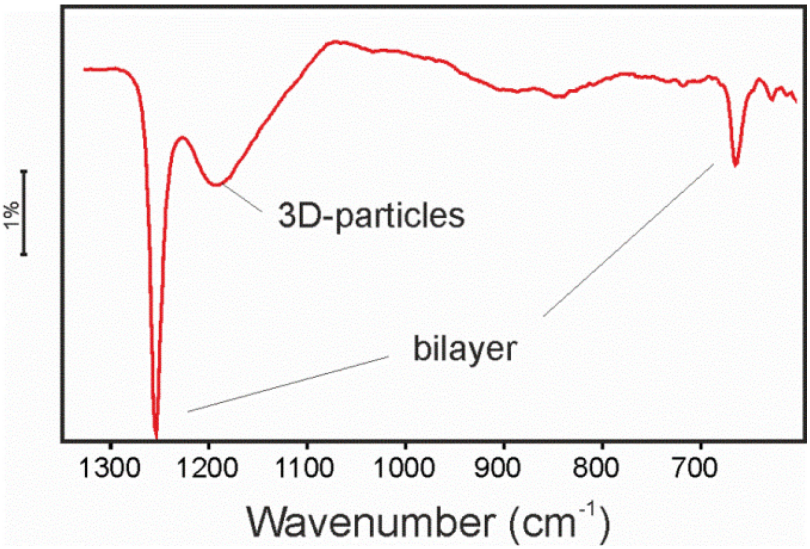

Figure 5.4: IRA-spectrum of the ^{18}O-labeled bilayer silicate film, which additionally exhibits a broad band at ~1190 cm^{-1} associated with silica nanoparticles.

As expected, a new broad band centered at 1190 cm^{-1} is observed in IRA-spectrum which is characteristic for three-dimensional, bulk-like (^{18}O-labeled) silica, suggesting that this sample contains also some silica nanoparticles. Then the sample was treated with normal $^{16}O_2$ and the TPD spectrum was recorded. The results (Figure 5.5) revealed desorption exclusively of $^{18}O_2$, thus providing the compelling evidence that oxygen in the silicate film does not scramble with ambient oxygen, and Ru oxide is formed by interaction with ambient oxygen molecules, in full agreement with IRAS results (Figure 5.2b) showing that the silicate film remains intact under these conditions.

Interestingly, we didn't observe the peak at 1140 K for this experiment. Since the similar desorption was found on disordered RuO_x films grown on Pt(111) (Figure 5.3), this feature was tentatively assigned to the desorption from poorly defined Ru-oxide phase(s), which are formed on Ru(0001) only when covered by a "perfect" silicate bilayer.

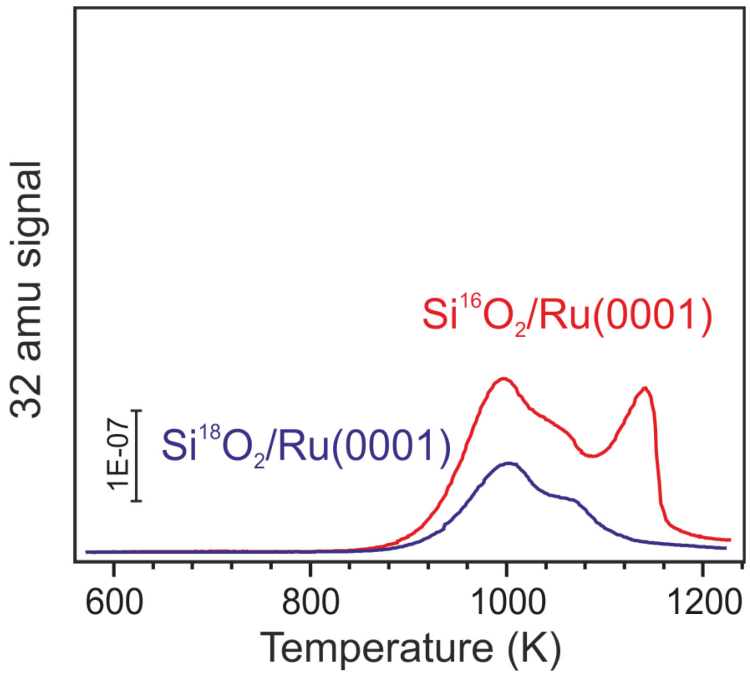

Figure 5.5: Oxygen (32 amu) signal in TPD spectra of SiO_2/Ru(0001) films prepared with ^{16}O and ^{18}O isotopes as indicated. Both films were then exposed to 15 mbar $^{16}O_2$ at 700 K for 45 min. Note that the ^{18}O-labeled film additionally contained silica nanoparticles (see Figure 5.4).

Finally, we investigated the oxidation of silicate-covered Ru(0001) using NO_2 as a stronger oxidizing agent [208]. Figure 5.6a shows series of IRA-spectra upon stepwise exposure to 3 mbar NO_2 at 700 K at the intervals as indicated. (The sample was always evacuated for the IRAS measurements). It is apparent that principal phonon bands at 1300 and 690 cm^{-1} gradually attenuated with increasing NO_2 exposure. 90 min exposure of NO_2 in total results in the development of a prominent shoulder as indicated by the arrow in Figure 5.6a, which is clear indication for the film dewetting and formation of three-dimensional silica nanoparticles. AES measurements of the resulted surface revealed O/Ru signal ratio of 0.5, which is remarkably higher than 0.25 observed for O_2-treated SiO_2/Ru sample, but still below than 0.7 observed for RuO_2(110)/Ru (see Figure 5.1b). TPD spectrum shown in Figure 5.6b also confirms deeper oxidation of the Ru support by NO_2 as compared to O_2.

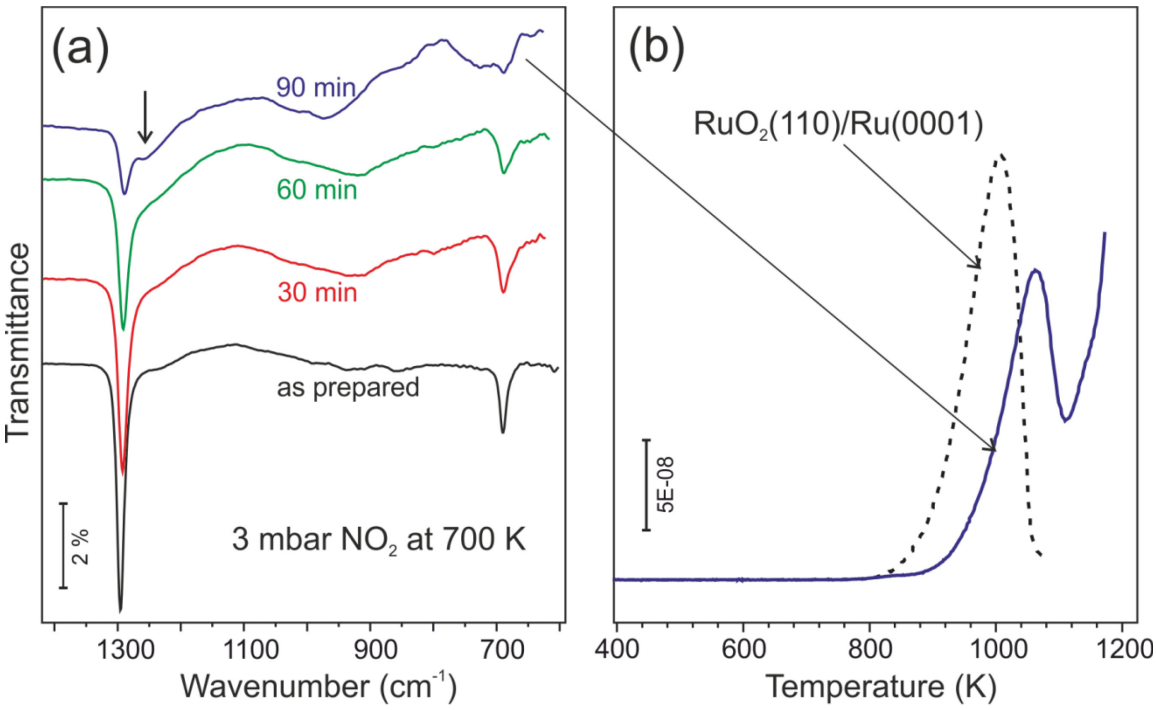

Figure 5.6: (a) IRA-spectra of SiO_2/Ru(0001) after stepwise exposure to 3 mbar NO_2 at 700 K for the total time as indicated. The arrow on panel (a) highlights the feature commonly assigned to three-dimensional silica particles caused by film dewetting. Oxygen TPD spectrum taken for the last sample is shown in (b). Spectrum for RuO_2(110)/Ru(0001) from Figure 5.1a is shown as dashed line, for comparison.

5.2 Case 2: Aluminosilicate Films

As a next step, the oxidation of aluminosilicate films grown on Ru(0001) was examined. The substitution of some Si ions with Al in the bilayer structure generate these films which may contain highly acidic, bridging hydroxyl species [153]. In order to make a comparison with pure silicate films, the $Al_{0.25}Si_{0.75}O_2$ aluminosilicate film was exposed to 15 mbar of O_2 at 700 K. The typical TPD spectrum is shown on Figure 5.7 in direct comparison with pure Ru and silicate/Ru samples. Apparently, TPD profile of aluminosilicate film resembles to the one for pure silicate. However, the oxidation of the Ru surface is suppressed by the aluminosilicate films in the larger extent.

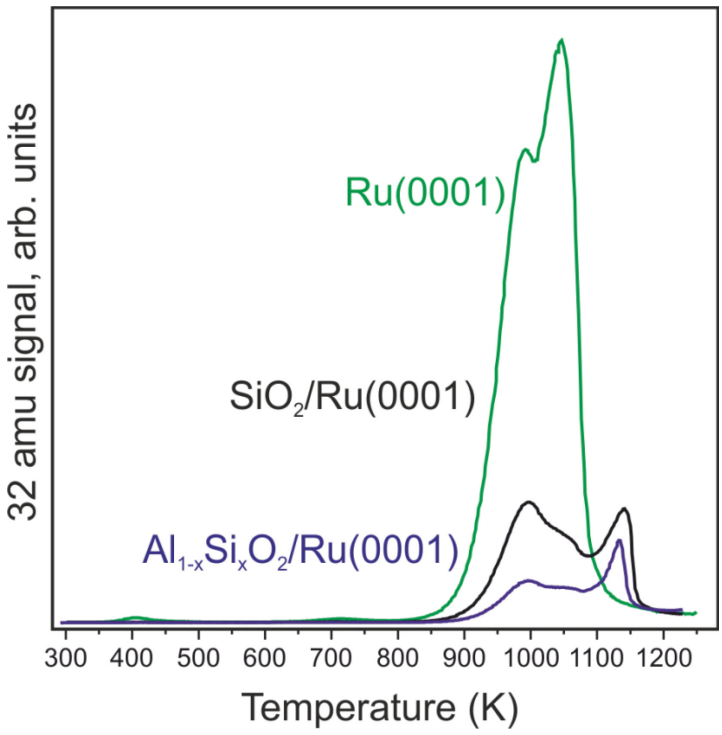

Figure 5.7: Comparative TPD spectra of O_2 (32 amu) from three different samples as indicated. All were exposed to 15 mbar of O_2 at 700 K for 40 min.

The passivation effects of aluminosilicate films were further corroborated by AP-XPS measurements by Dr. Anibal Boscoboinikat BNL. The experiments were performed as to directly compare interaction of oxygen with a bare Ru(0001) surface and with an aluminosilicate film of compositional stoichiometry $Al_{0.2}Si_{0.8}O_2$[153]. All the spectra were taken in ~10^{-4} mbar O_2 ambient at varying temperature, unless otherwise stated.

Bottom lines in Figure 5.8, shows Ru $3d_{5/2}$ and O 1s core level spectra for the clean Ru(0001) surface at 300 K. The Ru $3d_{5/2}$signal peaked at 280.1 eV contains a shoulder at lower binding energies (BE) (at 279.3 eV) which is attributed to the surface core level shift (SCLS). The adsorption of CO on the surface due to the UHV background results in a small signal at 531.8 eV in the O 1s region. As a result of O_2 exposure to 10^{-4} mbar at 300 K, ~529.8 eV signal appears that is assigned to chemisorbed O species. Subsequent heating to 623 K causes the signal gains intensity, due to increasing O coverage, ultimately forming an O-(1x1) overlayer [209]. Simultaneously, the SCLS shoulder attenuates and a new feature becomes visible on the higher BE side of the Ru $3d_{5/2}$ peak, which have been previously assigned to various Ru species in contact with O atoms, including surface and possibly subsurface oxygen [210]. Heating to 673 K didn't cause considerable changes in the spectra. However, the O 1s starts shifting to a lower

BE (ultimately, to 529.0 eV) and increasing in intensity on further heating to 723 K, thus indicating the oxidation of the deeper metal layers.

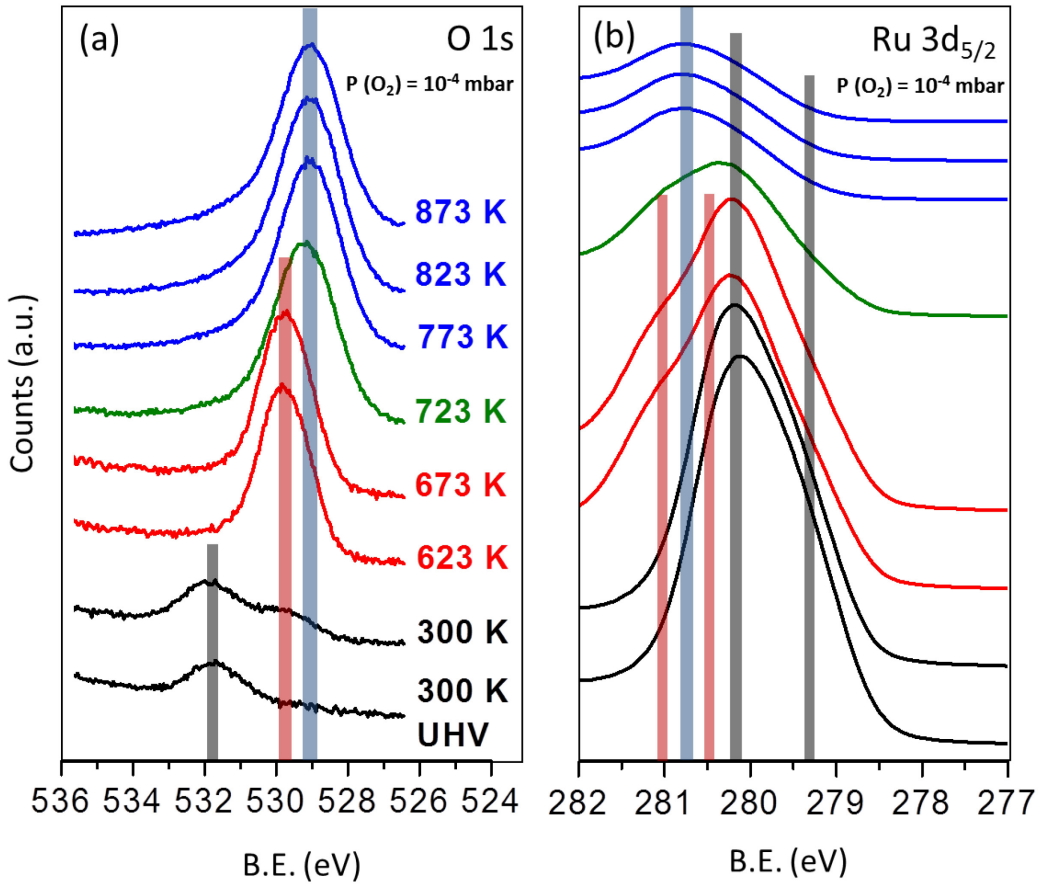

Figure 5.8: O 1s (a) and Ru $3d_{5/2}$ (b) regions in AP-XPS spectra taken in 10^{-4} mbar of O_2 at increasing temperatures as indicated. The lowermost spectra are obtained in UHV for the clean Ru(0001) surface prior to the oxygen exposure. The photon energy is 580 eV. The spectra are offset for clarity. (Provided by Dr. A. Boscoboinik)

No changes are observed at 873 K. Concomitantly, in the Ru $3d_{5/2}$ region, only the peak at 280.6 eV is seen, although its intensity gets decreased, in agreement with the formation of RuO_2 phase.

At least three different oxidation states were found to be coexisting by further deconvolution analysis of the Ru 3d signal measured at 873 K in 10^{-4} mbar O_2 (Figure 5.9).

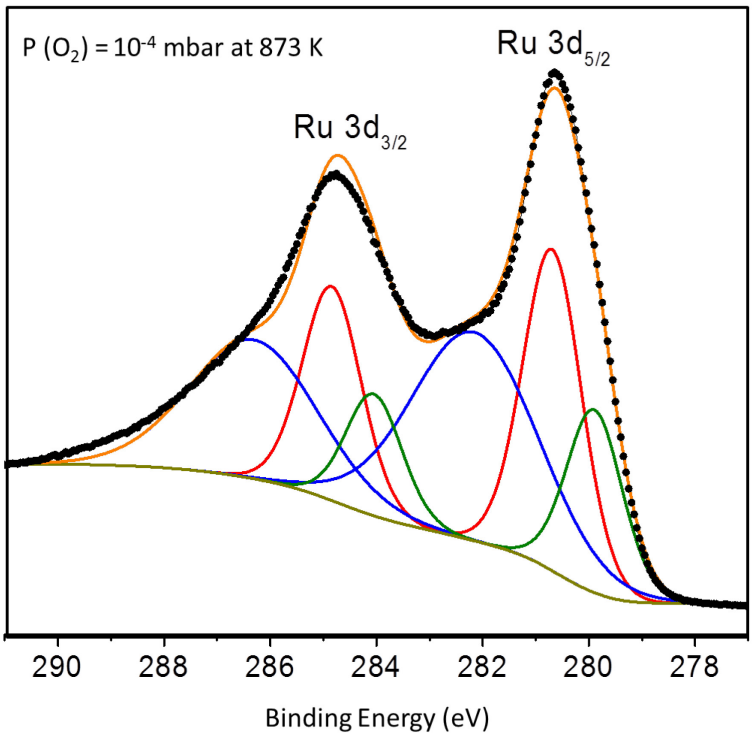

Figure 5.9: Deconvoluted Ru 3d spectrum taken on Ru(0001) in 1×10^{-4} mbar O_2 at 873 K. Different types of RuO_x are evident (red and blue lines), in addition to a small amount of metallic Ru (green line)(Provided by Dr. A. Boscoboinik).

This result agrees well with the presence of different Ru oxide phases deduced on the basis of TPD results shown in Figure 5.8 which also revealed the existence of at least three different oxide domains. Note that, 580 eV photon energy used here limit the probing depth to the first atomic layers with the inelastic mean free paths of photoelectrons ~6 Å and 5 Å for the Ru 3d and O 1s levels respectively [211].

Figure 5.10 compares the Ru 3d and O 1s spectra obtained for the bare and the aluminosilicate-covered Ru(0001) surfaces at 300 K and after heating in O_2 to elevated temperatures. It is apparent that an aluminosilicate covered Ru(0001) is more resistant towards oxidation. In principal, Ru only existed in metallic state, although with a slightly (by 0.2 eV) shifted BE. Upon heating in O_2 at 923 K, the intensity of the corresponding O 1s spectra increased ~30 %. This increment was assigned to the accumulation of the interfacial O atoms chemisorbed on Ru(0001) that exhibits BE of ~530 eV. Using the amounts of oxygen in the original aluminosilicate film as internal reference for calibration, the additional interfacial O, forced upon the high-pressure

O_2treatment was estimated to be 0.6 ML. (The signal can be further attenuated by atoms in the aluminosilicate, therefore this value must be taken as an upper limit.) Looking back to the aluminosilicate covered Ru 3d core level, the slight decrease in the peak area is related to the addition of the aforementioned chemisorbed oxygen on Ru(0001). This also explains the 0.2 eV shift by the attenuation of the SCLS. In addition to this, the Ru $3d_{3/2}$ peak has lost the intensity when compared to $3d_{5/2}$ peak, most likely due to burning adventitious carbon in oxygen ambient, as the Ru $3d_{3/2}$ partially overlaps with the C 1s level.

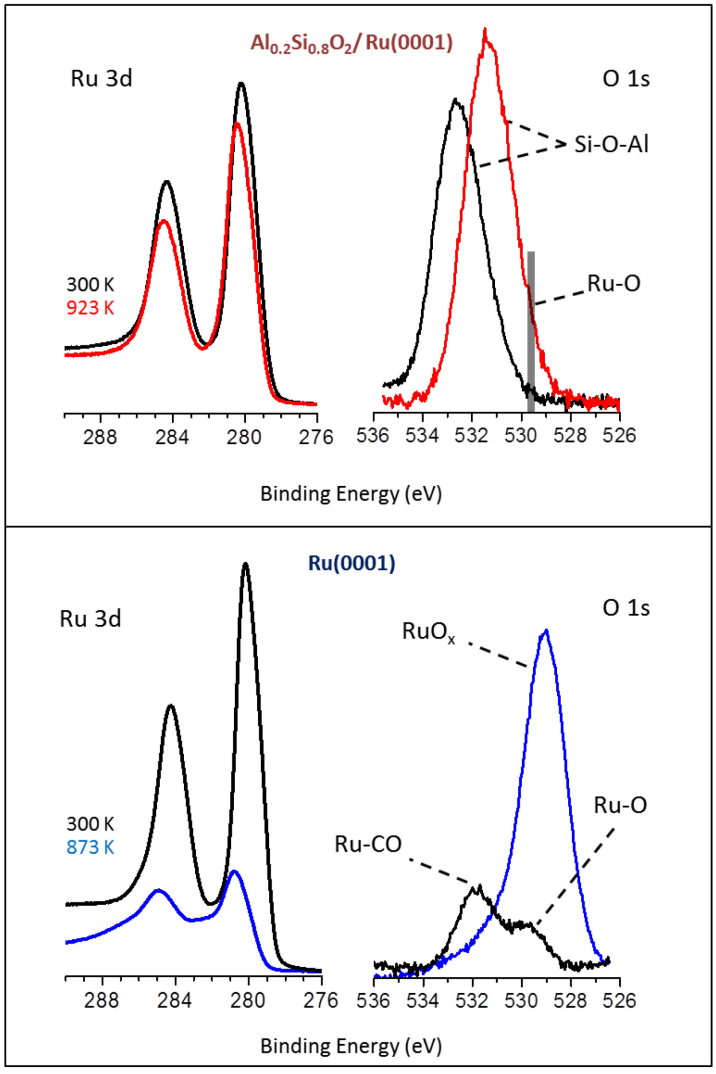

Figure 5.10: Ru 3d and O 1s regions in XP-spectra of the bare Ru(0001) surface and the aluminosilicate film measured at 300 K and after heating in 10^{-4} mbar O_2 to the indicated temperatures(Provided by Dr. A. Boscoboinik).

To sum up, the AP-XPS results indicated that the penetration of oxygen through the aluminosilicate film can take place and they dissociatively chemisorb on Ru(0001). However, the accumulation of more oxygen and subsequent oxidation to form Ru-oxide phases is completely inhibited in 10^{-4} mbar O_2 even at 923 K.

5.3 The Interaction of Methanol with Silicate Films

To shed more light on whether confinement effects may, indeed, affect surface chemistry, in the following, we show preliminary results for reactions with methanol. Ruthenium surfaces exhibit unique catalytic properties in direct methanol fuel cells [212]. The studies of methanol interactions with Ru surface is important for the determination of different reaction pathways and/or reaction intermediates in order to elucidate metal`s selectivity [213]. Methanol has wide range of industrial applications such as the catalytic conversion of methanol to hydrocarbons on solid acid catalysts like zeolites. In the following example, methanol interactions with three different surfaces namely, Ru(0001), silicate covered Ru(0001) and aluminosilicate covered Ru(0001) were investigated under the same conditions.

First, we expose clean Ru(0001) to 5 mbar of methanol at 400 K. Then, the sample was evacuated and infrared spectroscopy was performed in UHV. As it is mentioned previously, positive signal corresponds to the molecules leaving from surface as a result of annealing. The IRA spectra of methanol adsorbed on Ru(0001) at 400 K and subsequent annealing are shown in Figure 5.11a. Heating to 475 K and 575 K doesn't result in any desorption feature from the surface. However, annealing to 675 K exhibits three peaks located at 2220, 2195 and 2095 cm^{-1} which can be assigned the asymmetric and symmetric stretching modes of CD_3 groups respectively [214].Upon heating the surface to 1200 K, the CD species decompose, leaving carbon on the surface which then forms graphene as judged by LEED in Figure 5.11b.

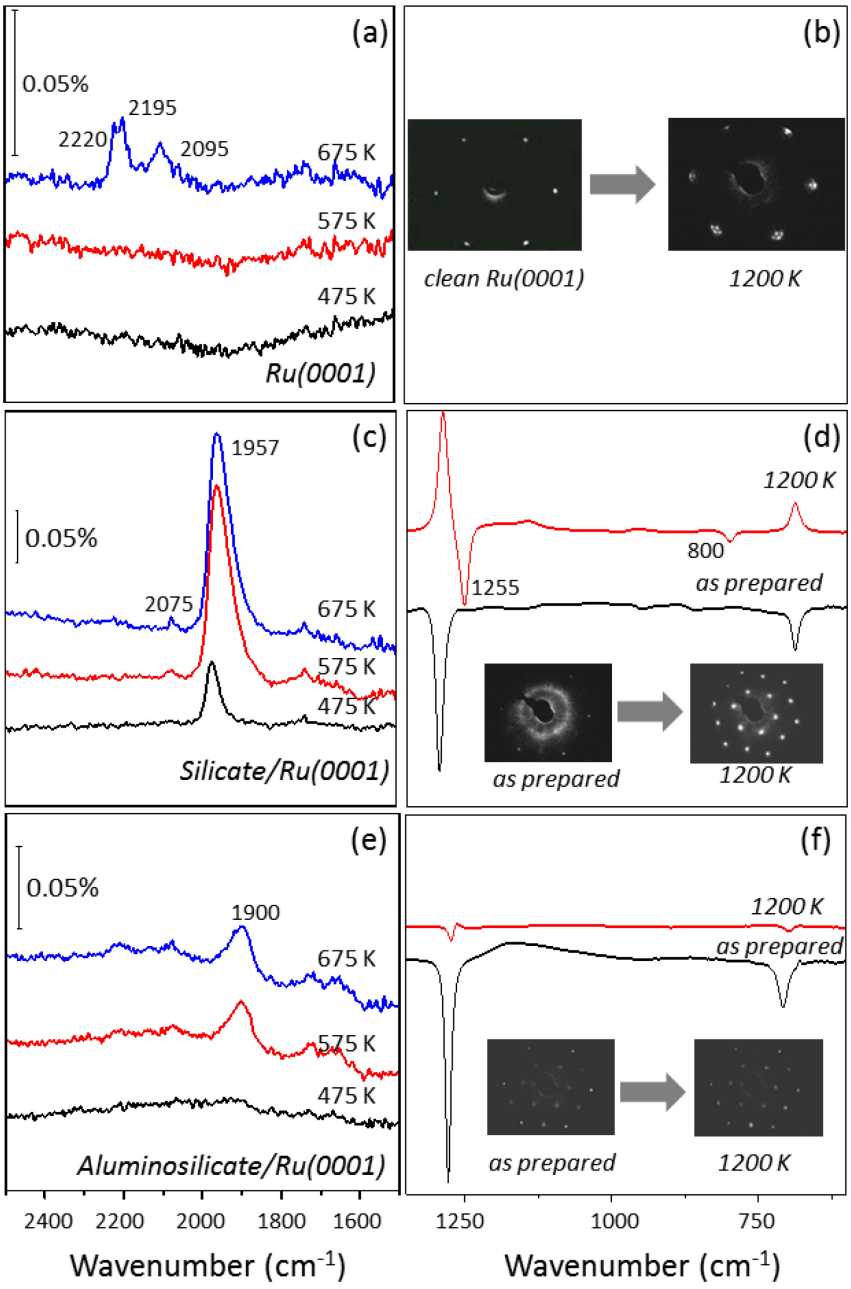

Figure 5.11: The adsorption of 5 mbar methanol (deuterated) at 400 K on (a,b) clean Ru(0001) (c, d) silicate covered Ru(0001) (e, f) aluminosilicate covered Ru(0001) (Each red spectrum in (b, d, f) is divided by the spectrum obtained as prepared film).

The IRAS result of methanol adsorption on silicate covered Ru(0001) is shown in Figure 5.11c. In this case, methanol decomposition follows a different pathway by leaving only CO species on the Ru(0001) surface showing 2075 and 1957 cm^{-1}bands.Apparently, no sign of C-D species was detected when the surface covered with silicate. The decomposition of methanol underneath silicate leaves graphitic carbon,

which can then react with silicate layer after annealing at 1200 K to form silicon carbide layer as evidenced by the transformation of principal silicate phonons to features 1255 and 800 cm^{-1} and corresponding LEED patternFigure 5.11d[215].

The exposure of methanol on aluminosilicate film revealed only a small amount of CO desorption from the surface (1900 cm^{-1}, Figure 5.11e). The main phonon features of aluminosilicate film didn't change and the crystallinity of the film was preserved after adsorption of methanol and annealing at 1200 K, implying that the film stays intact under these conditions (Figure 5.11f).

The decomposition of methanol on clean Ru(0001) surface have been investigated previously [213, 214, 216, 217]. It has been demonstrated that methanol can form methoxy species even at 80 K by breaking of O-H bond, and these methoxy species are dominant up to 220 K. They further decompose to carbon monoxide and hydrogen by annealing T>220 K and reaction is completed at 320 K. Partial dehydrogenation to formaldehyde rather than a complete fragmentation was also observed when the methanol was sequentially dosed. This different path was explained by the change in surface reactivity due to the poisoning effect caused by surface carbon (resulting from the first dose) which result in formaldehyde species stable up to 420 K. Interestingly, in our case, methanol decomposition at ambient conditions result in more stable C-D species (575-675 K) which can be explained by this effect of the accumulated carbon. Woodman et al. has studied methane interaction with Ru(0001) at high pressure (5 torr) with HREELS [218], and it has been found that methyldyne species (CH) are present on surface in a wide range of temperature (400-700 K). Therefore, highly stable C-D species that we observed in this study indicates that high pressure methanol adsorption changes the reactivity of Ru(0001) surface , and complete dehydrogenation doesn't take place under these conditions.

5.4 Conclusions

In this study, we investigated the interaction of oxygen with Ru(0001) supported ultrathin silicate and alminosilicate films at elevated O_2 pressures (10^{-4} mbar – 10 mbar) and temperatures (450 – 923 K). The results reveal that oxygen in the film does not scramble with oxygen in the ambient, therefore, the silicate film stay essentially intact

under these conditions. Although, molecular oxygen easily penetrates the film and dissociates on the Ru surface underneath, the formation of RuO_2(110) phase which readily takes place on bare Ru(0001) under the same conditions is strongly suppressed. These results indicate considerable spatial effects for oxidation reactions on metal surfaces in the confined space at the interface. Such phenomena have recently received much attention for the case of metal supported graphene and may potentially be interesting in the case of silicate as more robust materials under strongly oxidizing conditions.

Aluminosilicate covered Ru were found to be completely resistant towards the oxidation. With this respect, the observed passivation of the metal surface covered by the film could give some useful insights for using aluminosilicates in general, and zeolites in particular, as anti-corrosion coatings for various applications [219, 220].

The results of methanol interaction with silicate-covered Ru(0001) demonstrated that the reactivity of Ru(0001) surface has been modified due to the presence of weakly bound silicate layer and, the methanol decomposition pathway has been altered, resulting in only CO and no other sign of C-D species as in the case of clean Ru(0001). This means that reactivity of Ru(0001) towards methanol are strongly influenced in the 2D space underneath a silicate film, which caused considerable differences in terms of methanol decomposition when it is compared with clean Ru(0001) at the same conditions.

6. Summary and Outlook

The relationship between the atomic structure, composition and electronic properties of an oxide surface with its activity is a fundamental issue in catalytic studies. Surface science approach provides atomic scale information offabricatingmodel catalyst in a controlled way. The elucidation of silica surface sites available for diffusion and chemisorption of gas phase species is crucial to understand the role of silica in wide range of applications including material science, microelectronics and catalysis. In this regard, the discovery of well-defined bilayer silica films only weakly bonded to the metal support made the investigation of the physical and chemical properties of silicate materials possible at atomic scale. The aim of this thesis is to give an insight about adsorption, diffusion, reaction, and desorption mechanisms of several gas molecules on a well-ordered, ultrathin silicate film grown on Ru(0001) metal substrate.

Since the interaction of water with silica surfaces plays an important role in many fields including catalysis, the adsorption of water on silicate film was addressed first. It is found that hydroxylation occurs at defects most likely step edges at temperatures as low as ~180 K. Water dissociation seems to be more facile in the presence of several water molecules, since hydroxylation is observed only after water film formation at low temperatures and subsequent heating in order to desorb unreacted water molecules. Water dissociation yields surface Si-OH species and another hydrogen atom that produces the second OH including oxygen in silicate. This hydrogen may also leave the surface via desorption with water or reacts on Ru support. Recombinative desorption of OH through water appears to occur almost exclusively from the sites where dissociation first occurred.

The chemical properties of the silanols which were investigated by using CO, water, and NH_3 revealed no evidence for acidity of silanols, however, upon adsorption of NH_3, H-D exchange is observed, where OH species can be replaced by OD and vice versa. This finding strongly suggests that the reaction between hydroxyls and ammonia likely proceeds via the same mechanism as that between OD(OH) and $H_2O(D_2O)$. The adsorption of NH_3 on OD is stronger that with the regular silicate surface. Desorbing ammonia complexes after the interaction with hydroxyls were almost exclusively in the form of NDH_2, in which the ammonia desorption energy of ~37 kj/mol was calculated as an upper limit approximation of the H-D exchange activation barrier.

The interlayer space between the silicate sheet and the metal surface allows small molecules to diffuse and subsequent chemical reactions may occur on the metal surface. To investigate this, the permeation of CO, D_2 and O_2 molecules on a silicate film was studied. The results revealed that perfect crystalline silicate is hardly permeable for CO and D_2. The intercalation of gas molecules underneath silicate occurs through the defects (pores) associated with large rings, commonly present in amorphous silica. Although D_2showed Langmuir-type adsorption kinetics, CO adsorption at T>200 K exhibited an induction period followed by self-acceleration which could be as a result of an increase in the distance between silicate and the metal surface due to the CO-CO repulsive interaction accumulating at high coverages behind the pores.

In addition, we investigated the interaction of oxygen with silica and aluminosilicate supported on Ru(0001) at elevated O_2 pressures (10^{-5}-10 mbar) and temperatures (450-923 K). Silicate layer, which stays intact under these conditions, strongly passivates the RuO_2(110) formation, whereas, Ru oxidation is completely suppressed with ultrathin aluminosilicate films. This intercalation of dense oxygen adlayers indicate considerable nanoconfinement effects for oxidation reactions on metal surfaces occurring at nanosized space at the interface and therefore, may potentially be interesting by providing a confined environment for catalyst or corrosion passivation applications

Theabove-presented results showed that silicate films grown on metal substrates present a good model system for studying reactions on silica-based materials. The results revealed a complex behavior of metal supported silicate bilayer films upon ambient pressure gas exposures which involves gas transport through the pores and intercalation underneath silicate. Therefore, silicate sheet can be utilized as an attractive material like a hybrid molecular sieve for reactions that may otherwise occur unselectively on the supporting metal surface. Additionally, a confined space underneath a silicate film can generate new possibilities by upgrading the catalytic performance through controlled coating of a metal catalyst with weakly bounded silicates.

The fact that, the integrity of aluminosilicate film is preserved in all high-pressure gas adsorption conditions suggests thatthe aluminosilicate coatings have a good potential for the anti-corrosion applications.

On the other hand, the "results" also suggests that aluminosilicate film do not much suffer from "sub-surface chemistry". In principle, this allows one to look at surface chemistry of aluminosilicates as model for zeolites.Zeolites involve in many reactions like the catalytic cracking of crude oil, methanol to gasoline conversion, isomerization and oligomerization of alkenes and many others. The acidity of zeolites which are classified into Brønsted and Lewis acid sites are the origin of acid-catalyzed reactions. Brønsted acids sites exist as bridging OH groups between Al and Si atoms, and Lewis acids sites are generated by dehydration of bridging hydroxyls at higher temperatures. Recently, the preparation of an ultrathin aluminosilicate system which possess the highly acidic bridging hydroxyls, hence presenting the required features to model zeolites from a surface science approach was described in our group [153]. The presence of bridging hydroxyls was demonstrated by the adsorption of carbon monoxide as a probe molecules, which forms an adduct with the proton and induces a red shift of the O-H stretching vibration which is proportional to the acidity. Later, it was also demonstrated that a weak base like ethene also bind to these bridging hydroxyls coordinatively and therefore, can provide information about the precursor state for the ethene oligomerization reaction[221]. In principle, when olefins such as butene, are in contact with acid catalysts, they undergo isomerization reaction as well [222]. This reaction includes double-bond migration (such as 1-butene to 2-butene), polymerization and finally H/D exchange [223].

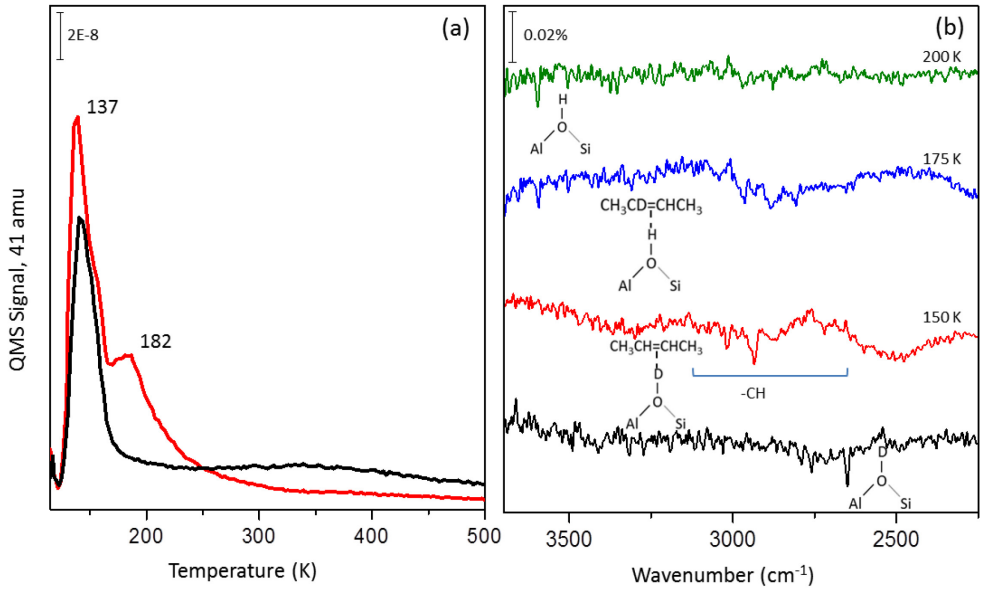

Figure 6.1: Spectra of cis-butene adsorbed on hydroxylated and non-hydroxylated aluminosilicate thin films.

Then, the H/D isotope exchange reaction of Brønsted acid sites with cis-butene was examined by using deuterated aluminosilicate thin film. The TPD spectra of cis-butene adsorption at 125 K on hydroxylated (red spectrum) and non-hydroxylated (black spectrum) aluminosilicate film are shown in Figure 6.1a. The measurements show evidence of a certain reaction between the cis-butene and bridging hydroxyls, which manifests itself as desorption feature at 182 K and is not observed for cis-butene TPD on non-hydroxylated surface. Instead, in the case of non-hydroxylated surface, a long desorption feature starting around 250 K was observed, and this can indicate that the film is also reactive due to the formation of Lewis acid sites after the removal of bridging hydroxyls. To have a better understanding about the surface chemistry, we have also carried out a complementary IRAS study. In this case, cis-butene was adsorbed at 150 K in order to prevent the condensation. Figure 6.1b shows a series of IRA-spectra after cis-butene adsorption at ~150 K on hydroxylated surface followed by heating to temperatures as indicated. The peak at 2650 cm^{-1} of the bridging OD group disappears upon adsorption of cis-butene at 150 K and butene molecules remain on the surface as judged by the IRAS bands at 3000-2800 cm^{-1}. Subsequent heating to 175 K decreases the intensity of CH stretching region and concomitantly, a peak appears at 3593 cm^{-1} corresponding to bridging OH group. Heating to 200 K removes the cis-butene from the surface and the intensity of OH bridging group is further increased. These results clearly indicate the interaction of cis-butene with bridging OD is accompanied by the H/D exchange reaction. Previously, the existence of isomerization from cis- to trans-butene during H/D isotope exchange reaction is distinguished by the C=C stretching bands at 1645 cm^{-1} and a deformation band at 1409 cm^{-1} [224]. Under the present experimental conditions, none of these bands could be detected with our system. This can be due to the metal selection rules, in which C=C bond is parallel to the surface and invisible in IRAS.

The results presented here indicate that the prepared model system has a good potential in order to study zeolite catalyzed reactions in a more controlled way on planar model system and therefore can provide some insights on structure-reactivity relationships which is hard to attain with conventional zeolites due to their highly complex constitution.

Symbols and Abbreviations

AES	Auger Electron Spectroscopy
DFT	Density Functional Theory
FID	Flame Ionization Detector
FT	Fourier Transform
GC	Gas Chromatography
HP	Cell High Pressure Cell
TEM	Transmission Electron Microscopy
IMFP	Inelastic Mean Free Path
IRAS	Infrared Reflection Absorption Spectroscopy
LEED	Low Energy Electron Diffraction
ML/MLE	Monolayer/ Monolayer Equivalent
PVD	Physical Vapor Deposition
SMSI	Strong Metal Support Interaction
STM	Scanning Tunneling Microscopy
TPD	Temperature Programmed Desorption
UHV	Ultra-High Vacuum
AP-XPS	Ambient Pressure X-Ray Photoemission Spectroscopy

Bibliography

[1] Liebau, F., *Structural Chemistry of Silicates*. 1st ed. (1985), Berlin Heidelberg: Springer-Verlag

[2] Online; accessed 04 March 2015; Available from: http://www.ks.uiuc.edu/Research/silica/

[3] Vogel, W., *Glass Chemistry*. 2nd ed. (1994), Berlin Heidelberg: Springer-Verlag

[4] Brill, R.; Grimm, H.; Hermann, C. and Peters, U., *Ann Phys* (1942). **41**: p. 233-244

[5] Pauling, L., *The Nature of the Chemical Bond*. (1945), Cornell Univ, New York: Cornell University Press, Ithaca

[6] Pantelides, S.T. and Harrison, W.A., *Physical Review B*, (1976). **13**: p. 2667-2691

[7] Balta, P. and Balta, E., *Introduction to the Physical Chemistry of the Vitreous State*. (1976), Bucharest Romania: Editura Academiei Romani/Abacus Press

[8] Nucho, R.N. and Mudhukar, A., *Physical Review B*, (1980). **21**: p. 1576-1588

[9] Shaikhutdinov, S. and Freund, H.-J., *Advanced Materials*, (2013). **25**: p. 49-67

[10] Jiang, Z.-H. and Zhang, Q.-Y., *Progres in Materials Science*, (2014). **61**: p. 144-215

[11] Greaves, G.N.; Fontaine, A.; Legarde, P.; Reoux, D. and Gurman, S.J., *Nature*, (1981). **293**: p. 611-616

[12] Zachariasen, W.H., *Journal of the American Chemical Society*, (1932). **54**: p. 3841-3851

[13] Warren, B.E., *Journal of the American Ceramic Society*, (1934). **17**: p. 249-254

[14] Ross, R.H.J., *Heterogeneous Catalysis: Fundamentals and Applications*. (2012), Amsterdam, Netherlands: Elsevier

[15] Zhuravlev, L.T., *Colloids and Surfaces A: Physicochemical and Engineering Aspects*, (2000). **173**: p. 1-38

[16] Potapov, V.V. and Zhuravlev, L.T., *Journal of Volcanology and Seismology*, (2007). **5**: p. 310-318

[17] Louie, D.K., *Handbook of sulphuric acid manufacturing*. 2nd ed. (2008): DKL Engineering

[18] Online; accessed 07 March 2015; Available from: https://catalysts.evonik.com/product/catalysts/en/catalyst-brands/pages/default.aspx

[19] Liu, Q.; Gath, K.K.; Bauer, J.C.; Schaak, R.E. and Lunsford, J.H., *Catalysis Letters*, (2009). **132**: p. 342-348

[20] Hogan, J.P. and Banks, R.L.; United States, *U. S. Patent* 2825721 (1958)

[21] Theopold, K.H., *Chemtech*, (1997). **27**: p. 26

[22] Weckhuysen, B.M. and Schoonheydt, R.A., *Catalysis Today*, (1999). **51**: p. 215

[23] Shell; United Kingdom, *British Patent* 1249079 (1971)

[24] Sheldon, R.A. and Van Bekkum, H., *Fine Chemicals through Heterogeneous Catalysis*. (2001), Weinheim, Germany: WILEY-VCH Verlag GmbH

[25] Lercher, J.A. and Jentys, A., *Handbook of Porous Solids*. Vol. 2. (2002), Weinheim: Wiley-VCH Verlag GmbH

[26] Gorte, R.J., *Handbook of Porous Solids*. Vol. 1. (2002), Weinheim: Wiley-VCH Verlag GmbH

[27] Elanany, M.; Koyama, M.; Kubo, M.; Broclawik, E. and Miyamoto, A., *Applied Surface Science*, (2005). **246**: p. 96-101

[28] Hunger, M., *Catalytically Active Sites: Generation and Characterization in Zeolites and Catalysis*. Vol. 2. (2010), Weinheim: Wiley-VCH Verlag GmbH

[29] Shigeishi, R.A.; Chiche, B.H. and Fajula, F., *Microporous and Mesoporous Materials*, (2001). **43**: p. 211-236

[30] Szostak, R., *Studies in Surface Science and Catalysis*, (1991). **58**: p. 153-200

[31] Weitkamp, J., *Solid State Ionics*, (2000). **131**: p. 175-188

[32] von Ballmoos, R.; Harris, D.H. and Magee, J.S., *Catalytic Cracking in Handbook of Heterogeneous Catalysis*. Vol. 4. (1997), Weinheim: Wiley-VCH Verlag GmbH

[33] Cheng, W.C.; Habib, E.T.J.; Rajagopalan, K.; Roberie, T.G.; Wormsbecher, R.F. and Ziebarth, M.S., *Fluid catalytic cracking in Handbook of Heterogeneous Catalysis*. Vol. 6. (2008), Weinheim: Wiley-VCH Verlag GmbH

[34] Sie, S.T., *Isomerization*, in *Handbook of Heterogeneous Catalysis*. 2008, Wiley-VCH Verlag GmbH: Weinheim.

[35] van Ween, J.A.R.; Minderhoud, J.K.; Huve, L.G. and Strok, W.H.J., *Hydro Cracking and Catalytic Dewaxing* in *Handbook of Heterogeneous Catalysis*. 2008, Wiley-VCH Verlag GmbH: Weinheim.

[36] Clark, M.C.; Smith, C.M.; Stern, D.L. and Beck, J.S., *Alkylation of Aromatics*, in *Handbook of Heterogeneous Catalysis*. 2008, Wiley-VCH Verlag GmbH: Weinheim.

[37] Stern, D.L.; Brown, S.H. and Beck, J.S., *Isomerization and Transalkylation of Aromatics*, in *Handbook of Heterogeneous Catalysis*. 2008, Wiley-VCH Verlag GmbH: Weinheim.

[38] Olsbye, U.; Svelle, S.; Bjorgen, M.; Beato, P.; Janssens, T.V.W.; Joensen, F.; Bordiga, S. and Lillerud, K.P., *Angewandte Chemie International Edition*, (2012). **51**: p. 5810-5831

[39] Patton, E.M.R.L. and Wilson, S.T., *Studies in Surface Science and Catalysis*, (1988). **37**: p. 13-20

[40] Chu, C.T.-W.; Kuehl, G.H.; Lago, R.M. and Chang, C.D., *Journal of Catalysis*, (1985). **93**: p. 451-458

[41] Szostak, R.; Nair, V. and Thomas, T.L., *Journal of the Chemical Society, Faraday Transactions 1*, (1987). **83**: p. 487-494

[42] Chu, C.T.-W. and Chang, C.D., *Journal of Physical Chemistry*, (1985). **89**: p. 1569-1571

[43] Gnep, N.S.; Doyemet, J.Y.; Seco, A.M. and Riberio, F.R., *Applied Catalysis*, (1988). **43**: p. 155-166

[44] Martens, J.A.; Sourverijns, W.; Van Rhijn, W. and Jacobs, P.A., *Handbook of Heterogeneous Catalysis*. Vol. 1. (1997), Weinheim: Wiley-VCH Verlag GmbH

[45] Olson, D.H. and Dempsey, E., *Journal of Catalysis*, (1969). **13**: p. 221-231

[46] Chao, K.-J.; Lin, J.-C.; Wang, Y. and Lee, G.H., *Zeolites*, (1986). **6**: p. 35-38

[47] Ertl, G.; Knözinger, H. and Weitkamp, J., *Environmental Catalysis*. (1999), Weinheim: Wiley-VCH

[48] Thomas, J.M. and Thomas, W.J., *Principle and Practice of Heterogeneous Catalysis*. (1997), Weinheim: VCH

[49] Langmuir, I., *Transactions of the Faraday Society*, (1922). **17**: p. 607-620

[50] Freund, H.-J.; Kuhlenbeck, H.; Libuda, J.; Rupprechter, G.; Baumer, M. and Hamann, J., *Topics in Catalysis*, (2000). **15**: p. 201-209

[51] Clair, T.P.S. and Goodman, D.W., *Topics in Catalysis*, (2000). **13**: p. 5-19

[52] Campbell, C.T., *Advances in Catalysis*, (1989). **36**: p. 1-54

[53] Nelson, A.E. and Schulz, K.H., *Review of Scientific Instruments*, (2000). **71**: p. 2471-2475

[54] Libuda, J.; Schauermann, S.; Laurin, M.; Schalow, T. and Freund, H.-J., *Monatshefte für Chemie*, (2005). **136**: p. 59-75

[55] Campbell, C.T., *Surface Science Reports*, (1997). **27**: p. 1-111

[56] Henry, C.R., *Surface Science Reports*, (1998). **31**: p. 231-325

[57] Dellwig, T.; Hartmann, J.; Libuda, J.; Meusel, I.; Rupprechter, G.; Unterhalt, H. and Freund, H.-J., *Journal of Molecular Catalysis A*, (2000). **162**: p. 51-66

[58] Gillet, E.; Channahone, S.; Matolin, V. and Gillet, M., *Surface Science*, (1985). **152/153**: p. 603-614

[59] Schauermann, S.; Johanek, V.; Laurin, M.; Libuda, J. and Freund, H.-J., *Chemical Physics Letters*, (2003). **381**: p. 298-305

[60] Conner, W.C.J. and Falconer, J.L., *Chemical Reviews*, (1995). **95**: p. 759-788

[61] Chen, H.-W. and White, J.M., *Journal of Molecular Catalysis*, (1986). **35**: p. 355-364

[62] Freund, H.-J.; Heyde, M.; Nilius, N.; Schauermann, S.; Shaikhutdinov, S. and Sterrer, M., *Journal of Catalysis*, (2013). **308**: p. 154-167

[63] Tauster, S.J.; Fung, S.C. and Garten, R.L., *Journal of the American Chemical Society*, (1978). **100**: p. 170-175

[64] Bowker, M.; Stone, P.; Morrall, P.; Smith, R.; Bennett, R.; Perkins, N.; Kvon, R.; Pang, C.; Fourre, E. and Hall, M., *Journal of Catalysis*, (2005). **234**: p. 172-181

[65] Libuda, J. and Freund, H.-J., *Surface Science Reports*, (2005). **57**: p. 157-298

[66] Haruta, M.; Tsubota, S.; Kobayashi, T.; Kageyama, H.; Genet, M.J. and Delmon, B., *Journal of Catalysis*, (1993). **144**: p. 175-192

[67] Chen, M. and Goodman, D.W., *Chemical Society Reviews*, (2008). **37**: p. 1860-1870

[68] Li, J.; Li, X.; Zhai, H.-J. and Wang, L.-S., *Science*, (2003). **299**: p. 864-867

[69] Sterrer, M.; Risse, T.; Heyde, M.; Rust, H.-P. and Freund, H.-J., *Physical Review Letters*, (2007). **98**: p. 206103-206106

[70] Shao, X.; Prada, S.; Giordano, L.; Pacchioni, G.; Nilius, N. and Freund, H.-J., *Angewandte Chemie International Edition*, (2011). **50**: p. 11525-11527

[71] Xu, X. and Goodman, D.W., *Applied Physics Letters*, (1992). **61**: p. 774-776

[72] He, J.W.; Xu, X.; Corneille, J.S. and Goodman, D.W., *Surface Science*, (1992). **279**: p. 119-126

[73] Schroeder, T.; Adelt, M.; Richter, B.; Naschitzki, M.; Baumer, M. and Freund, H.-J., *Surface Review and Letters*, (2000). **7**: p. 7-14

[74] Schroeder, T.; Hammoudeh, A.; Pykavy, M.; Magg, N.; Adelt, M.; Baumer, M. and Freund, H.-J., *Solid-State Electron*, (2001). **45**: p. 1471-1478

[75] Schroeder, T.; Giorgi, J.B.; Baumer, M. and Freund, H.-J., *Physical Review B*, (2002). **66**: p. 165422-165432

[76] Chen, M.S.; Santra, A.K. and Goodman, D.W., *Physical Review B*, (2004). **69**: p. 155404-155410

[77] Thiry, P.A.; Liehr, M.; Pireaux, J.J.; Sporken, R.; Caudano, R.; Vigneron, J.P. and Lucas, A.A., *Journal of Vacuum Science & Technology B*, (1985). **3**: p. 1118-1121

[78] Schaefer, J.A. and Göpel, W., *Surface Science*, (1985). **155**: p. 535-552

[79] Weissenrieder, J.; Kaya, S.; Lu, J.L.; Gao, H.J.; Shaikhutdinov, S.; Freund, H.-J.; Sierka, M.; Todorova, T.K. and Sauer, J., *Physical Review Letters*, (2005). **95**: p. 076103

[80] Giordano, L.; Ricci, D.; Pacchioni, G. and Ugliengo, P., *Surface Science*, (2005). **584**: p. 225-236

[81] Kaya, S.; Baron, M.; Stacchiola, D.; Weissenrieder, J.; Shaikhutdinov, S.; Todorova, T.K.; Sierka, M.; Sauer, J. and Freund, H.-J., *Surface Science*, (2007). **601**: p. 4849-4861

[82] Sierka, M.; Todorova, T.K.; Kaya, S.; Stacchiola, D.; Weissenrieder, J.; Lu, J.L.; Gao, H.J.; Shaikhutdinov, S. and Freund, H.-J., *Chemical Physics Letters*, (2006). **424**: p. 115-119

[83] Kundu, M. and Murata, Y., *Applied Physics Letters*, (2002). **80**: p. 1921-1923

[84] Zhang, Z.; Jiang, Z.; Yao, Y.; Tan, D.; Fu, Q. and Bao, X., *Thin Solid Films*, (2008). **516**: p. 3741-3746

[85] Kershner, D.C. and Medlin, J.W., *Surface Science*, (2008). **602**: p. 786-794

[86] Yu, X.; Yang, B.; Boscoboinik, J.A.; Shaikhutdinov, S. and Freund, H.-J., *Applied Physics Letters*, (2012). **100**: p. 151604-151608

[87] Loeffler, D.; Uhlrich, J.J.; Baron, M.; Yang, B.; Yu, X.; Lichtenstein, L.; Heinke, L.; Buechner, C.; Heyde, M.; Shaikhutdinov, S. and Freund, H.-J., *Physical Review Letters*, (2010). **105**: p. 146104

[88] Wlodarczyk, R.; Sierka, M.; Sauer, J.; Löffler, D.; Uhlrich, J.J.; Yu, X.; Yang, B.; Groot, I.M.N.; Shaikhutdinov, S. and Freund, H.-J., *Physical Review B*, (2012). **85**: p. 085403

[89] Lichtenstein, L.; Buechner, C.; Yang, B.; Shaikhutdinov, S.; Heyde, M.; Sierka, M.; Wlodarczyk, R.; Sauer, J. and Freund, H.-J., *Angewandte Chemie International Edition*, (2012). **51**: p. 404-407

[90] Lichtenstein, L.; Heyde, M. and Freund, H.-J., *Physical Review Letters*, (2012). **109**: p. 106101-106105

[91] Wovchko, E.A.; Camp, J.C.; Glass, J.A.J. and Yates, J.T.J., *Langmuir*, (1995). **11**: p. 2592-2599

[92] Hoffmann, F.M., *Surface Science Reports*, (1983). **3**: p. 107-192

[93] Schrader, B. (1995), Weinheim, Germany: VCH Verlagsgesellschaft mbH

[94] Meloan, C.E., *Elementary Infrared Spectrsocopy*. (1963), New York: The Macmillan Company

[95] Yates, J.T.J. and Madey, T.E., *Vibrational Spectrsocopy of Molecules on Surfaces*. (1987), New York: Plenum Press

[96] Woodruff, D.P. and Delchar, T.A., *Modern Techniques of Surface Science*. (1986), Cambridge: Cambridge University Press

[97] Francis, S.A. and Allison, A.H., *Journal of the Optical Society of America*, (1959). **49**: p. 131

[98] Pritchard, J., *Vibrations in Adsorbed Layers*. Conference Records Series of KFA. (1978), Julich: KFA

[99] Stuart, B., *Infrared Spectroscopy: Fundamentals and Applications*. (2004), West Sussex: John Wiley & Sons Ltd.

[100] Atkins, P. and De Paula, J., *Physical Chemistry*. 8 ed. (2006), Oxford, UK: Oxford University Press

[101] Niemantsverdriet, J.W., *Spectroscopy in Catalysis*. Vol. 3. (2007), Weinheim: Wiley-VCH Verlag GmbH

[102] Davis, M.E. and Davis, R.J., *Fundamentals of Chemical Reaction Engineering*. (2003), New York: McGraw-Hill

[103] Christmann, K., *Introduction to Surface Physical Chemistry*. (1991), Darmstadt: Springer-Verlag GmbH

[104] Cabrera, A.L., *The Journal of Chemical Physics*, (1990). **93**: p. 2854-2858

[105] Arrhenius, S.A., *Zeitschrift für Physikalische Chemie*, (1889). **4**: p. 96-116

[106] Kautto, E.; Kuhalainen, J. and Manninen, M., *Physica Scripta*, (1997). **55**: p. 628-633

[107] Redhead, P.A., *Vacuum*, (1962). **12**: p. 203-211

[108] Oura, K.; Lifshits, V.G.; Saranin, A.A.; Zotov, A.V. and Katayama, M., *Surface Science An Introduction*. (2003), Heidelberg: Springer-Verlag Berlin Heidelberg

[109] Seah, M.P. and Dench, W.A., *Surface and Interface Analysis*, (1979). **1**: p. 1-11

[110] Jona, F.; Strozier, J.A.J. and Yang, W.S., *Reports on Prgress in Physics*, (1982). **45**: p. 527-585

[111] Meitner, L., *Zeitschrift für Physik*, (1922). **9**: p. 131-144

[112] Auger, P., *C. R. A. S.*, (1923). **177**: p. 169-171

[113] Ong, J.L. and Lucas, L.C., *Biomaterials*, (1998). **19**: p. 455-464

[114] Harris, L.A., *Journal of Applied Physics*, (1968). **39**: p. 428-431

[115] Poole, C., *Gas Chromatography*. (2012), Oxford: Elsevier Inc.

[116] Grob, R.L. and Barry, E.F., *Modern Practice of Gas Chromatography*. (2004), New Jersey: John Wiley & Sons

[117] Lister, T., *Modern Chemical Techniques*. (1996), Great Britain: Royal Society of Chemistry

[118] Wilde, K.D. and Engewald, W., *Practical Gas Chromatography A Comprehensive Reference*. (2014), Heidelberg: Springer-Verlag Berlin Heidelberg

[119] Yang, B.; Kaden, W.E.; Yu, X.; Boscoboinik, J.A.; Martynova, Y.; Lichtenstein, L.; Heyde, M.; Sterrer, M.; Wlodarczyk, R.; Sierka, M.; Sauer, J.; Shaikhutdinov, S. and Freund, H.-J., *Physical Chemistry Chemical Physics*, (2012). **14**: p. 11344-11351

[120] Carriere, B. and Lang, B., *Surface Science*, (1977). **64**: p. 209-223

[121] Carriere, B. and Deville, J.P., *Surface Science*, (1979). **80**: p. 278-286

[122] Yang, J. and Wang, E.G., *Current Opinion in Solid State and Materials Science*, (2006). **10**: p. 33-39

[123] Morrow, B.A.; Cody, I.A. and Lee, S.M., *Journal of Physical Chemistry*, (1976). **80**: p. 2761-2767

[124] Rignanese, G.-M.; Charlier, J.-C. and Gonze, X., *Phys. Chem. Chem. Phys.*, (2004). **6**: p. 1920-1925

[125] Hofmann, U.; Endell, K. and Wilm, D., *Angewandte Chemie* (1934). **47**: p. 539

[126] Rideal, E.K., *Transactions of the Faraday Society*, (1936). **32**: p. 4

[127] Kiselev, A.V., *Kolloidn Zh.*, (1936). **2**: p. 17

[128] Yaroslavsky, N.G. and Terenin, A.N., *Dokl. Akad. Nauk SSSR*, (1949). **66**: p. 885

[129] Chuang, I.S. and Maciel, G.E., *Journal of Physical Chemistry B*, (1997). **101**: p. 3052-3064

[130] Bunker, B.C.; Haaland , D.M.; Michalske, T.A. and Smith, W.L., *Surface Science*, (1989). **222**: p. 95-118

[131] Morrow, B.A. and McFarlan, A.J., *Journal of Physical Chemistry*, (1992). **96**: p. 1395-1400

[132] Morrow, B.A. and McFarlan, A.J., *Langmuir*, (1991). **7**: p. 1695-1701

[133] Hoffmann, P. and Knozinger, E., *Surface Science*, (1987). **188**: p. 181-198

[134] Cypryk, M. and Apeloig, Y., *Organometallics*, (2002). **21**: p. 2165

[135] Goumans, T.P.M.; Wander, A.; Brown, W.A. and Catlow, C.R.A., *Phys. Chem. Chem. Phys.*, (2007). **9**: p. 2146-2152

[136] Zhu, T.; Li, J.; Lin, X. and Yip, S., *J. Mech. Phys. Solids*, (2005). **53**: p. 1597

[137] Iler, R.K., *The Chemistry of Silica*. (1979), New York: Wiley

[138] J., Y.G., *Journal of Colloid Science*, (1958). **13**: p. 67-85

[139] Young, G.J. and Bursh, T.P., *Journal of Colloid Science*, (1960). **15**: p. 361-369

[140] Iarlori, S.; Ceresoli, D.; Bernasconi, M.; Donadio, D. and Parrinello, M., *Journal of Physical Chemistry B*, (2000). **105**: p. 8007-8013

[141] Du, M.H.; Lolchin, A. and Cheng, H.-P., *Journal of Chemical Physics*, (2003). **119**: p. 6418

[142] Ma, Y.; Foster, A.S. and Nieminen, T., *Journal of Chemical Physics*, (2005). **122**: p. 144709

[143] Chuang, I.S.; Kinney, D.R. and Maciel, G.E., *Journal of American Chemical Society*, (1993). **115**: p. 8695-8705

[144] Borello, E.; A., Z. and Morterra, C., *Journal of Physical Chemistry*, (1967). **71**: p. 2938

[145] Sneh, O. and George, S.M., *Journal of Physical Chemistry*, (1995). **99**: p. 4639-4647

[146] Wendt, S.; Frerichs, M.; Wei, T.; Chen, M.S.; Kempter, V. and Goodman, D.W., *Surface Science*, (2004). **565**: p. 107-120

[147] Kaya, S.; Weissenrieder, J.; Stacchiola, D.; Shaikhutdinov, S. and Freund, H.-J., *Journal of Physical Chemistry C*, (2007). **111**: p. 759-764

[148] Morrow, B.A. and Cody, I.A., *Journal of Physical Chemistry*, (1976). **80**: p. 1995-1998

[149] Chiang, C.M.; Zegarski, B.R. and Dubois, L.H., *Journal of Physical Chemistry*, (1993). **97**: p. 6948-6950

[150] Persson, B.N. and Ryberg, R., *Physical Review B*, (1981). **24**: p. 6954-6970

[151] Heyde, M.; Shaikhutdinov, S. and Freund, H.-J., *Chemical Physics Letters*, (2012). **550**: p. 1-7

[152] Zecchina, A.; Lamberti, C. and Bordiga, S., *Catalysis Today*, (1998). **41**: p. 169-177

[153] Boscoboinik, J.A.; Yu, X.; Yang, B.; Fischer, F.D.; Wlodarczyk, R.; Sierka, M.; Shaikhutdinov, S.; Sauer, J. and Freund, H.-J., *Angewandte Chemie International Edition*, (2012). **51**: p. 6005-6008

[154] Morimoto, T.; Yanai, H. and Nagao, M., *Journal of Physical Chemistry*, (1976). **80**: p. 471-475

[155] Todorova, T.K.; Sierka, M.; Sauer, J.; Loeffler, D.; Uhlrich, J.J.; Yu, X.; Yang, B.; Groot, I.M.N.; Shaikhutdinov, S. and Freund, H.-J., *Physical Review B*, (2006). **73**: p. 165414

[156] Giordano, L.; Del Vitto, A. and Pacchioni, G., *Journal of Chemical Physics*, (2006). **124**: p. 034701-034707

[157] Baron, M.; Stacchiola, D.; Ulrich, S.; Nilius, N.; Shaikhutdinov, S.; Freund, H.-J.; Martinez, U.; Giordano, L. and Pacchioni, G., *Journal of Physical Chemistry C*, (2008). **112**: p. 3405-3409

[158] Kaden, W.E.; Buechner, C.; Lichtenstein, L.; Stuckenholz, S.; Ringleb, F.; Heyde, M.; Sterrer, M.; Freund, H.-J.; Giordano, L.; Pacchioni, G.; Nelin, C.J. and Bagus, P.S., *Physical Review B*, (2014). **89**: p. 115436

[159] Holt, J.K.; Park, H.G.; Wang, Y.; Stadermann, M.; Artyukhin, A.B.; Grigoropoulos, C.P.; Noy, A. and Bakajin, O., *Science*, (2006). **312**: p. 1034-1037

[160] Gruener, S. and Huber, P., *Physical Review Letters*, (2008). **100**: p. 064502

[161] Kavalenka, M.N.; Striemer, C.C.; Fang, D.Z.; Gaborski, T.R.; McGrath, J.L. and Fauchet, P.M., *Nanotechnology*, (2012). **23**: p. 145706

[162] Unnikrishnan, S.; Jansen, H.V.; Falke, F.H.; Tas, N.R.; Wolferen, H.A.G.M.V.; Boer, M.J.D.; Sanders, R.G.P. and Elwenspoek, M.C., *Nanotechnology*, (2009). **20**: p. 305304

[163] Savard, M.; Tremblay-Darveau, C. and Gervais, G., *Physical Review Letters*, (2009). **103**: p. 104502

[164] Bunch, J.S.; Verbridge, S.S.; Alden, J.S.; van der Zande, A.M.; Parpia, J.M.; Craighead, H.G. and McEuen, P.L., *Nano Letters*, (2008). **8**: p. 2458-2462

[165] Jiang, D.-e.; Cooper, V.R. and Dai, S., *Nano Letters*, (2009). **9**: p. 4019-4024

[166] Mu, R.; Fu, Q.; Jin, L.; Lyu, L.; Fang, G.; Tan, D. and Bao, X., *Angewandte Chemie International Edition*, (2012). **51**: p. 4856-4859

[167] Sutter, P.; Sadowski, J.T. and Sutter, E.A., *Journal of American Chemical Society*, (2010). **132**: p. 8175-8179

[168] Feng, X.; Maier, S. and Salmeron, M., *Journal of American Chemical Society*, (2012). **134**: p. 5662-5668

[169] Yao, Y.; Fu, Q.; Zhang, Y.Y.; Weng, X.; Li, H.; Chen, M.; Jin, L.; Dong, A.; Mu, R.; Jiang, P.; Liu, L.; Bluhm, H.; Liu, Z.; Zhang, S.B. and Bao, X., *PNAS*, (2014). **111**: p. 17023-17028

[170] Sutter, P.; Sadowski, J.T. and Sutter, E., *Physical Review B*, (2009). **80**: p. 245411

[171] Yang, B.; Boscoboinik, J.A.; Yu, X.; Shaikhutdinov, S. and Freund, H.-J., *Nano Letters*, (2013). **13**: p. 4422-4427

[172] Pfnur, H.; Feulner, P. and Menzel, D., *Journal of Chemical Physics*, (1983). **79**: p. 4613-4623

[173] Pfnur, H.; Menzel, D.; Hoffmann, F.M.; Ortega, A. and Bradshaw, A.M., *Surface Science*, (1980). **93**: p. 431-452

[174] Feulner, P. and Menzel, D., *Surface Science*, (1985). **154**: p. 465-488

[175] Kneitz, S.; Gemeinhardt, J. and Steinruck, H.P., *Surface Science*, (1999). **440**: p. 307-320

[176] Pfnur, H. and Menzel, D., *Journal of Chemical Physics*, (1983). **79**: p. 2400-2410

[177] Kostov, K.L.; Widdra, W. and Menzel, D., *Surface Science*, (2004). **560**: p. 130-144

[178] Lindroos, M.; Pfnur, H.; Feulner, P. and Menzel, D., *Surface Science*, (1987). **180**: p. 237-251

[179] Mak, C.H.; Brand, J.L.; Deckert, A.A. and George, S.M., *Journal of Chemical Physics*, (1986). **85**: p. 1676-1680

[180] Mak, C.H.; Brand, J.L.; Koehler, B.G. and George, S.M., *Surface Science*, (1987). **188**: p. 312-320

[181] McIntosh, E.M.; Wikfeldt, K.T.; Ellis, J.; Michaelides, A. and Allison, W., *Journal of Physical Chemistry Letters*, (2013). **4**: p. 1565-1569

[182] Peebles, D.E.; Schreifels, J.A. and White, J.M., *Surface Science*, (1982). **116**: p. 117-134

[183] Schiffer, A.; Jakob, P. and Menzel, D., *Surface Science*, (1997). **389**: p. 116-130

[184] Ueta, H.; Groot, I.M.N.; Gleeson, M.A.; Stolte, S.; Mcbane, G.C.; Juurlink, L.B.F. and Kleyn, A.W., *ChemPhysChem*, (2008). **9**: p. 2372-2378

[185] Kostov, K.L.; Rauscher, H. and Menzel, D., *Surface Science*, (1992). **278**: p. 62-86

[186] Shimizu, H.; Christmann, K. and Ertl, G., *Journal of Catalysis*, (1980). **61**: p. 412-429

[187] Puisto, M.; Nenonen, H.; Puisto, A. and Alatalo, M., *The European Physical Journal B*, (2013). **86**: p. 1-9

[188] Deckert, A.A.; Brand, J.L.; Arena, M.V. and George, S.M., *Surface Science*, (1989). **208**: p. 441-462

[189] Zhang, H.; Fu, Q.; Cui, Y.; Tan, D. and Bao, X., *Journal of Physical Chemistry C*, (2009). **113**: p. 8296-8301

[190] Over, H., *Chemical Reviews*, (2012). **112**: p. 3356−3426

[191] Böttcher, A.; Niehus, H.; Schwegmann, S.; Over, H. and Ertl, G., *Journal of Physical Chemistry B*, (1997). **101**: p. 11185-11191

[192] Böttcher, A. and Niehus, H., *Journal of Physical Chemistry B*, (1999). **110**: p. 3186-3195

[193] Blume, R.; Niehus, H.; Conrad, H. and Böttcher, A., *The Journal of Chemical Physics*, (2004). **120**: p. 3871-3879

[194] Kim, Y.D.; Over, H.; Krabbes, G. and Ertl, G., *Topics in Catalysis*, (2001). **14**: p. 95-100

[195] Kim, Y.D.; Seitsonen, A.P. and Over, H., *Surface Science*, (2000). **465**: p. 1-8

[196] Over, H. and Muhler, M., *Progress in Surface Science*, (2003). **72**: p. 3-17

[197] Kim, Y.D.; Seitsonen, A.P.; Wendt, S.; Wang, J.; Fan, C.; Jacobi, K.; Over, H. and Ertl, G., *The Journal of Physical Chemistry B*, (2001). **105**: p. 3752-3758

[198] Wendt, S.; Knapp, M. and Over, H., *Journal of American Chemical Society*, (2004). **126**: p. 1537-1541

[199] Reuter, K. and Scheffler, M., *Physical Review B*, (2003). **68**: p. 045407

[200] Wang, J.; Fan, C.Y.; Jacobi, K. and Ertl, G., *The Journal of Physical Chemistry B*, (2002). **106**: p. 3422-3427

[201] Böttcher, A.; Starke, U.; Conrad, H.; Blume, R.; Niehus, H.; Gregoratti, L.; Kaulich, B.; Barinov, A. and Kiskinova, M., *The Journal of Chemical Physics*, (2002). **117**: p. 8104-8109

[202] Flege, J.I.; Hrbek, J. and Sutter, P., *Physical Review B*, (2008). **78**: p. 165407

[203] Martynova, Y.; Yang, B.; Yu, X.; Boscoboinik, J.A.; Shaikhutdinov, S. and Freund, H.-J., *Catalysis Letters*, (2012). **142**: p. 657-663

[204] Rössler, M.; Günther, S. and Wintterlin, J., *The Journal of Physical Chemistry C*, (2007). **111**: p. 2242-2250

[205] Emmez, E.; Yang, B.; Shaikhutdinov, S. and Freund, H.-J., *The Journal of Physical Chemistry C*, (2014). **118**: p. 29034-29042

[206] Herd, B.; Goritzka, J.C. and Over, H., *The Journal of Physical Chemistry C*, (2013). **117**: p. 15148-15154

[207] Herd, B.; Knapp, M. and Over, H., *The Journal of Physical Chemistry C*, (2012). **116**: p. 24649-24660

[208] Mitchell, W.J. and Weinberg, W.H., *The Journal of Chemical Physics*, (1996). **104**: p. 9127-9136

[209] Over, H.; Seitsonen, A.P.; Lundgren, E.; Wiklund, M. and Andersen, J.N., *Chemical Physics Letters*, (2001). **342**: p. 467-472

[210] Blume, R.; Hävecker, M.; Zafeiratos, S.; Teschner, D.; Kleimenov, E.; Knop-Gericke, A.; Schlögl, R.; Barinov, A.; Dudin, P. and Kiskinova, M., *Journal of Catalysis*, (2006). **239**: p. 354-361

[211] Powell, C.J.J., *NIST Electron Inelastic-Mean-Free-Path database*. 2010, National Institute of Standards and Technology: Gaithersburg, MD.

[212] Milone, C.; Neri, G.; Donato, A.; Mussolino, M.G. and Mercadante, L., *Journal of Catalysis*, (1996). **159**: p. 253-258

[213] Hrbek, J.; DePaola, R.A. and Hoffmann, M., *Journal of Chemical Physics*, (1984). **81**: p. 2818-2827

[214] Barros, R.B.; Garcia, A.R. and Ilharco, L.M., *Journal of Physical Chemistry B*, (2001). **105**: p. 11186-11193

[215] Yang, B.; Shaikhutdinov, S. and Freund, H.-J., *Surface Science*, (2015). **632**: p. 9-13

[216] Gazdzicki, P. and Jakob, P., *Journal of Physical Chemistry C*, (2010). **114**: p. 2655-2663

[217] Barros, R.B.; Garcia, A.R. and Ilharco, L.M., *Journal of Physical Chemistry B*, (2004). **108**: p. 4831-4839

[218] Wu, M.-C. and Goodman, W., *Journal of American Chemical Society*, (1994). **116**: p. 1364-1371

[219] Banerjee, P.; Woo, R.; Grayson, S.; Majumder, A. and Raman, R., *Materials*, (2014). **7**: p. 6092-6104

[220] Krivenko, P.V. and Guziy, S.G., *Applied Clay Science*, (2013). **73**: p. 65-70

[221] Boscoboinik, J.A.; Yu, X.; Emmez, E.; Yang, B.; Shaikhutdinov, S.; Fischer, F.D.; Sauer, J. and Freund, H.-J., *The Journal of Physical Chemistry C*, (2013). **117**: p. 13547-13556

[222] Corma, A., *Chemical Reviews*, (1995). **95**: p. 559-614

[223] Kondo, J.N.; Liqun, S.; Wakabayashi, F. and Domen, K., *Catalysis Letters*, (1997). **47**: p. 129-133

[224] Kondo, J.N.; Wakabayashi, F. and Domen, K., *Catalysis Letters*, (1998). **53**: p. 215-220

List of Figures

List of Tables

List of Publications

1. "Oxidation of The Ru(0001) Surface Covered by Weakly Bound, Ultrathin Silicate Films"
   Emmez, E.; Boscoboinik, J. A.; Tenney, S.; Sutter, P.; Shaikhutdinov, S.; Freund, H.-J.
   Surface Science, *in press*

2. "Permeation of A Single-Layer SiO_2 Membrane and Chemistry in Confined Space"
   Emmez, E.; Yang, B.; Shaikhutdinov, S.; Freund, H.-J.
   J. Phys. Chem C, 2014, (118) 29034

3. "Interaction of Probe Molecules with Bridging Hydroxyls of Two-Dimensional Zeolites: A Surface Science Approach"
   Boscoboinik, A.J.; Yu, X.; **Emmez, E.**; Yang, B.;Shaikhutdinov, S.; Fischer, F. D.; Sauer, J.; Freund, H.-J.
   J. Phys. Chem. C, 2013, (117) 13547

4. "Hydroxylation of Metal Supported Sheet-like Silica Films"
   Yang, B.; **Emmez, E.**; Kaden, W.E.; Yu, X.; Boscoboinik, A.J.; Sterrer, M.; Shaikhutdinov, S.; Freund, H.-J.
   J. Phys. Chem. C, 2013, (117) 8336

5. "Role of the Exposed Pt Active Sites and BaO_2 formation in NO_x Storage Reduction Systems: A Model Catalyst Study on BaO_x/Pt(111)"
   Vovk, E.; **Emmez, E.**; Erbudak, M.; Bukhtiyarov, V.; Ozensoy, E.
   J. Phys. Chem. C, 2011, (115) 24256

6. "A Direct Evidence for the Instability and Deactivation of Mixed-Oxide Systems: Influence of Surface Segregation and Sub-surface Diffusion"
   Emmez, E.; Vovk, E.; Bukhtiyarov, V.; Ozensoy, E.
   J. Phys. Chem. C, 2011, (115) 22438

Selbständigkeitserklärung

Ich erkläre, dass ich die vorliegende Arbeit selbständig und nur unter Verwendung der angegebenen Literatur und Hilfsmittel angefertigt habe.

Berlin, den 09.07.2015 Emre Emmez